



SAPIENZA
UNIVERSITÀ DI ROMA

**Università degli Studi di Roma “Sapienza”
Facoltà di Scienze Matematiche, Fisiche e Naturali**

DIPARTIMENTO DI FISICA
Corso di Laurea Magistrale in Fisica

**NEUTRINO BEAM SIMULATIONS
AND DATA CHECKS
FOR THE NO ν A EXPERIMENT**

Candidate:
Marco Del Tutto
Matricola 1392341

Thesis Advisor:
Prof. Giovanni Rosa

External Advisors:
Prof. John W Cooper
Dr. Giulia Brunetti

Academic Year 2014–2015

COLOPHON

This thesis has been typeset by L^AT_EX and the `classicthesis` class.

CONTACTS: marco.deltutto@gmail.com, mdeltutt@fnal.gov.

NOTE: This thesis has been possible thanks to the Laurea Magistrale program for Italian students and the Fermilab Neutrino Division. The research work was performed at the Fermi National Accelerator Laboratory for a period of six months, from March to September 2015, working in the NO ν A Experiment.



Ai miei genitori,
perché senza di loro
niente di tutto questo sarebbe
mai stato possibile.

ACKNOWLEDGMENTS

Firstly, I would like to express my gratitude to my advisor, Prof. Giovanni Rosa, for supporting me in my studies. I would like to thank my advisors here at Fermilab, Prof. John W Cooper and Dr. Giulia Brunetti, because their guidance, support and advices helped me in all the time of this thesis. It was a real pleasure to work with you.

Besides my advisors, I would like to thank Dr. Emanuela Barzi and Prof. Giorgio Bellettini for having supported me to pursue my studies at Fermilab. The Laurea Magistrale program at Fermilab opened to me new possibilities that would have never been possible otherwise. Moreover, I would like to thank Dr. Simone Donati that allowed me to take part to the Summer Student at Fermilab program last year. This program marked the beginning of my thesis.

I would like to thank the Fermilab Neutrino Division for the support given to the Laurea Magistrale program. Thank you to Dr. Regina Rameika and Prof. Steve Brice.

A very special thanks goes out to the NO ν A Beam Group and especially to Dr. Alexander Radovic, Dr. Raphael Scroeter, Dr. Robert Hatcher, Gareth Kafka and Kuldeep Kaur Maan. You were always available to answer my questions and to help me every time I needed. Thank you. I also would like to thank all the NO ν A people I had the pleasure to talk with, you made my time here an amazing one.

Thanks to Dr. Alberto Marchionni that helped me to start my thesis, and to Dr. Jim Hylan that helped me during the Special Runs.

A very special thanks goes to the Neutrino Division and NO ν A administrative support, Etta Jonson and Stephanie Schuler. They really made my life easier. But also to the Fermilab Visa Office, especially to Kappatolia Sherman, who allowed me to start my thesis on time.

Thank you to my parents, who this thesis is dedicated. They allowed me to become the man that I am now; I owe everything to them. And thanks to all my family, especially my grandfather, Franco, who sadly passed away last year.

Last but not least, I would like to thank the person who has stood by my side through this thesis and I hope she will for all the next adventures. Thank you Cecilia for being part of my journey.

CONTENTS

Acknowledgments	4
Introduction	7
1 NEUTRINO PHYSICS	9
1.1 A brief history about neutrinos	9
1.2 Neutrino Oscillations	12
1.3 Neutrino oscillations in vacuum	13
1.3.1 General remarks	16
1.3.2 PMNS matrix	16
1.4 Oscillation Probability In Matter	17
1.5 Neutrino Mass Hierarchy	21
1.5.1 Motivation for Determining the Neutrino Mass Hierarchy	22
1.6 Overview of Neutrino Oscillation Experiments	23
2 THE NUMI BEAM LINE	26
2.1 The Target	27
2.2 Focusing System	29
2.2.1 Multi-Horn System	31
2.2.2 NuMI Horns	32
2.3 Decay Pipe, Hadron Absorber and Muon Shield	36
3 THE NOVA EXPERIMENT	37
3.1 A long-baseline experiment	38
3.2 NO ν A capabilities	39
3.2.1 $\nu_e / \bar{\nu}_e$ Appearance	39
3.2.2 $\nu_\mu / \bar{\nu}_\mu$ Disappearance	41
3.3 An off-axis experiment	42
3.4 The Detectors	44
4 PREDICTION OF THE NEUTRINO FLUX	48
4.1 Software Framework	48
4.2 Weighted Monte Carlo	49

4.2.1	The Lorentz Transformation	50
4.2.2	Importance weight	51
4.2.3	Implementation	52
4.3	FluxReader	53
4.3.1	The off-axis angle	54
4.4	The Ancestor List	56
4.4.1	Implementation	57
4.5	Number of interactions of the neutrino ancestors	58
4.6	Particle tracking using the Ancestor List	62
4.6.1	Tagging of particles going through the Horn neck	66
4.6.2	Tagging of under/over focused pions	67
4.6.3	Decomposition of the neutrino spectrum	68
4.7	Crossing point along the beam line for over-focused pions	72
4.8	Pion angle w.r.t. the beam line after the focusing	74
5	HORN CURRENT STUDIES	77
5.1	Motivations	77
5.2	Data Taking	81
5.3	Event Reconstruction	82
5.3.1	Energy Estimation	84
5.4	Event Selection	86
5.4.1	Near Detector pre-selection	87
5.4.2	Near Detector Selection	88
5.5	Data Quality	89
5.6	Data Analysis	93
5.6.1	Peak Position	93
5.7	Data Fits	99
5.8	The NO ν A Simulation Chain	99
5.9	Systematics	100
5.9.1	NuMI Flux Uncertainties	100
5.9.2	Detector related Uncertainties	101
5.10	Data - Monte Carlo Comparison	103
5.11	Data - MC Fits	110
	Conclusions	112
	Bibliography	114

INTRODUCTION

The Standard Model of particle physics (SM) successfully explains a wide variety of experimental results in terms of three generations of constituent quarks and leptons and their electroweak and strong interactions. In this frame, neutrinos remain the most enigmatic of the fundamental fermions as we still don't know the answers to several basic questions: what is their absolute mass scale? Do neutrinos violate the CP symmetry, and if yes to what extent? Are neutrinos and anti-neutrinos distinct particles (Dirac-type) or identical particles (Majorana-type)? Knowledge of the neutrino mass hierarchy, another missing tile of the overall picture, can help to tackle each of these questions. Moreover, it may lead to hints of physics beyond the SM, since neutrinos may obtain their mass in a different way than other fundamental fermions. The neutrino mass hierarchy has implications, as well, for cosmology and to understand the asymmetry between matter and anti-matter in the universe.

It is possible to address experimentally these questions looking at the phenomenon of neutrino oscillations, a quantum mechanical phenomenon whereby a neutrino created with a specific lepton flavor (electron, muon or tau) can later be measured to have a different flavor.

The NO ν A (NuMI Off-axis ν_e Appearance) long-baseline neutrino oscillation experiment, currently exploiting the oscillation concept, has in fact been designed to extend our knowledge about neutrinos. Through precision measurements of $\nu_e/\bar{\nu}_e$ appearance and $\nu_\mu/\bar{\nu}_\mu$ disappearance, NO ν A aims to provide constraints on θ_{13} , θ_{23} , $|\Delta m_{\text{atm}}^2|$, explore the neutrino mass hierarchy and constrain the CP violating phase.

NO ν A needs a high intensity, almost pure, ν_μ beam. Goal of this thesis is to study the NuMI (Neutrinos at the Main Injector) beam aiming at the optimization of the neutrino yield in NO ν A. An optimized neutrino yield is a fundamental requirement for all the neutrino experiments since neutrinos interact rarely with matter.

Chapter 1 gives a brief introduction about the history of neutrinos, then shows an overview of neutrino physics and neutrino oscillations.

Chapter 2 describes the whole NuMI beamline and explains how the neutrino beam at Fermilab is produced.

Chapter 3 describes the NO ν A experiment in details, designed as a finely segmented twin (near and far) detector offering superb event identification capability.

Chapter 4 explains how the beam line is modeled using Monte Carlo simulations, shows the new tools that have been implemented in the simulation and finally shows studies on the trajectories of ancestor particles that decays in neutrinos of the NuMI beam, mainly pions. Either positive or negative particles are focused thanks to a focusing system that is composed of two magnetic Horns in order to obtain a rather pure ν_μ or $\bar{\nu}_\mu$ beam.

Chapter 5 describes a simulation to understand how the neutrino yield at NO ν A changes if the Horn Current is decreased from the nominal value of 200 kA. The comparison with data taken in June 2015 with different values of the Horn Current is shown.

Conclusions and perspectives for NO ν A are given in the last Chapter.

1 | NEUTRINO PHYSICS

1.1 A BRIEF HISTORY ABOUT NEUTRINOS

Neutrino history is deeply rooted in the recognition of weak interactions¹. As early as 1896, Becquerel discovered the radioactivity of uranium. Three years later, Rutherford discovered that there were two different by-products, α and β . The emission of γ ray being discovered later. In 1914, Chadwick demonstrated that the β -spectrum was continuous, in contrast to α - and γ -rays which were unique in energy.

This was a surprising result and some years later Meitner demonstrated that the missing energy could not be ascribed to neutral γ -rays, which led to the idea that the missing energy could be explained by the existence of a new particle. A radical alternative explanation was suggested by N. Bohr: perhaps energy conservation held only in a statistical sense.

In order to escape from this deadlock and to work out spin statistics in β -decay, W. Pauli addressed an open letter to "Dear Radioactive Ladies and Gentlemen" attending a physics Conference at Tübingen in December 1930. He argued that the existence of a neutral weakly interacting fermion emitted in β -decay could solve the issue. He called this neutral fermion a neutron, with mass of the order of the electron. In June 1931, Pauli gave a talk at a meeting of the American Physical Society in Pasadena and reported for the first time on his idea. He did not have his talk printed, however, since he was still uncertain about his idea.

When J. Chadwick discovered in 1932 the neutron as we know it today, E. Fermi renamed the Pauli particle the *neutrino*. The first published reference to the neutrino is in the Proceedings of the Solvay Conference of October 1933. Fermi and Perrin independently concluded in 1933 that neutrinos could be massless.

The first milestone in a comprehensive theory of weak interactions was established in 1934 when Fermi formulated a theory of β -decay, now known as Fermi theory, in analogy with quantum electrodynamics.

¹ For a complete treatment see K. Winter, *Neutrino Physics* [77], C. Giunti and C. W. Kim, *Fundamentals of Neutrino Physics and Astrophysics* [41], and references therein.

Although the remarkable success of the Fermi theory left few in doubt of the neutrino's existence, none had yet been observed in interactions. In fact, predicting the strength of interactions, H. Bethe and R. Peierls claimed in 1934 that it might never be observed. Also advised by B. Pontecorvo in the early 1950s, F. Reines and C.L. Cowan searched for a way to measure inverse β -decay, in which an anti-neutrino can produce a positron according to the reaction:

$$\bar{\nu} + p \rightarrow n + e^+$$

After considering several methods, including a nuclear explosion, they settled on using the large flux of *electron anti-neutrinos* from a nuclear reactor at the Savannah River Nuclear Plant and 10 ton of equipment, including 1400 liters of liquid scintillators. This experiment was the first reactor-neutrino experiment. In June of 1956, Reines and Cowan sent a telegram informing Pauli of the discovery. Reines (Cowan passed away) was awarded the Nobel prize 40 years later.

In 1962, *muon neutrinos* were discovered by Lederman, Schwartz, Steinberger and coworkers at the Brookhaven National Laboratory. This experiment used a beam of protons focused toward a beryllium target. The resulting interaction produced a large number of pions which decayed to muons and muon neutrinos.

In 1973, the Gargamelle experiment at CERN discovered the weak neutral current interaction via $\nu_\mu + N \rightarrow \nu_\mu + \text{hadrons}$ and $\bar{\nu}_\mu + N \rightarrow \bar{\nu}_\mu + \text{hadrons}$, where N is a nucleon in the detector.

From there on, coupling of the leptonic charged current (CC) and neutral current (NC) with hadronic objects had to be depicted by Feynmann diagrams in Figure 1, involving the exchange of charged (W) or neutral (Z) gauge bosons.

Much later in 2001, the *tau neutrinos* were detected by the DONUT experiment. This experiment collided 800 GeV protons with a block of tungsten. This collision produced D_S mesons that subsequently decayed into tau-leptons which then produced tau neutrinos.

These and the experiments which followed confirmed the existence of three neutrino flavors: the electron neutrino (ν_e), the muon neutrino (ν_μ), and the tau neutrino (ν_τ).

As a branch of the neutrino history, in 1968 there was the first clue of neutrino oscillation: the Homestake experiment by Davis and coworkers measured the flux of neutrinos from the sun and detected a deficit when compared with the prediction of Bahcall's Standard Solar Model. This discrepancy was called the *solar neutrino problem*. The Davis experiment used a chlorine-based detector and radiological techniques to measure the flux of solar neutrinos interacting in the detector. This solar experiment was detecting electron neutrinos.

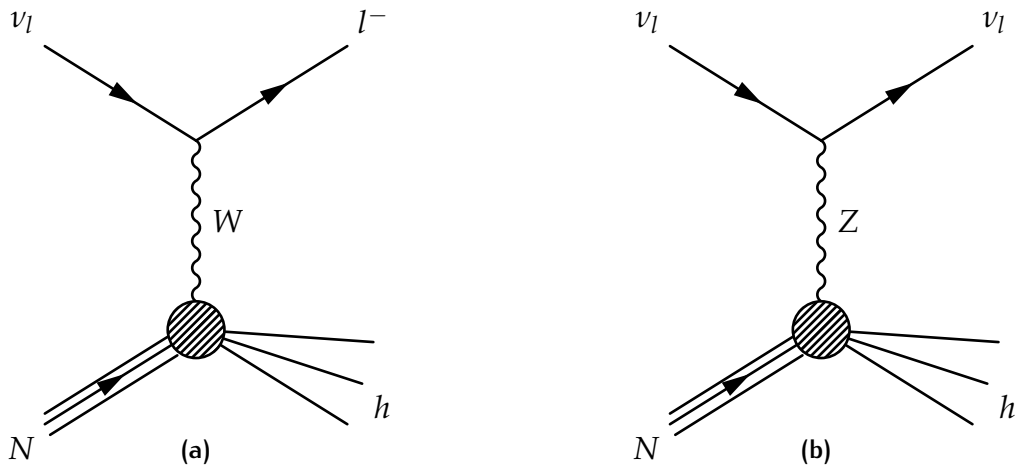


Figure 1: Feynman diagrams of W and Z exchange with a nucleon N . These examples show a deep inelastic scattering and the nucleon is then destroyed after the interaction, leaving a hadronic system h .

The same deficit was observed with muon neutrinos in atmospheric experiments. This happened in 1988 with the Kamiokande experiment.

In 1998, the Super-Kamiokande experiment used a cylindrical stainless steel tank with 50 ktons of water surrounded by 11,146 photomultipliers to detect neutrinos coming from the sun and the atmosphere. The revealed deficit in the angular and energy distribution was explained by neutrino oscillations.

In 2002, the SNO experiment made precise measurements of solar neutrinos. SNO is a heavy water Cherenkov detector in a nickel mine in Ontario (Canada) at a depth of 204 m of rock. The detector contained 1000 tons of D_2O . This experiment measured the electron and non-electron component of the solar neutrino spectrum by comparing the charged current and neutral current neutrino reactions on deuterium. The result from this experiment was a detailed confirmation of the flavor changing signature of neutrino oscillation.

In 2002, the KamLAND experiment found the first evidence for reactor $\bar{\nu}_e$ oscillations. KamLAND is a liquid scintillator anti-neutrino detector that measured the $\bar{\nu}_e$ flux from nuclear reactors at an average distance of 180 km. This experiment observed 258 events with an expected 365 ± 24 events for the case of no oscillations.

In 2010, the observation of a ν_τ particle in a ν_μ beam was announced by the OPERA experiment. The OPERA experiment has been designed to search for $\nu_\mu \rightarrow \nu_\tau$ oscillations in appearance mode through the detection of the τ -lepton produced in the ν_τ CC interactions. The detector is located at Gran Sasso, 730 km away from the source in Geneva. In 2015 the fifth ν_τ candidate event was

observed, [27].

No experiments that have been performed so far have detected conclusive deviations from the SM, except neutrino oscillation experiments, which have shown that neutrinos are massive and mixed. In the SM, this is not the case. This discovery has made the SM an effective theory of the yet unknown theory beyond the SM. The understanding of how the neutrinos would gain tiny masses and how they are mixed is an extremely challenging task to face. The answer must be found in a theory beyond the SM. Thus, the neutrino is playing the role of a messenger of the new physics beyond the SM.

The phenomenon of neutrino oscillation has been observed for neutrinos from many sources, the sun, reactors, cosmic ray interactions, and accelerator beams. While these experiments tell us about neutrino mixing angles and differences in the square of their masses, we still do not have a complete knowledge of neutrinos. Remaining questions are mainly the absolute mass of neutrinos (since oscillations are only sensible to the difference of the square of the masses), whether there is CP violation in the neutrino sector, their mass hierarchy and if they are Dirac ($\nu \neq \bar{\nu}$) or Majorana ($\nu = \bar{\nu}$) particles.

1.2 NEUTRINO OSCILLATIONS

Although the first evidence dates 1968, the concept of neutrino oscillations was first proposed in 1957 by Pontecorvo [64], in analogy with the $K^0 - \bar{K}^0$ oscillation phenomenon (M. Gell-Mann and A. Pais), in which the strangeness quantum number is oscillating. The oscillations are generated by the interference of different massive neutrinos, which are produced and detected coherently because of their very small mass differences. The theory of neutrino oscillations was finally settled in 1975-76 by S. Eliezer and A.R. Swift, H. Fritzsch and P. Minkowski, S.M. Bilenky and B. Pontecorvo as main contributors.

Neutrinos ν_α with flavour $\alpha = e, \mu, \tau$ are produced in particle decay and in charged-current (CC) weak interactions processes. Neutrinos of any flavour can also be produced in the neutral-current (NC) weak interaction process $Z \rightarrow \nu\bar{\nu}$. The CC processes are generated by the charged-current leptonic interaction Lagrangian, [41]:

$$\mathcal{L} = -\frac{g}{2\sqrt{2}} \left(j^\rho W_\rho + j^{\rho\dagger} W_\rho^\dagger \right) \quad (1)$$

where j^ρ is the leptonic charged current:

$$j^\rho = 2 \sum_{\alpha=e,\mu,\tau} \sum_k U_{\alpha k}^* \bar{\nu}_k \gamma^\rho l_\alpha \quad (2)$$

The leptonic charged current in eqn. (1) generates a superposition of massive neutrinos whenever the energies and momenta of the particles involved in the neutrino production process are not measured with a degree of accuracy allowing the determination, through energy-momentum conservation, of the emitted massive neutrino. This is the case for neutrino oscillation experiments, in which a flavor neutrino ν_α is a superposition of massive neutrinos ν_k with weights proportional to $U_{\alpha k}^*$.

1.3 NEUTRINO OSCILLATIONS IN VACUUM

Let us consider a neutrino with flavour α and momentum \mathbf{p} , produced in a CC weak interaction from a charged lepton l_α . In the standard theory of neutrino oscillations², the neutrino flavour state is described by:

$$|\nu_\alpha\rangle = \sum_k U_{\alpha k}^* \nu_k, \quad (3)$$

where U is the unitary mixing matrix, called PMNS (Pontecorvo, Maki, Nakagawa and Sakata) matrix. If we choose a finite normalization volume V , in order to have orthonormal massive neutrino states it must be

$$\langle \nu_k | \nu_j \rangle = \delta_{kj}.$$

The unitarity of the mixing matrix implies that also the flavour states are orthonormal:

$$\langle \nu_\alpha | \nu_\beta \rangle = \delta_{\alpha\beta}.$$

Since the massive neutrino states ν_k are eigenstates of the Hamiltonian, $\mathcal{H} |\nu_k\rangle = E_k |\nu_k\rangle$, with energy

$$E_k = \sqrt{\mathbf{p}^2 + m_k^2}, \quad (4)$$

² For a deep treatment of neutrino oscillations see C. Giunti and C. W. Kim, *Fundamentals of Neutrino Physics and Astrophysics* [41], and H. J. Lipkin, *Quantum theory of neutrino oscillations for pedestrians: simple answers to confusing questions* [50].

then the Schrodinger equation

$$i \frac{d}{dt} |\nu_k(t)\rangle = \mathcal{H} |\nu_k(t)\rangle,$$

implies that the massive neutrino states evolve in time as plane waves:

$$|\nu_k(t)\rangle = e^{-iE_k t} |\nu_k\rangle. \quad (5)$$

Let us consider now a flavour state $|\nu_\alpha(t)\rangle$ which describes a neutrino created with a definite flavour α at time $t = 0$. From eqns (3) and (5), the time evolution of this state is given by

$$|\nu_\alpha(t)\rangle = \sum_k U_{\alpha k}^* e^{-iE_k t} |\nu_k\rangle, \quad (6)$$

such that

$$|\nu_\alpha(0)\rangle = |\nu_\alpha\rangle.$$

The massive states can be expressed in terms of flavor states inverting eqn (3):

$$|\nu_k\rangle = \sum_\alpha U_{\alpha k} |\nu_\alpha\rangle, \quad (7)$$

where the relation $U^\dagger U = \mathbf{1}$ has been used. Substituting the last relation into equation (6) one gets:

$$|\nu_\alpha(t)\rangle = \sum_{\beta=e,\mu,\tau} \left(\sum_k U_{\alpha k}^* e^{-iE_k t} U_{\beta k} \right) |\nu_\beta\rangle. \quad (8)$$

Hence, the superposition of massive neutrino states $|\nu_\alpha(t)\rangle$, a the pure flavor state given in eqn. (3) at $t = 0$, becomes a superposition of different flavor states at $t > 0$. As it turns out that the mixing matrix U is not diagonal: neutrinos are mixed. The amplitude of $|\nu_\alpha\rangle \rightarrow |\nu_\beta\rangle$ transitions as a function of time is given by:

$$A_{\nu_\alpha \rightarrow \nu_\beta}(t) \equiv \langle \nu_\alpha | \nu_\beta \rangle = \sum_k U_{\alpha k}^* U_{\beta k} e^{-iE_k t}.$$

And the transition probability is then given by:

$$P_{\nu_\alpha \rightarrow \nu_\beta}(t) = |A_{\nu_\alpha \rightarrow \nu_\beta}(t)|^2 = \sum_{k,j} U_{\alpha k}^* U_{\beta k} U_{\alpha j} U_{\beta j}^* e^{-i(E_k - E_j)t}.$$

For ultra-relativistic neutrinos, one could expand relation (4) considering $m_k \ll E$:

$$E_k \simeq E + \frac{m_k^2}{2E}, \quad (9)$$

where $E = |\mathbf{p}|$. Given the mass difference Δm_{kj}^2 it is then possible to write:

$$E_k - E_j \simeq \frac{\Delta m_{kj}^2}{2E}.$$

In neutrino oscillation experiments, the propagation time t is not measured. What is known is the distance L between the source and the detector. Since ultra-relativistic neutrinos propagate almost at the speed of light, it is possible to approximate $t = L$ (see Section 1.3.1). Therefore, the transition probability can be approximated by:

$$P_{\nu_\alpha \rightarrow \nu_\beta}(t) = \sum_{k,j} U_{\alpha k}^* U_{\beta k} U_{\alpha j} U_{\beta j}^* e^{-i \frac{\Delta m_{kj}^2 L}{2E}}. \quad (10)$$

The oscillation probability thus depends both on quantities fixed by nature (PMNS matrix elements and differences of the square of the masses Δm^2) and on parameters fixed by experiments (the path the neutrino travels L , i.e. the source-detector distance, and the neutrino energy E) Moreover, the oscillation experiments are only sensitive to the difference of the squares of the masses and not to the absolute neutrino mass.

The transitions among different flavors manifest for $L > 0$, because the unitarity relation

$$UU^\dagger = \mathbf{1} \quad \iff \quad \sum_k U_{\alpha k} U_{\beta k}^* = \delta_{\alpha\beta},$$

implies that

$$P_{\nu_\alpha \rightarrow \nu_\beta}(L = 0, E) = \delta_{\alpha\beta}.$$

It is possible to show that:

- The sum of the probabilities of transition from a flavor neutrino ν_α to all flavor neutrinos ν_β is equal to unity:

$$\sum_{\beta} P_{\nu_\alpha \rightarrow \nu_\beta}(L, E) = 1.$$

- The sum of the probabilities of transition from any flavor neutrino ν_α to a flavor neutrino ν_α is equal to unity:

$$\sum_{\alpha} P_{\nu_\alpha \rightarrow \nu_\beta}(L, E) = 1.$$

1.3.1 General remarks

The main assumptions adopted in the standard derivation of the neutrino oscillation probability can be summarized as follows.

- Flavour neutrinos have a definite momentum \mathbf{p} , i.e. all the massive neutrino components have the same momentum. This is also called the *equal momentum assumption*. In principle, there is no justification for this assumption. However, it is possible to see that the equal momentum assumption is irrelevant in the derivation of the oscillation probability.
- The propagation time t is equal to the distance L traveled by the neutrino between production and detection. This is called the *light-ray approximation*. This assumption is unjustified in a plane-wave treatment of oscillations, because plane waves extend with the same amplitude over the whole space-time. However, in quantum theory, localized particles are described by wave packets. In fact, neutrinos are described by wave packets that are localized in the production process at the production time and propagate between the production and the detection processes with a group velocity close to the velocity of light, justifying the approximation $t = L$.

1.3.2 PMNS matrix

In the standard picture of neutrino oscillations with three active neutrino flavors and no sterile states the 3×3 PMNS matrix is written in the form:

$$\begin{pmatrix} |\nu_e\rangle \\ |\nu_\mu\rangle \\ |\nu_\tau\rangle \end{pmatrix} = \begin{pmatrix} U_{e1} & U_{e2} & U_{e3} \\ U_{\mu1} & U_{\mu2} & U_{\mu3} \\ U_{\tau1} & U_{\tau2} & U_{\tau3} \end{pmatrix} \begin{pmatrix} |\nu_1\rangle \\ |\nu_2\rangle \\ |\nu_3\rangle \end{pmatrix} \quad (11)$$

The standard parametrization of PMNS mixing matrix in terms of three mixing angles and a CP-violating phase is given as follows:

$$\begin{aligned} U_{e2} &= \cos \theta_{13} \sin \theta_{12} \\ U_{\mu3} &= \cos \theta_{13} \sin \theta_{23} \\ U_{e3} &= \sin \theta_{13} e^{-i\delta_{\text{CP}}} \end{aligned} \quad (12)$$

with all other elements following by unitarity. The square of the elements of the PMNS matrix give the fractional flavor content, e.g. $|U_{e2}|^2$ is the fraction of ν_2 that is ν_e . Figure 2 gives this fraction for all the mass eigenstates.

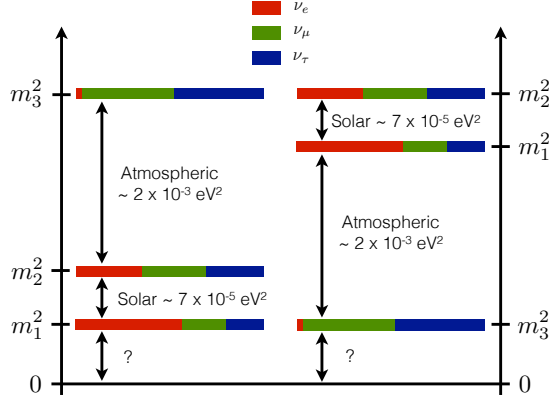


Figure 2: Pictorial representation of the possible neutrino mass hierarchies. Note: Δm_{atm}^2 is equivalent to Δm_{32}^2 and Δm_{sol}^2 is equivalent to Δm_{21}^2 .

Alternatively, it is possible to write:

$$\sin^2 \theta_{13} = |U_{e3}|^2, \quad \sin^2 \theta_{12} = \frac{|U_{e2}|^2}{(1 - |U_{e3}|^2)} \sim |U_{e2}|^2, \quad \sin^2 \theta_{23} = \frac{|U_{\mu 3}|^2}{(1 - |U_{e3}|^2)} \sim |U_{\mu 3}|^2, \quad (13)$$

where the \sim follows from the fact that $|U_{e3}|^2 \ll 1$ ³.

At the end one can write the PMNS matrix as follows:

$$U = \begin{pmatrix} c_{12}c_{13} & s_{12}c_{13} & s_{13}e^{-i\delta_{\text{CP}}} \\ -s_{12}c_{23} - c_{12}s_{23}s_{13}c_{12}s_{23} & c_{12}c_{23} - s_{12}s_{23}s_{13}e^{i\delta_{\text{CP}}} & s_{23}c_{13} \\ s_{12}c_{23} - c_{12}c_{23}s_{13}e^{-i\delta_{\text{CP}}} & -c_{12}s_{23} - s_{12}c_{23}s_{13}e^{i\delta_{\text{CP}}} & c_{23}c_{13} \end{pmatrix} \quad (14)$$

where $c_{ij} \equiv \cos \theta_{ij}$ and $s_{ij} \equiv \sin \theta_{ij}$. This matrix depends on: three mixing angles θ_{12} , θ_{13} , and θ_{23} , of which the first and last are the dominant angles for solar and atmospheric oscillations, respectively; a Dirac phase δ_{CP} that can induce CP-violating differences in the oscillation probabilities for conjugate channels such as $\nu_{\mu} \rightarrow \nu_e$ versus $\bar{\nu}_{\mu} \rightarrow \bar{\nu}_e$.

1.4 OSCILLATION PROBABILITY IN MATTER

Neutrinos propagating in matter are subject to a potential due to the *coherent* forward elastic scattering with the particles in the medium (electrons and nucle-

³ Day Bay reactor experiment measured $\sin^2 2\theta_{13} = 0.084 \pm 0.005$, [8].

ons). Coherent scattering happens when the neutrino wave function interacts with the matter as a whole, such as the scattered waves from the nuclei in the matter interfere with each other.

Neutrinos in matter are also affected by *incoherent* scattering with particles in the medium. In an incoherent scattering, the neutrino wave function scatters with each single nucleus independently in such a way that the scattered waves do not interfere, but they sum up incoherently. However, as shown below, this contribution can be neglected for artificial terrestrial neutrino sources.

Let us consider the cross section of a neutrino weakly interacting with a lepton or a hadron. From dimensional arguments, in the center of mass frame we get

$$\sigma \sim G_F s \quad (15)$$

where s is the Lorentz invariant Mandelstam variable which represent the squared center of mass energy and G_F is the Fermi constant: $G_F = 1.16 \times 10^{-5} \text{GeV}^{-2}$. Being s invariant, we can express it in the laboratory frame neglecting the neutrino mass. We get: $s = 2EM$, where E is the neutrino energy and M the mass of the lepton or the hadron. This yields:

$$\sigma \sim G_F E M \sim 10^{-38} \text{cm}^2 \frac{E M}{\text{GeV}^2} \quad (16)$$

We can now evaluate the mean free path λ of a neutrino traversing a medium with number density N of target particles:

$$\lambda \sim \frac{1}{N \sigma} \sim \frac{10^{38} \text{cm}^2}{(N \text{cm}^3) (E M / \text{GeV}^2)} \quad (17)$$

For neutrinos traversing the Earth's crust, the main target particles are nucleons with mass $M \sim 1 \text{ GeV}$ and number density $N \sim N_A / \text{cm}^3 \sim 10^{24} / \text{cm}^3$. So that:

$$\lambda_{\text{Earth}} \sim \frac{10^{14} \text{cm}}{(E / \text{Gev})} \quad (18)$$

If we take for example the NO ν A experiment, the neutrino energy is about 2 GeV. This yields $\lambda_{\text{Earth}} \sim 10^{14} \text{cm}$. Considering that the Earth diameter is about 10^9cm , we can conclude that the Earth is nearly transparent for neutrinos. Hence the contribution of incoherent scattering can be neglected.

When active flavor neutrinos propagate in matter, their evolution equation is affected by effective potentials due to the coherent interactions with the

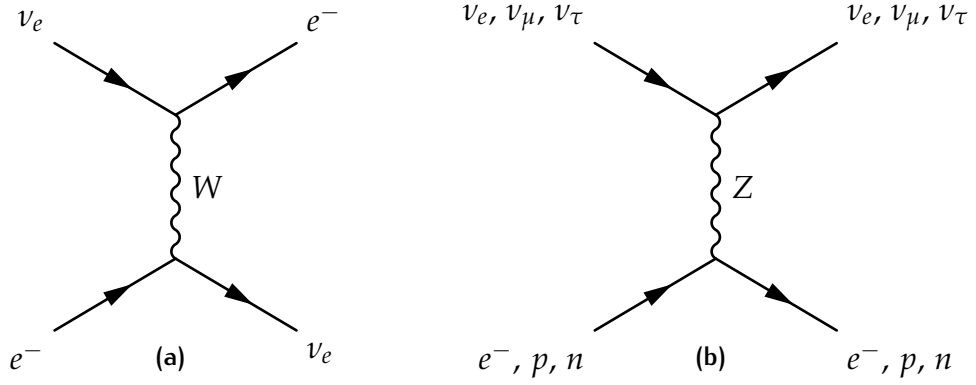


Figure 3: Feynman diagrams of the coherent forward elastic scattering processes that generate the CC potential V_{CC} through W exchange and the NC potential V_{NC} through Z exchange.

medium through coherent forward elastic weak CC and NC scatterings ([41], [55]). The Feynman diagrams of CC and NC scattering are shown in Figure 3. This phenomenon was first proposed by Wolfenstein [78] and is now known as the Mikheyev-Smirnov-Wolfenstein (MSW) effect.

To derive the MSW effect for the simplified case of two neutrinos (ν_μ, ν_e) let's start by expressing the Schrodinger equation as:

$$i \frac{d}{dL} \begin{pmatrix} \nu_e \\ \nu_\mu \end{pmatrix} = \left[U \begin{pmatrix} \frac{m_1^2}{2E} & 0 \\ 0 & \frac{m_2^2}{2E} \end{pmatrix} U^* + \begin{pmatrix} V_{CC} & 0 \\ 0 & 0 \end{pmatrix} \right] \begin{pmatrix} \nu_e \\ \nu_\mu \end{pmatrix} \quad (19)$$

where V_{CC} is the the additional component to the Hamiltonian from the charged-current coherent forward scattering of electron neutrinos off electrons. This factor takes the form

$$V_{CC} = \pm \sqrt{2} G_F N_e \quad (20)$$

with N_e being the number density of electrons in the medium, G_F is Fermi's constant, and the positive sign for neutrinos, the negative for anti-neutrinos.

The matrix in Equation 19 is the flavor basis Hamiltonian and can be diagonalized according to:

$$U_M^T H_F U_M = H_M \quad (21)$$

where H_M is the effective Hamiltonian in the mass basis in matter,

$$H_M = \frac{1}{4E} \begin{pmatrix} -\Delta m_M^2 & 0 \\ 0 & \Delta m_M^2 \end{pmatrix} \quad (22)$$

and U_M is the effective mixing matrix in matter,

$$U_M = \begin{pmatrix} \cos \theta_M & \sin \theta_M \\ -\sin \theta_M & \cos \theta_M \end{pmatrix} \quad (23)$$

From Equations 22 and 23,

$$\begin{aligned}\Delta m_M^2 &= \sqrt{(\Delta m_0^2 \cos 2\theta_0 \mp 2EV_{CC})^2 + (\Delta m_0^2 \sin^2 2\theta_0)^2} \\ \tan 2\theta_M &= \frac{\tan 2\theta_0}{1 \mp \frac{2EV_{CC}}{\Delta m_0^2 \cos 2\theta}}\end{aligned}\quad (24)$$

here Δm_0^2 and θ_0 denote the mass splitting and mixing angle in a vacuum and the sign for neutrinos, plus for anti-neutrinos. So the matter effect modifies the oscillation parameters based on the matter density and neutrino energy.

The effect of this coherent scattering results in an enhancement or suppression in the oscillation probability. See Section 3.1 for more details.

Taking account the matter effect, one can derive the expression for the oscillations probabilities.

The probability for $\nu_\mu \rightarrow \nu_\mu$ oscillation is [18]:

$$\begin{aligned}P_{\mu\mu} &= 1 - \sin^2 2\theta_{23} \sin^2 \Delta + \alpha c_{12}^2 \sin^2 2\theta_{23} \Delta \sin 2\Delta + \\ &\quad - \alpha^2 \sin^2 2\theta_{12} c_{23}^2 \frac{\sin^2 A\Delta}{A^2} - \alpha^2 c_{12}^4 \sin^2 2\theta_{23} \Delta^2 \cos 2\Delta + \\ &\quad + \frac{1}{2A} \alpha^2 \sin^2 2\theta_{12} \sin^2 2\theta_{23} \left(\sin \Delta \frac{\sin A\Delta}{A} \cos(A-1)\Delta - \frac{\Delta}{2} \sin(2\Delta) \right) + \\ &\quad - 4s_{13}^2 s_{23}^2 \frac{\sin^2(A-1)\Delta}{(A-1)^2} + \\ &\quad - \frac{2}{A-1} s_{13}^2 \sin^2 2\theta_{23} \left(\sin \Delta \cos A\Delta \frac{\sin(A-1)\Delta}{A-1} - \frac{A}{2} \Delta \sin 2\Delta \right) + \\ &\quad - 2\alpha s_{13} \sin 2\theta_{12} \sin 2\theta_{23} \cos \delta_{CP} \cos \Delta \frac{\sin A\Delta}{A} \frac{\sin(A-1)\Delta}{A-1} + \\ &\quad + \frac{2}{A-1} \alpha s_{13} \sin 2\theta_{12} \sin 2\theta_{23} \cos \delta_{CP} \sin \Delta \times \\ &\quad \times \left(A \sin \Delta - \frac{\sin A\Delta}{A} \cos(A-1)\Delta \right)\end{aligned}\quad (25)$$

The probability for $\nu_\mu \rightarrow \nu_e$ oscillation is:

$$\begin{aligned}
P_{\mu e} = & \sin^2 2\theta_{13} \sin^2 \theta_{23} \frac{\sin^2(A-1)\Delta}{(A-1)^2} + \\
& 2\alpha \sin \theta_{13} \cos \delta_{CP} \sin 2\theta_{12} \sin 2\theta_{23} \frac{\sin(A\Delta)}{A} \frac{\sin(A-1)\Delta}{A-1} \cos \Delta + \\
& - 2\alpha \sin \theta_{13} \sin \delta_{CP} \sin 2\theta_{12} \sin 2\theta_{23} \frac{\sin(A\Delta)}{A} \frac{\sin(A-1)\Delta}{A-1} \sin \Delta
\end{aligned} \tag{26}$$

where:

$$\begin{aligned}
\Delta & \equiv \frac{\Delta m_{31}^2 L}{4E} = 1.27 \frac{\Delta m_{31}^2 L \text{ (km)}}{E \text{ (GeV)}} \\
A & \equiv \frac{2EV}{\Delta m_{31}^2} = \frac{VL}{2\Delta}
\end{aligned} \tag{27}$$

and $V(x)$ is the potential:

$$V(x) \simeq 7.56 \times 10^{-14} \left(\frac{\rho(x)}{\text{g/cm}^3} \right) Y_e(x) \text{ eV}$$

where $\rho(x)$ is the matter density along the neutrino path and $Y_e(x)$ is the number of electrons per nucleon. For the Earth one has, to a very good accuracy, $Y_e \sim 0.5$. For many practical applications (such as long-baseline accelerator experiments, as well as oscillations of atmospheric, solar, and supernova neutrinos inside the Earth when they do not cross the Earth's core) it is a very good approximation to assume that the matter density along the neutrino trajectory is constant. Typical values for the matter density are $\rho_{\text{crust}} \sim 3 \text{ g/cm}^3$ in the Earth's crust and $\rho_{\text{mantle}} \sim 4.5 \text{ g/cm}^3$ in its mantle.

1.5 NEUTRINO MASS HIERARCHY

The now well-accepted picture of neutrino mixing involves three underlying mass states, with three mixing angles defining the linear superpositions that make up each of the three weak, or flavor, states. The magnitude of the mass-squared splitting between states ν_1 and ν_2 is known from the KamLAND reactor experiment, and the much-larger splitting between the third, ν_3 state and the $\nu_1 - \nu_2$ pair is known from atmospheric and long-baseline experiments. However, pure neutrino oscillations are sensitive only to the magnitude of the

mass splitting, not to its sign. Defining the ν_1 state as having the largest admixture of the electron flavor eigenstate, the sign of the mass splitting between states ν_2 and ν_1 is determined to be positive ($\Delta m_{21}^2 > 0$) using the pattern of neutrino oscillations through the varying-density solar medium. However, the corresponding sign of $\Delta m_{32}^2 \sim \Delta m_{31}^2$ remains unknown. That is, there are two potential orderings, or *hierarchies*, for the neutrino mass states: the so called *normal hierarchy*, in which ν_3 is the heaviest, and the *inverted hierarchy*, in which ν_3 is the lightest, as shown in Figure 2.

The long-baseline experiments have sensitivity to the neutrino mass hierarchy, due to the interaction of neutrinos with matter as they pass through the Earth. As the baseline itself is a critical factor for sensitivity, experiments are classified either as near term and relatively short baseline (like T2K [22] and NO ν A [61]), or as long-baseline experiment (DUNE, [11]). While T2K has very little sensitivity to the hierarchy, due to the short baseline, NO ν A has the potential to make a measurement at the $2 - 3\sigma$ level, dependent on the value of the CP phase parameter, δ_{CP} .

A combination of several experiments at different base-lines (e.g. T2K+NO ν A, or T2K/NO ν A+DUNE, etc) can disentangle the competing effects of CP violation and matter-induced neutrino-anti-neutrino differences, and thus improve the constraints in the hierarchy significantly beyond any single measurement.

1.5.1 Motivation for Determining the Neutrino Mass Hierarchy

Once we understand the ordering of the neutrino mass states, the uncertainty on a measurement of the CP-violating phase, δ_{CP} , is significantly reduced. Knowledge of the mass hierarchy would define the scope for future neutrinoless double beta decay ($0\nu\beta\beta$) experiments, seeking to resolve the mass nature of the neutrino, by limiting the domain for observation of a signal. In combination with cosmological measurements, which are sensitive to the sum of neutrino masses, knowledge of the mass hierarchy could also be used to determine the absolute mass scale of neutrinos. The mass hierarchy could also further understanding of core-collapse supernovae. For these many reasons, determination of the neutrino mass hierarchy is thus a fundamental step towards completion of the Standard Model of particle physics.

1.6 OVERVIEW OF NEUTRINO OSCILLATION EXPERIMENTS

It is possible to classify neutrino oscillation experiments into appearance and disappearance experiment:

APPEARANCE EXPERIMENTS These experiments measure transitions between different neutrino flavors, i.e. they look for the oscillation of $\nu_\alpha \rightarrow \nu_\beta$ measuring ν_β .

DISAPPEARANCE EXPERIMENTS These experiments measure the survival probability of a neutrino flavor by counting the number of tagged interactions in the detector and comparing it with the expected one. These experiments measure $\nu_\alpha \rightarrow \nu_X$, i.e. they see the oscillation but not the final product.

Another classification of neutrino experiments is based on the different sources of neutrinos that have been used. Natural sources, like solar or atmospheric neutrinos, are not enough to explore all the neutrino oscillation parameters.

REACTOR EXPERIMENTS These experiments exploit the large isotropic fluxes of electron anti-neutrinos produced in nuclear reactors by β^- decays of heavy nuclei (mainly fission fragments of ^{235}U , ^{238}U , ^{239}Pu , ^{241}Pu). A typical energy of reactor ν_e 's is of the order of a few MeV. Experiments of this type which have been performed in the past are: CHOOZ [25] and Palo Verde [3].

ACCELERATOR EXPERIMENTS These experiments make use of beams of neutrinos produced by decay of pions, kaons, and muons created by a proton beam hitting a target. These processes will be described in detail in the following.

ATMOSPHERIC NEUTRINO EXPERIMENTS Primary cosmic rays interact with the upper layers of the atmosphere producing a large flux of pions and kaons which decay in the atmosphere into muons and muon neutrinos. Many muons further decay into electrons and muon neutrinos before hitting the ground. Atmospheric neutrino experiments are designed to detect these ν_μ . The energy of detectable atmospheric neutrinos covers a very wide range, from about 500 MeV to about 100 GeV. The source-detector distance ranges from about 20 km for neutrinos coming from above, to about 10^4

km for neutrinos coming from below, initially produced on the other side of the Earth. Some atmospheric neutrino experiments which have been performed in the past are: Kamiokande [39], Super-Kamiokande [38], MACRO [24].

SOLAR NEUTRINO EXPERIMENTS These experiments detect the neutrinos generated in the core of the Sun by the thermonuclear reactions that power the Sun. Solar neutrino experiments are designed to detect these ν_e . Solar neutrino experiments are sensitive to extremely small values of Δm^2 , much smaller than the sensitivity of the other experiment discussed above. Several solar neutrino experiments have been performed in the past, like Kamiokande [40] and SNO [35].

Since the value of Δm^2 is fixed by nature, different experiments can be designed in order to be sensitive to different values of Δm^2 , by choosing appropriate values of the ratio L/E . The value of Δm^2 for which

$$\frac{\Delta m^2 L}{2E} \simeq 1$$

is called *sensitivity* to Δm^2 of an experiment. Different types of neutrino oscillation experiments are then classified depending on the average value of the ratio L/E . Considering only accelerator neutrino beam, it is then possible to categorize them into:

SHORT BASE-LINE EXPERIMENTS The range of L/E covered by these experiments and their sensitivity to Δm^2 are:

$$\frac{L}{E} \lesssim 1 \text{ km/GeV} \quad \implies \quad \Delta m^2 \gtrsim 1 \text{ eV}^2$$

Some experiments of this type which have been performed in the past are: BEBC [16], CDHSW [20], CHARM [19], CHORUS [17], NOMAD [31].

LONG BASE-LINE EXPERIMENTS These are experiments which have sources similar to SBL experiments, but the source-detector distance is about two or three orders of magnitude larger. They measure the atmospheric sector: Δm_{32}^2 . In this case:

$$\frac{L}{E} \lesssim 10^3 \text{ km/GeV} \quad \implies \quad \Delta m^2 \gtrsim 10^{-3} \text{ eV}^2$$

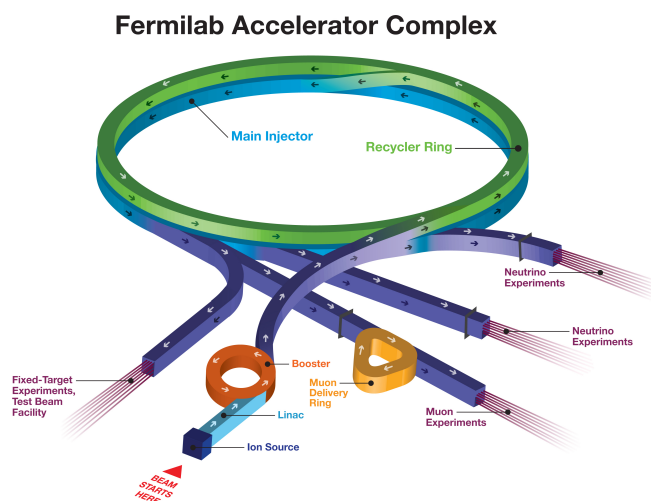
Some experiments of this type which have been performed in the past and in the present are: ICARUS [30], OPERA [26], T2K [22], MINOS [28] and NO ν A (see Chapter 3).

VERY LONG-BASELINE EXPERIMENTS These are accelerator neutrino experiments with a source-detector distance of the order of several thousands of km, comparable with the diameter of the Earth:

$$\frac{L}{E} \lesssim 10^4 \text{ km/GeV} \quad \implies \quad \Delta m^2 \gtrsim 10^{-4} \text{ eV}^2$$

These experiments are under study; new and more intense neutrino beams are needed in order to observe a sufficient number of events at such large distances.

2 | THE NUMI BEAM LINE



The Fermilab Accelerator Complex is composed of four accelerators that work in tandem [1]: the linear accelerator (linac), booster, recycler, and main injector. These accelerators produce two primary proton beams, a low energy (8 GeV) proton beam from the Booster and a high energy (120 GeV) beam from the Main Injector. Hitting a target, these proton beams produce secondary beams of pions, kaons, muons and neu-

trinos that serve a variety of experiments.

The Main Injector takes the 8 GeV energy protons from the Booster and accelerates them to 120 GeV. These highly energetic protons strike a carbon target to generate pions that subsequently decay to muons and muon neutrinos, resulting in the most intense neutrino beam in the world. The muon neutrino beam is used for studies of both the disappearance of muon neutrinos and the appearance of electron neutrinos. Three experiments currently gather data from the NuMI beam line.

The **MINOS** experiment [28] is a long-baseline neutrino experiment designed to observe the phenomena of neutrino oscillations. MINOS uses two detectors, one located at Fermilab, at the source of the neutrinos, and the other located 724 km away, in northern Minnesota, at the Soudan Underground Mine.

MINERvA [23] is a neutrino scattering experiment that seeks to measure low energy neutrino interactions both in support of neutrino oscillation experiments and also to study the strong dynamics of the nucleon and nucleus that affect these interactions.

The **NOvA** experiment, that can count on two detectors, one at Fermilab and one 810 km away at Ash River, Minnesota, will use the NuMI beam

to directly observe and measure the transformation of muon neutrinos into electron neutrinos by measuring the ν_e . NO ν A will also make important indirect measurements of the mass ordering of the three known neutrino types, which will be a key piece of information in determining the currently unknown masses of neutrinos.

NuMI is a tertiary beam resulting from the decays of pion and kaon secondaries produced in the NuMI target. Protons of 120 GeV are fast-extracted from the Main Injector (MI) accelerator and bent downward by 58 mrad toward Soudan, MN. The beam line is designed to accept 4.9×10^{13} protons per pulse (ppp). The repetition rate is 0.75 Hz, giving about 6×10^{20} protons on target per year, [7].

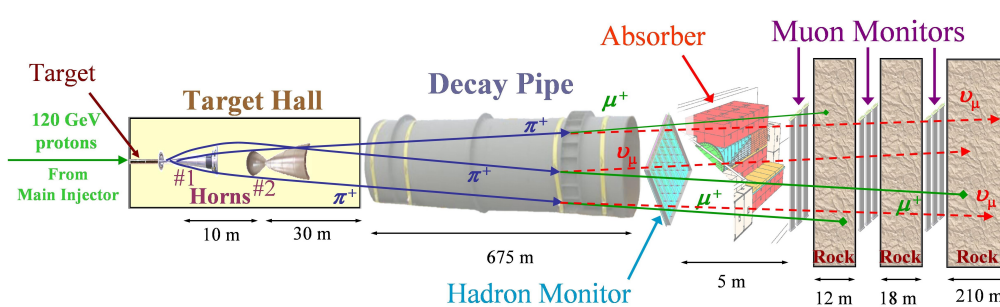


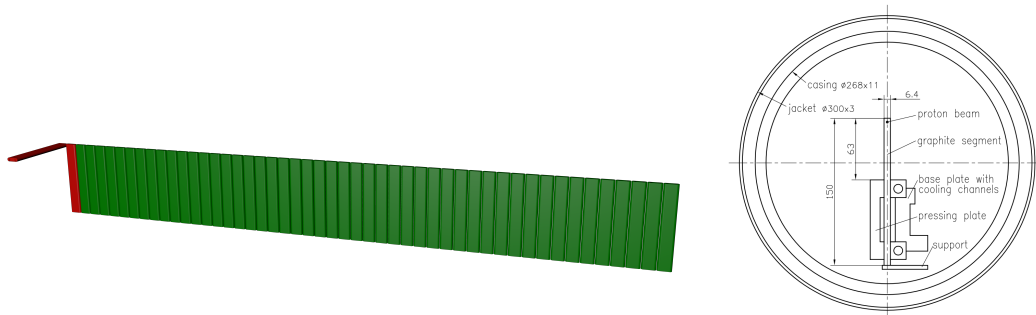
Figure 4: The NuMI Beam Line, [79].

2.1 THE TARGET

Protons accelerated in the Main Injector hit a graphite target. The protons interact with nucleons in the carbon and produce new particles, including pions, by far the main source of neutrinos and anti-neutrinos.

The target material is made of the ZXF-5Q graphite grade of Poco Graphite, Inc. which has a density of 1.78 g/cm^3 , [52]. The target consists of a total of 50 graphite segments. There are 48 graphite segments in the target core.

There are two uncoupled water cooling systems: the cooling system of graphite target segments and a second system to remove the energy deposited in the target casing. The latter will provide removal of the heat, deposited in the target casing by secondary particles, as well as the heat emitted from target segments tips. The cooling water runs along the target through a helical groove machined at the outer surface of casing, which is made of heavy-wall pipe. The target casing is covered by thin cylindrical jacket with inlet and outlet pipes.



- (a) Target core. The primary proton beam runs through the target from left to right. There are 48 segments in the target core, plus two additional Budal monitors (colored red) at the upstream end of the target.
- (b) Cross-section of the target.

Figure 5: NuMI Target.

The jacket is welded to the target casing at its both ends. The inside of the target casing is anodized to obtain the coefficient of emissivity. More detail description and main operation factors of the cooling system for the target casing are given below.

The dimensions of the graphite segments are described in [52]. One fin has a height of 150 mm (the extension out of the pressing plate is of 63 mm), a width of 7.4 mm and a depth of 24 mm. The ends of the segments are rounded with a 3.2 mm radius. The purpose of the gaps and rounded corners is to reduce the mechanical stress in the target material. The target width was reduced as much small as possible in order to maximize the flux of pions and still match the width of the beam.

In order to monitor the proton beam, the upstream end of the target is instrumented with two special fins as part of a Budal monitor. The Budal monitor is a charge-read-out monitoring system. There is a horizontal fin (for vertical position scans) and one additional vertical fin (for horizontal position scans). These two fins are colored in red in Figure 5a. Each of these fins are electrically isolated from the rest of the target. The vertical and horizontal fins are of the same dimensions as the main target fins. The gap between the vertical Budal fin and the first fin in the target core is 4.5 mm. The gap between the horizontal Budal fin and the vertical Budal fin is 5 mm. During normal operations, the proton beam will travel through both of the Budal fins, plus the other 48 fins of the target. A proton traveling down the center of the target will see a total of 1.2 meters ($= 50 \text{ segments} \times 24 \text{ mm/segment}$) of graphite material,

that corresponds to 2 interaction lengths. The total distance traveled from the upstream end of the target to the downstream end, including the gaps between the segments is 1.233 meters.

When the protons hit the target, secondary particles are produced. To enhance the neutrino beam, these secondaries are focused by the focusing system described in the next section.

2.2 FOCUSING SYSTEM

Simon van der Meer developed the idea of the *magnetic Horn* [76], a focusing device to collect the secondary pions and kaons from the target and directing them toward the downstream experiments, thereby increasing the neutrino flux.

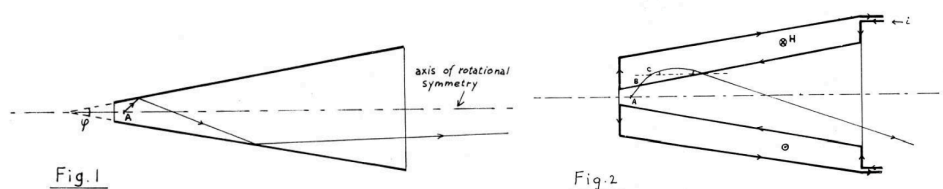


Figure 6: Van der Meer's schematic diagram of the neutrino Horn, [76].

The magnetic Horn consists of two axially-symmetric conductors with a current sheet running down the inner conductor and returning on the outer conductor [48], as shown in Figure 6. Between the conductors a toroidal magnetic field is produced whose $q\mathbf{v} \times \mathbf{B}$ force provides a restoring force for particles of one sign (π^+ or π^-), and defocuses particles of the other sign, thus enhancing a ν_μ beam while reducing $\bar{\nu}_\mu$ background, for example. The toroidal field produced is:

$$B(r) = \frac{\mu_0 I}{2\pi r}$$

where r is the radial distance from the beam axis. Ideally, for the Horn with perfect axial symmetry, the field outside of the Horns would vanish.

Different shapes for the inner conductor were ideated. Van der Meer's original Horn was a conical surface for the inner conductor. Such a device, shown in Figure 6, does a good job at focusing all momenta for a given angle of pion into the Horn. Later was conceived a magnetic Horn with parabolic-shaped inner conductors. In a parabolic Horn, the inner conductor follows the

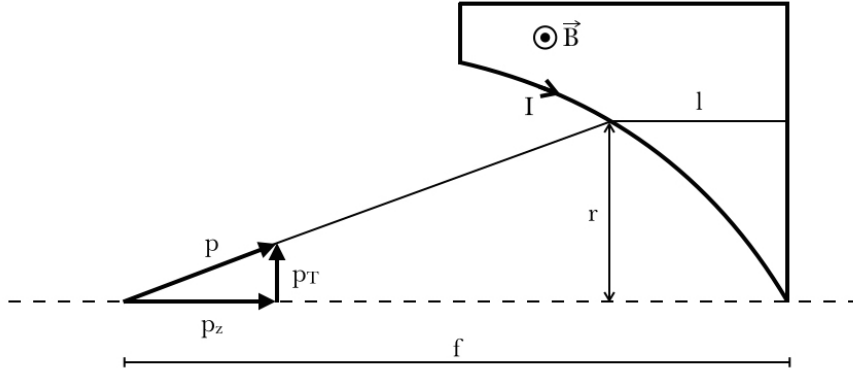


Figure 7: Schematic view of particles going through a focusing Horn with parabolic shape of inner conductor, [62].

curve $z = ar^2$ where z is the coordinate along the beam (or Horn) axis, and a is a parameter in cm^{-1} .

The amount of p_T kick that parabolic Horn gives to a particle, i.e. the variation of the transverse momentum of the particle, can be estimated by approximating the path of the particle inside the Horn with a straight line (as in Figure 7). Charged particles moving through the magnetic field inside the Horn feel the force $\mathbf{F} = q\mathbf{v} \times \mathbf{B}$. For the impulse-momentum theorem, the change in the momentum of the particle is equal to the impulse:

$$\begin{aligned} |\mathbf{J}| = |\Delta\mathbf{p}_T| &= \left| \int \mathbf{F} dt \right| = \left| q \int (\mathbf{v} \times \mathbf{B}(\mathbf{r})) dt \right| = \left| \int (d\mathbf{l} \times \mathbf{B}(\mathbf{r})) \right| \\ &= \int B(r) dl = B(r) l = \frac{\mu_0 I}{2\pi r} l \end{aligned} \quad (28)$$

because $q = \pm 1$ and $\mathbf{B} \perp \mathbf{l}$ in our approximation.

The Horn can be assimilated to a focusing lens. Its focal length can be found considering that the source is far away from the Horn: $r/f \approx p_T/p$. For perfectly focused particle, the Horn would cancel out its transverse momentum, so that $\Delta p_T = p_T$:

$$f \approx \frac{r}{p_T} p = \frac{2\pi}{\mu_0 I a} p. \quad (29)$$

From this we see that:

- the parabolic Horn works for all angles (within the limit of the small angle approximation), while the conical Horn works only with a "most likely angle" $\theta_{in} = \langle p_T \rangle / p$;

- a single parabolic Horn has a strong chromatic dependence (its focal length depends directly on particle momentum p).

2.2.1 Multi-Horn System

Multiple focusing elements can improve the neutrino flux because subsequent focusing elements can be used to "rescue" pion trajectories improperly focused by the first focusing element [48]. The idea of such devices was first noted by Palmer [58]. Such a multi-lens system was adopted at CERN PS neutrino beam and was also implemented for the CERN Antiproton Accumulator.

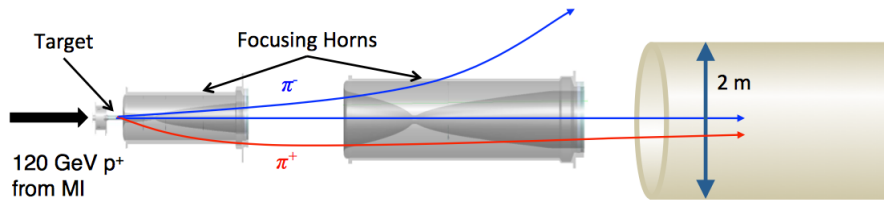


Figure 8: The NuMI Beam Line uses a two Horn focusing system.

The motivation for the multiple lenses is the following. A lens provides a definite " p_T kick" given by $\Delta\theta$ whose value can be calculated given the Horn shape, current, and the particle momentum p , as shown in eqn. 29. The Horn is tuned to give a p_T kick equal to this most probable entrance angle $\theta_{in} = \langle p_T \rangle / p$ into the Horn: $\Delta\theta = \theta_{in}$. Many particles emerging from the target will have a p_T not equal to the mean $\langle p_T \rangle$, resulting in particles, at the same momentum p , entering the Horn at a variety of angles. Assume we would like to focus all particles between $\theta_{in} = 0$ and $\theta_{in} = 2\theta_{in}$. A particle entering the Horn at θ_{in} will thus emerge from the Horn with outgoing angle $\theta_{out} = |\theta_{in} - \Delta\theta|$.

A particle entering the Horn with $\theta_{in} = \theta_{in}$ will exit at $\theta_{out} = 0$, while a particle entering the Horn at either $\theta_{in} \sim 0$ or $\theta_{in} = 2\theta_{in}$ will emerge with an angle $\theta_{out} = \theta_{in}$. A particle beam entering the Horn with angular divergence $2\theta_{in}$ will emerge with divergence θ_{in} .

A second lens far from the first will see a point source of particles with a span of angles 0 to θ_{in} . It would be likewise expected to halve the divergence of the beam. Its inner aperture should be larger so as to leave unperturbed those particles already well-focused by the first lens.

A detailed study of the performances of the NuMI double Horn focusing system is reported in Section 4.6 and in Chapter 5.

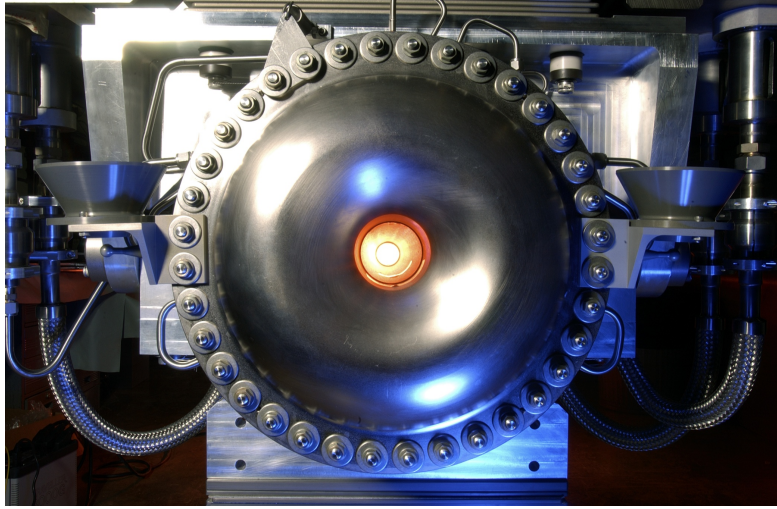


Figure 9: The NuMI magnetic horn.

2.2.2 NuMI Horns

The NuMI Horns geometry is shown in Figures 11a and 11b, while a picture of the NuMI Horn is shown in Figure 9. Tables 1 and 2 show the Horn dimensions for both the inner and outer conductors.

The NuMI Horns were designed to sustain currents of up to 200 kA producing the field of up to ~ 3 T in the narrowest part, inside the Horn field region.

Since the Horn heats up due to the pulsed current and radiation, during running the inner conductor is being cooled with nozzles that spray water on it. The Horns have a small field free region, called the neck of the Horn. The particles can pass through that region without being affected by Horns. The neck of second Horn is such that it allows the particles focused by first Horn to go through it without being further focused. These necks also allow the proton beam to go through without hitting the Horns.

When the pions travel through the Horn material, they can be scattered and this phenomenon must be taken under consideration because it will contribute to the uncertainty in the neutrino flux. To reduce this scattering process, the inner conductor is only a few millimeter thick. Anyway, one can consider a typical scattering angle [12] given by

$$\theta = \frac{13.6 \text{ MeV}}{p} \sqrt{\frac{x}{X_0}} \left[1 + 0.038 \ln \left(\frac{x}{X_0} \right) \right]$$

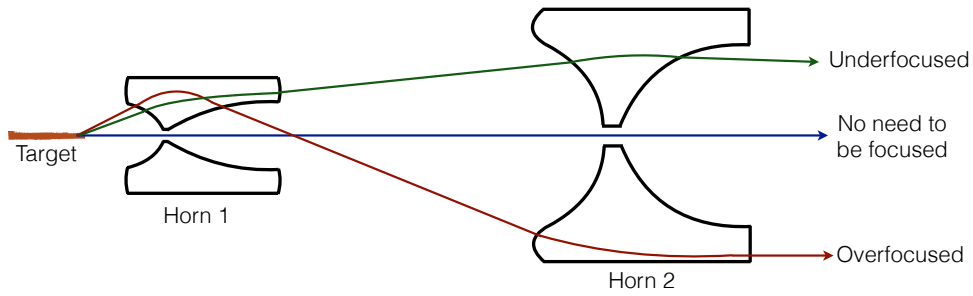


Figure 10: Schematic view of the target and the two Horns. Three pion trajectory examples are shown. Green: the particle has high momentum and it's only deviated by the Horn 1, Horn 2 is needed to correctly focus the particle. Red: the particle has low momentum and is over-focused by Horn 1, Horn 2 is needed to re-focus the particle. Blue: the particle goes straight through the neck of the Horns and doesn't need to be focused. Also other cases are possible: the particle only need Horn 1 or Horn 2 to be focused.

Since the Horns are made of Aluminum ($X_0 = 8.9$ cm), we have that for a 5 GeV pion $\theta = 3$ mrad.

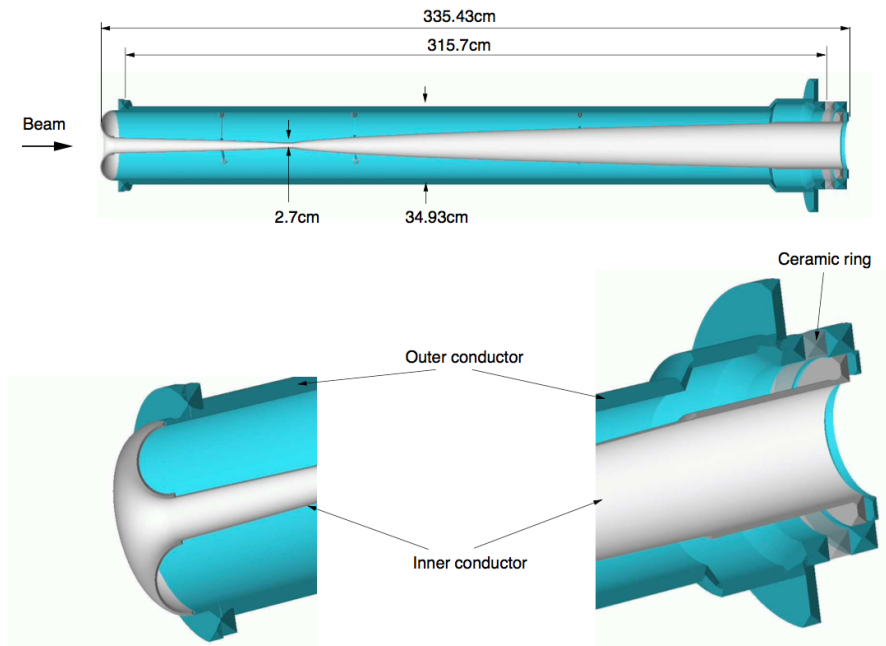
The second Horn is used to capture the particles that were improperly focused by the first Horn extending the focusing capabilities. Figure 10 shows the schematic view of target and Horns and 3 possible trajectories. The softest pions will come at the widest angle and will therefore be over-focused by the first Horn, but they will then get focused by the second Horn. Similarly, the pions that haven't received enough focusing by first Horn receive additional focusing by second Horn. Obviously, a two Horn system is capable of focusing a wider range of secondary momenta.

Table 1: Idealized dimensions of Horn 1 in cm. Subscripts IC and OC refer to inner and outer conductors, respectively, and *in* and *out* to the inside and outside surfaces of each conductor, [29].

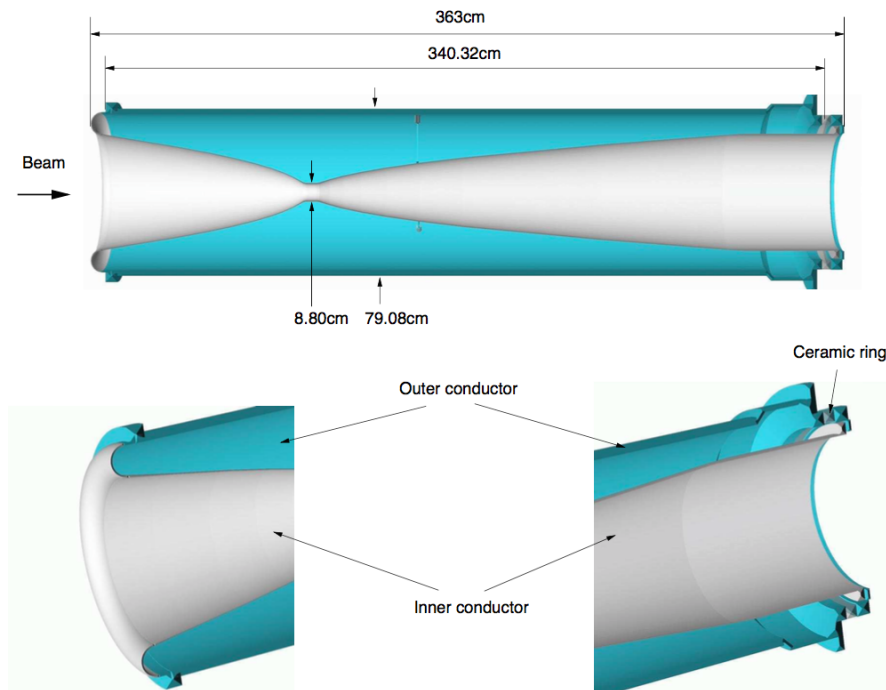
Z [cm]	Upstream		Neck	Downstream	
	0 – 44.047	44.047 – 80	80 – 83.982	83.982 – 95.128	95.128 – 300
R_{in}^{IC} [cm]	$\sqrt{\frac{92.8484-z}{7.0483}} - 0.2$	$\sqrt{\frac{85.7091-z}{7.0483}}$	0.90	$\sqrt{\frac{z-82.2123}{2.1850}}$	$\sqrt{\frac{z-80}{2.1850}} - 0.2$
R_{out}^{IC} [cm]	$\sqrt{\frac{92.8484-z}{7.0483}}$		1.35	$\sqrt{\frac{z-80}{2.1850}}$	
R_{in}^{OC} [cm]			14.92		
R_{out}^{OC} [cm]			17.46		

Table 2: Idealized Dimensions of Horn 2 in cm. Subscripts IC and OC refer to inner and outer conductors, respectively, and *in* and *out* to the inside and outside surfaces of each conductor, [29].

Z [cm]	Upstream	Neck	Downstream
	0 – 97.617	97.617 – 104.803	104.803 – 300
R_{in}^{IC} [cm]	$\sqrt{\frac{100-z}{0.1351}} - 0.3$	3.90	$\sqrt{\frac{z-100}{0.2723}} - 0.3$
R_{out}^{IC} [cm]	$\sqrt{\frac{100-z}{0.1351}}$		$\sqrt{\frac{z-100}{0.273}}$
R_{in}^{OC} [cm]			37.0
R_{out}^{OC} [cm]			39.54



(a) NuMI first Horn, [62].



(b) NuMI second Horn, [62].

Figure 11

2.3 DECAY PIPE, HADRON ABSORBER AND MUON SHIELD

The particles emanating from target hall area enter the 675 m long steel pipe. The NuMI decay pipe is 2 m in diameter within a larger excavated tunnel. The decay pipe starts 46 m downstream of the NuMI target and is filled with He.

The pipe is embedded into concrete shielding, so the particles moving in the outward direction are stopped either in the walls of the pipe or in the surrounding shielding. Since the decay pipe and the surrounding concrete are heated by the energy deposition of off-angle particles, the temperature of the shielding is maintained by water cooling.

The length of the decay pipe is set by the decay length of a pion. $\text{NO}\nu\text{A}$ neutrinos come from pion that have approximately an energy of 5 GeV, and the decay length of such pion is $\gamma\beta c\tau = 336$ m. But the same NuMI beam line is also used for other on-axis experiments, like MINOS and MINER νA . Their neutrinos come from pions of 5 to 10 GeV of energy, and for a 10 GeV pion the decay length is about 560 m.

The absorber stops the hadron component of the beam, while neutrinos and some of the muons pass through it. The absorber is a box 5.5 m wide \times 5.6 m tall \times 8.5 m long. It essentially consists of 4.75 m long, water cooled, aluminum core. The core is surrounded by layers of steel blocks and a layer of concrete shielding.

The threshold in momentum for muons is 3 – 4 GeV. Muons with momentum less than this are absorbed. The muons remaining in the NuMI beam after the decay pipe and absorber are ranged out in the so-called muon shield, which simply consists of 240 m of solid dolomite rock between the absorber and the MINOS and $\text{NO}\nu\text{A}$ ND hall. Without a muon shield the Near Detector electronics would be overloaded.

3 | THE NO ν A EXPERIMENT



The *NuMI Off-axis ν_e Appearance* experiment [61] has been designed to study $\nu_\mu(\bar{\nu}_\mu) \rightarrow \nu_e(\bar{\nu}_e)$ oscillations.

NO ν A uses the NuMI (*Neutrinos at the Main Injector*) muon neutrino beam at Fermilab as its neutrino source. It consists of two detectors optimized to reveal electron neutrinos. The first detector (Near Detector, ND) is sited inside the Fermilab laboratory, 100 m underground, 1 km distant from the Main Injector. The second one (Far Detector, FD) is sited in northern Minnesota, on surface, about 810 km distant from Fermilab, see Figure 12. The ND is used to measure the prompt neutrino flux. Once the flux is known, it is extrapolated to the FD that allows to look for neutrino oscillations. Using these two identical detectors, NO ν A can mitigate uncertainties in neutrino flux, neutrino cross section, and event selection efficiency.

The experiment is designed to address a broad range of open questions in the neutrino sector through precision measurements of the $\nu_\mu(\bar{\nu}_\mu) \rightarrow \nu_e(\bar{\nu}_e)$ oscillation. NO ν A will provide constraints on θ_{13} , θ_{23} , $|\Delta m_{\text{atm}}^2|$. It will also provide constraints on the ordering of the neutrino masses (i.e. whether the ν_3 state is more or less massive than the other two) and the amount of CP violation present in the neutrino sector. NO ν A will understand these last two quantities for certain region of δ_{CP} only, as shown in the following.

Outside of these primary goals, NO ν A has other purposes. With a comparisons of $\nu_\mu \rightarrow \nu_e$ and $\bar{\nu}_\mu \rightarrow \bar{\nu}_e$ NO ν A will also look for evidence of new physics. In fact, although NO ν A is designed to be an appearance experiment (i.e. is designed to reveal ν_e), a measurement of ν_μ events will be performed. NO ν A will provide constraints on sterile neutrino models by measuring the total flux of active neutrinos at its downstream detector. Neutrino-nucleus cross section measurements will be performed with a narrow-band beam. The two detectors can be used as a monitor for supernova neutrino activity. Finally, a variety of non-neutrino topics including searches for magnetic monopoles and hidden sector particles will be explored.

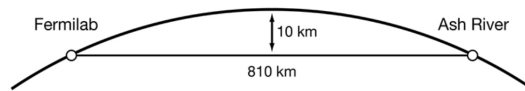
THE NO ν A EXPERIMENT



Figure 12: Positions of the NO ν A Near and Far Detectors. The Near Detector is sited at Fermilab while the Far Detector is in Minnesota, near Ash River.

3.1 A LONG-BASELINE EXPERIMENT

Before reaching the FD, neutrinos travel for 810 km in the Earth's crust. Neutrinos propagating in matter are subject to a potential due to the coherent forward elastic scattering with the particles in the medium (electrons and nucleons).



This is a key point for the NO ν A experiment, since this interaction differentiates the oscillation probability between a neutrino and an anti-neutrino beam. In this way NO ν A is potentially able to discriminate between the normal and the inverted hierarchy of the neutrino masses.

When neutrinos propagate through the Earth, coherent charged-current forward scattering of electron-type neutrinos with electrons in the Earth induces a significant change in the oscillation probabilities. These matter effects have opposite sign for neutrinos and anti-neutrinos and for normal versus inverted neutrino mass orderings. If the experiment is performed at the first oscillation peak, the matter effects are primarily a function of the energy of the neutrino beam and the transition probability in matter can be approximated by [7]:

$$P_{\text{mat}}(v_{\mu} \rightarrow v_e) \sim \left(1 \pm \frac{E}{6 \text{ GeV}}\right) P_{\text{vac}}(v_{\mu} \rightarrow v_e) \quad (30)$$

Two arguments thus emerge motivating the effort to set up a long baseline experiment [69]:

SENSITIVITY TO NEUTRINO MASS ORDERING Looking at eq. 30 it is possible to conclude that for the normal hierarchy, matter effects enhance (suppress) the transition probability for neutrinos (anti-neutrinos) and vice-versa for the inverted hierarchy. For the NO ν A experiment, matter effects give approximately a 30% enhancement or suppression in the transition probability.

THRESHOLD NO ν A has a baseline of 810 km. It would be a lot cheaper to have a 810 m baseline. With such baseline, all other things would be equal, but the neutrino flux will be a lot bigger: $\phi(\text{m})/\phi(\text{km}) = 10^6$. However, for atmospheric $\Delta m^2 \sim 2.5 \times 10^{-3} \text{eV}^2$ the oscillation maximum at $L = 810 \text{ m}$ is at $E = 1.47 \text{ MeV}$: well below ν_μ CC quasi-elastic threshold, that is $\sim 100 \text{ MeV}$.

3.2 NO ν A CAPABILITIES

NO ν A aims to perform measurements for three years with a ν_μ beam and three years with a $\bar{\nu}_\mu$ beam.

3.2.1 $\nu_e / \bar{\nu}_e$ Appearance

At the end NO ν A will essentially measure two probabilities: (i) the probability of the transition $\nu_\mu \rightarrow \nu_e$, $P(\nu_e)$ and (ii) the probability of the transition $\bar{\nu}_\mu \rightarrow \bar{\nu}_e$, $P(\bar{\nu}_e)$.

These two probabilities depend on both the mass hierarchy and the value of the CP-violating phase δ . It is convenient to plot the final result in a $P(\bar{\nu}_e)$ VS $P(\nu_e)$ graph.

In Figure 13 the values of the two probabilities are shown for different values of δ and for normal and inverted hierarchy.

Overlaid on the Figure are the expected 1σ and 2σ C.L. contours for a particular test point after six years of NO ν A running. This representation of the appearance measurements, though approximate, makes plain the nature of NO ν A 's hierarchy and CP violation sensitivity.

For example, no possible inverted hierarchy scenarios are included in the 2σ intervals for the test point shown, so the inverted hierarchy would be excluded by at least 2σ in this scenario. Figure 13a also demonstrates that the hierarchy

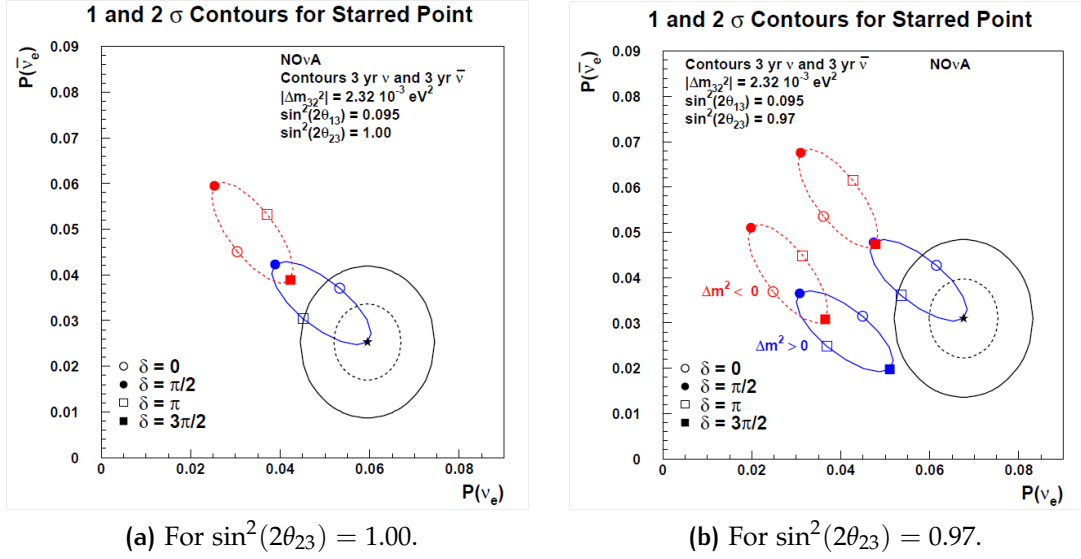


Figure 13: The ellipses show the δ values and choice of hierarchy that could yield from the oscillation probability measurements given $\sin^2(2\theta_{13}) = 0.095$. One can imagine that NO ν A makes a measurement of oscillation probability that yields the starred point. The contours are the 1 and 2 σ uncertainty on the starred point, [61].

can be established by NO ν A with a significance depending on the CP violating phase δ . This significance is shown explicitly as a function of δ in Figure 14a.

By the end of the primary NO ν A run, the T2K experiment will have a significant $\nu_\mu \rightarrow \nu_e$ oscillation data set of its own, and the appearance probabilities for T2K depend relatively little on the mass hierarchy [21]. Thus, potential degeneracies in the NO ν A measurement can be partially lifted by including T2K data. The combined sensitivity is shown in Figure 14b.

The estimates given so far have assumed $\sin^2(2\theta_{23}) = 1$. ν_μ disappearance measurements in the coming years, including those from NO ν A (see below), will provide increased precision on $\sin^2(2\theta_{23})$, and it is possible that non-maximal mixing will be established. Fig 13b shows how non-maximal mixing influences the NO ν A appearance measurements. In particular, the set of $\{P(\nu_e), P(\bar{\nu}_e)\}$ values that NO ν A can measure at 2 GeV is now described by four ellipses rather than two, with the higher (lower) probability cases corresponding to $\theta_{23} > \pi/4$ ($\theta_{23} < \pi/4$). Equivalently, the higher probability cases are those where the ν_3 state has more ν_μ than ν_τ admixture, and vice versa. This bifurcation in the set of possible outcomes allows NO ν A to make a measurement of this flavor

THE NO ν A EXPERIMENT

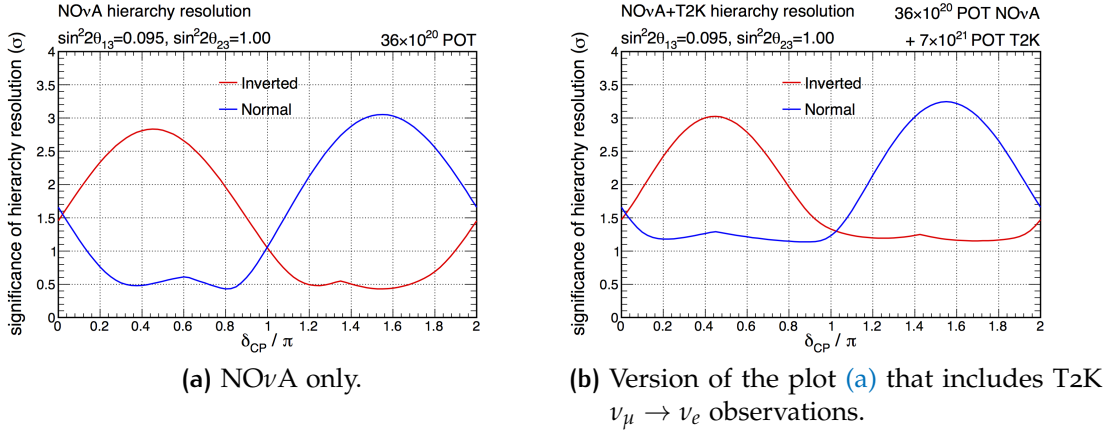


Figure 14: Significance with which NO ν A can resolve the mass hierarchy for the given values of $\sin^2(2\theta_{13})$ and $\sin^2(2\theta_{23})$ as a function of δ . This assumes a nominal 3+3 year run plan. The blue/solid (red/dashed) curve shows the sensitivity given a normal (inverted) hierarchy. The sensitivity goes to zero in this counting-only analysis at the delta values where the ellipses in Figure 13 intersect, [61].

balance (i.e. of the θ_{23} octant). If $\sin^2(2\theta_{23}) < 1$, then, the NO ν A appearance data will provide information on the mass hierarchy, δ_{CP} , and the θ_{23} octant simultaneously.

3.2.2 $\nu_\mu / \bar{\nu}_\mu$ Disappearance

While electron identification capability was a key feature in the design of NO ν A, the detectors also have excellent energy resolution for ν_μ charged current events, particularly for quasi-elastic interactions. In fact, NO ν A will make precision measurements of the atmospheric oscillation parameters $\sin^2(2\theta_{23})$ and $|\Delta m_{\text{atm}}^2|$ through ν_μ and $\bar{\nu}_\mu$ disappearance.

With the choice of a narrow-band 2 GeV spectrum and of a 810 km baseline, the ν_μ flux is largely oscillated away at the FD. Figure 15 shows the expected reconstructed energy spectrum for ν_μ and $\bar{\nu}_\mu$ CC quasi-elastic events after three years of ν running with an exposure of 18×10^{20} protons on target (POT). Both a maximal and a non-maximal mixing scenario are shown.

THE NOVA EXPERIMENT

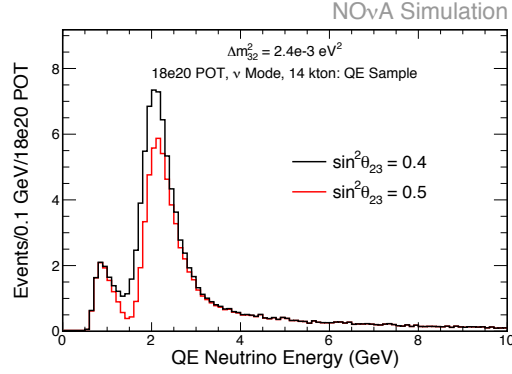


Figure 15: This plot shows the overlaid reconstructed energy spectra of all events selected in the contained QE sample for the ν_μ analysis with $\sin^2(2\theta_{23})$ equal to 0.4 and 0.5. It assumes 18×10^{20} POT in neutrino mode, [61].

3.3 AN OFF-AXIS EXPERIMENT

The advantage of siting an experiment off the center of the beam line is due to a feature of relativistic kinematics.

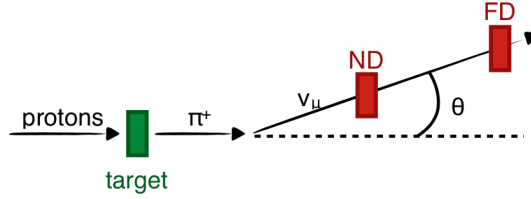


Figure 16: Schematic diagram of neutrino production (for a better description see Chapter 2). NOvA reveals neutrinos decayed from pions kaons and muons at an angle $\theta = 14.6$ mrad with respect to the beam line.

Let us consider the pion decay in a muon and a neutrino, Figure 16. We can describe this decay in the pion rest frame using the following notation¹:

$$\begin{aligned}
 p_\pi^* &= (m_\pi, \mathbf{0}) \\
 p_\nu^* &= (p^*, p^* \cos \theta, p^* \sin \theta, 0) \\
 p_\mu^* &= (m_\pi - p^*, -p^* \cos \theta, -p^* \sin \theta, 0)
 \end{aligned} \tag{31}$$

¹ Here and in the following, quantities with (without) a star denote quantities in the center of mass (laboratory) frame.

From the relation $m_\mu^2 = E_\mu^2 - \mathbf{p}_\mu^2$ we can derive the value of the neutrino energy in the center of mass frame:

$$p^* = \frac{m_\pi^2 - m_\mu^2}{2m_\pi} \quad (32)$$

To get the neutrino energy in the laboratory frame, we need to apply a Lorentz boost in the x direction, where the pion is moving. But first we need a relation between the angle θ^* in the pion frame and the angle θ in the laboratory frame. To do this, we can evaluate the tangent of θ in the following way:

$$\begin{aligned} p_v^\perp &= p_v \sin \theta = p^* \sin \theta^* \\ p_v^\parallel &= p_v \cos \theta = \gamma(p^* \cos \theta^* + \beta E_v^*) \approx \gamma p^* (\cos \theta^* + 1) \\ \implies \tan \theta &= \frac{p_v^\perp}{p_v^\parallel} = \frac{\sin \theta^*}{\gamma (\cos \theta^* + 1)} \end{aligned} \quad (33)$$

The last relation can then be re-written:

$$\cos \theta^* = \frac{1 - \gamma^2 \tan^2 \theta}{1 + \gamma^2 \tan^2 \theta} \quad (34)$$

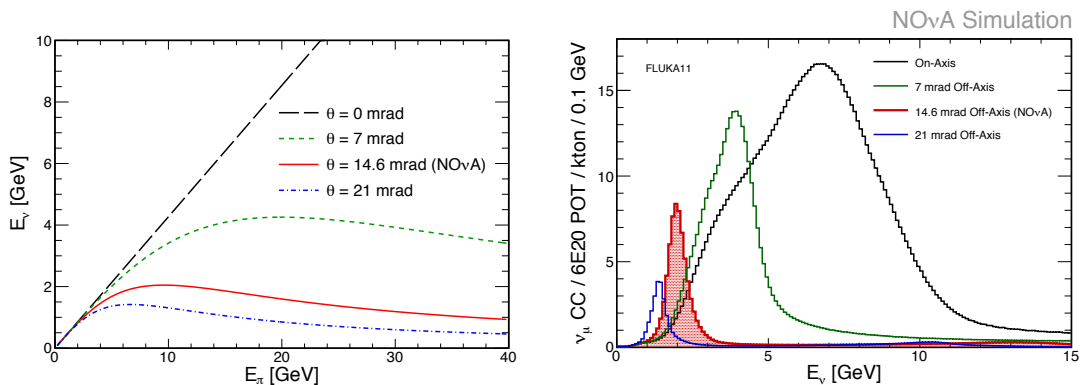
It is now possible to evaluate the value of the neutrino energy in the laboratory frame, as a function of the pion energy E_π and the angle θ :

$$\begin{aligned} E_v &= \gamma p^* + \beta \gamma p^* \cos \theta^* \\ &= p^* \left(\frac{E_\pi}{m_\pi} + \frac{|\mathbf{p}_\pi|}{m_\pi} \cos \theta^* \right) \\ &\approx p^* \frac{E_\pi}{m_\pi} (1 + \cos \theta^*) \\ &= p^* \frac{E_\pi}{m_\pi} \left(\frac{2}{1 + \gamma^2 \tan^2 \theta} \right) \end{aligned} \quad (35)$$

where we have used $E_\pi \approx |\mathbf{p}_\pi|$, valid for relativistic pions, and the relation (34). Finally:

$$E_v = \frac{1 - (m_\mu/m_\pi)^2}{1 + \gamma^2 \tan^2 \theta} E_\pi \quad (36)$$

Thus, while in an on-axis beam ($\theta = 0$) the energy of the neutrino is proportional to pion energy, in an off-axis beam the energy of the neutrino is less dependent on the pion energy and depends largely on the off-axis angle, yielding a tunable narrow-band beam. This is illustrated in Figure 17a.



- (a) The energy of neutrinos produced at various angles as a function of parent pion energy. At 14 mrad essentially all pion decays yield neutrinos in the 1-2 GeV energy range of interest for oscillations, compensating for the decrease in flux.
- (b) Simulated neutrino energy spectra for ν_μ charged current interactions in detectors sited 0, 7, 14, 21 mrad off the NuMI beam axis. NO ν A is sited at 14.6 mrad.

Figure 17

In Figure 17b the simulated neutrino energy spectrum is shown for different values of the off-axis angle. NO ν A is sited at $\theta = 14.6$ mrad corresponding to a quasi-monochromatic spectrum with neutrinos of about 2 GeV. The tail of the distribution is due to the K^+ decays that enhances the ν_μ spectrum between 10 and 15 GeV. The width of the distribution is due to the fact that not all the pions are perfectly focused (i.e. have zero transverse momentum).

Another important characteristic of an off-axis neutrino beam is that it allows to reduce the NC background. Being the beam almost monochromatic, high energy neutrinos producing NC events are largely absent. The ν_μ beam is not perfectly pure as there are contaminations of ν_e and $\bar{\nu}_\mu$. The ν_μ beam and the ν_e and $\bar{\nu}_\mu$ backgrounds are explained in more details in Section 4.3 where the neutrino flux is studied.

3.4 THE DETECTORS

The NO ν A detector is made of liquid scintillator which is both the interacting medium and the source of the light collected by front-end electronics. The detector mass is about 64% active because the scintillator is held in planes by

THE NO ν A EXPERIMENT



Figure 18: The NO ν A Near Detector. Credit: Fermilab.

PVC extrusions constituting separate cells. The NO ν A FD has a total of 344,064 PVC cells arranged in planes of 384 cells, in 896 layers with each cell 15.6 meters long.

When a charged particle is created from a neutrino interaction, it ionizes the liquid scintillator while traveling through it. The emitted light travels and it's reflected by the PVC walls until it arrives to the plastic wavelength shifting fibers. The signal then travels through the fiber reaching an avalanche photodiode. Front end electronics then convert and store the signal appropriately. Once collected, attenuation and calibration are applied to the signal turning it into energy units. Ultimately, the signal is stored in units equivalent to the amount of energy deposited by the charged particles in the cell.

The basic unit of all the NO ν A Detectors is a simple rectangular rigid PVC plastic cell containing liquid scintillator and a wavelength-shifting fiber [7], as illustrated in Figure 19. When charged particles traverse the cell, scintillator light is produced in the liquid. The light bounces around and it is captured by a wavelength-shifting fiber or absorbed by PVC or scintillator. The fiber is twice the length L of the cell and is looped at the bottom such that the captured light is routed in two directions to the end (top in the illustration) of the cell. Effectively there are two fibers in the cell, each with a nearly perfect mirror at the bottom so that nearly four times the light of a single non-reflecting fiber is captured. The NO ν A FD contains about 13,000 kilometers of wavelength shifting fiber, with each 15.6 m long cell containing a loop of about 33.5 meters.

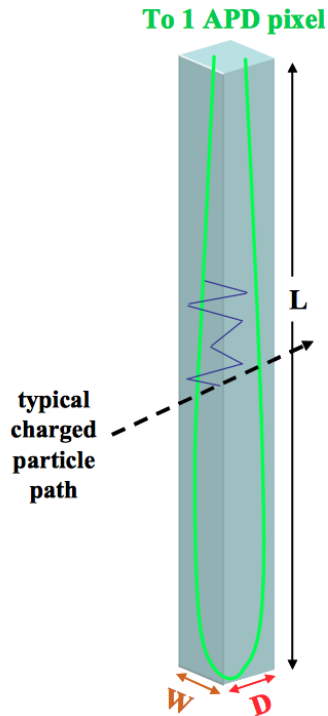


Figure 19: A PVC cell of dimensions (W , D , L) containing liquid scintillator and a wavelength-shifting fiber (green). A charged particle incident on the front face produces light (blue line) that bounces off the cell walls until absorbed by the fiber. The fiber routes the light to an APD. [7].

At the top of the cell both ends of the looped fiber are directed to one pixel on an Avalanche Photodiode (APD) photodetector array and the light is converted to an electronic signal.

Wavelength shifting provide an efficient method for collecting light generated in the long liquid scintillator filled cells of the detector. The violet light (~ 425 nm) emitted by the scintillator is absorbed by a fluorescent dye in the wavelength shifting fiber. The blue-green ($450 - 650$ nm) light emitted by the dye is partially trapped within the fiber by total internal reflection.

The 3.9 million gallons of liquid scintillator of the FD is composed primarily of mineral oil with 5.1% pseudocumene (1,2,4-trimethylbenzene) as the scintillant [36]. When excited by an ionizing particle, the primary scintillant pseudocumene decays by emitting photons in the range $270 - 320$ nm. These UV photons excite the wavelength shifter PPO (2,5-diphenyloxazole) which in turn decays and emit photons mostly in the range $340 - 380$ nm, with a tail that extends to 460 nm. In the third step in of this process, the down-converted

THE NOVA EXPERIMENT

scintillation photons excite the second wavelength shifter bis-MSB (1,4-bis-(o-methyl-styryl)-benzene) which subsequently decays to photons in the range 390 – 440 nm, with a tail that extends to 480 nm. Photons in the range 390 – 460 nm excite the wavelength shifter in the WLS fiber.

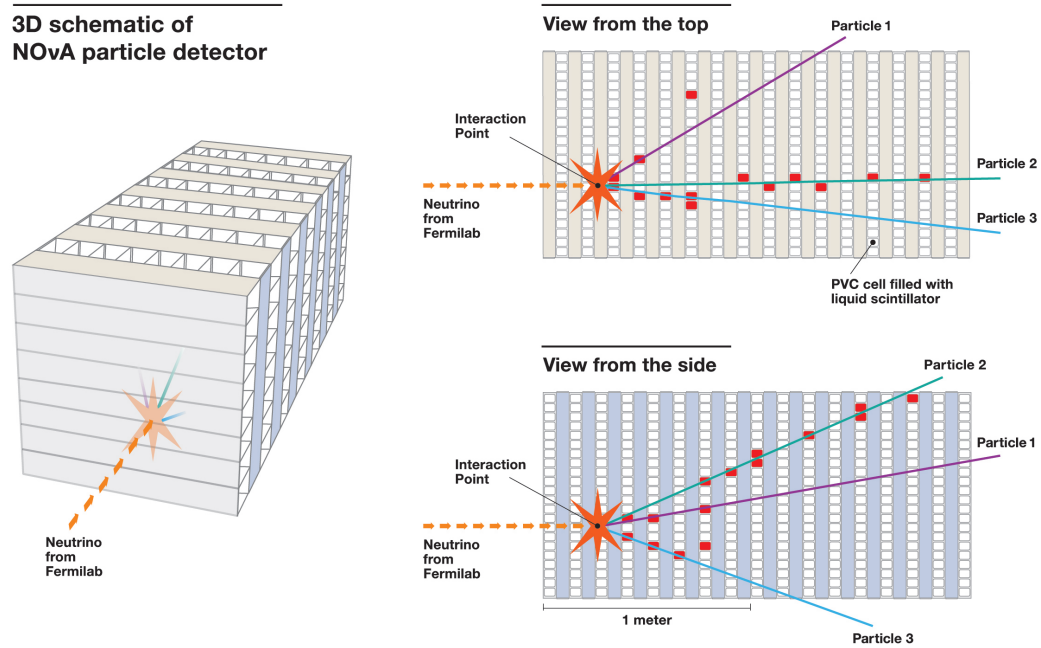


Figure 20: A graphic representation of one of the first neutrino interactions captured at the NOvA Far Detector in northern Minnesota. The dotted red line represents the neutrino beam, generated at Fermilab in Illinois and sent through 500 miles of earth to the Far Detector. The image on the left is a simplified 3-D view of the detector, the top right view shows the interaction from the top of the detector, and the bottom right view shows the interaction from the side of the detector. Credit: Fermilab.

4 | PREDICTION OF THE NEUTRINO FLUX

A prediction of the neutrino flux produced at the NuMI facility can be made using a Monte Carlo (MC) simulation fully including the whole beam line.

In Section 2.2 rough approximations of Horn focusing were adopted. Several effects need to be considered when calculating the actual trajectories of particles through the Horns. First, the target is an extended object located very close to the first Horn, breaking the point source approximation. Second, the Horns themselves are large objects extending over 3 meters along the beam axis. Finally, the particles have to pass through the Horn conductor, where multiple scattering occurs. MC calculations account for these effects, tracing individual particles through the magnetic fields in infinitesimal steps, deflecting particle trajectories or introducing scattering in the Horn material.

This chapter describes the Monte Carlo simulations used to predict the neutrino flux and the number of events at the NO ν A ND and FD. As part of this thesis work, a new tool was added to the simulation: the Ancestor List. This list contains the whole neutrino history, starting from the initial proton on target and ending with the neutrino. Once developed, the Ancestor List was used to track each single pion through the beam line to understand how the pion trajectories could affect the neutrino spectrum.

4.1 SOFTWARE FRAMEWORK

The official simulation software used by NO ν A to simulate the whole beam line is a combination of FLUKA ([13], [37]) and Geant4 [34]. This combination is made by FLUGG [67], a tool that add on to FLUKA to interface to Geant4 geometry. A simple model of incoming proton beam is used as a source of initial particles. The primary output of the this code is an `ntuple` representing the decays of secondaries that give rise to neutrinos.

The FLUGG simulation code falls into two broad categories: the simulation of the physical processes, made by FLUKA (FORTRAN) and the geometry description, written using Geant4 (C++). As an interplay of these two parts, FLUKA performs

particle interactions, tracks particle properties and writes output files, and whenever FLUKA goes to make a query about the geometry, the FLUGG code passes this query to Geant4, [45].

Besides FLUKA, a second simulator is used by the NO ν A experiment, based on Geant4 only: G4NuMI. The G4NuMI code builds up a representation of the NuMI beam line geometry and interfaces it with the Geant4 physics tools. G4NuMI and FLUGG make use of the same geometry. This software is often used to make cross checks with the FLUGG results. Although the studies shown in this chapter come from the FLUGG simulator, G4NuMI is used to make comparisons with FLUGG in Chapter 5, where the Horn Current studies are presented.

4.2 WEIGHTED MONTE CARLO

A method to accelerate the conventional procedure of neutrino production is discussed in this section, [54]. The idea is to replace the Monte Carlo neutrino kinematics and transport to the detector with an analytic calculation based up on a rotation and Lorentz transformation of each small solid angle that points to the detector into the rest frame of the decaying hadron. Key to this calculation is the fact that the relevant hadrons are pseudoscalar and thus decay with the resulting neutrino emerging isotropically in this rest frame. The solid angle subtended by the detector element in this frame divided by 4π gives the probability that the neutrino will pass through the particular detector element. The energy of the neutrino in the laboratory frame is also a unique multiple of its energy in the hadron rest frame.

The weight w that is needed is then the solid angle subtended by the detector element in this frame ($\Delta\Omega'$) divided by 4π :

$$w = \frac{\Delta\Omega'}{4\pi}$$

where the ' symbol denotes the hadron rest frame. This is the probability that a neutrino, generated from a pseudoscalar particle, points towards the center of the detector, see Figure 21.

Assuming that we know the solid angle in the laboratory frame, $\Delta\Omega$, what we need is the transformation that allows to evaluate $\Delta\Omega'$.

4 PREDICTION OF THE NEUTRINO FLUX

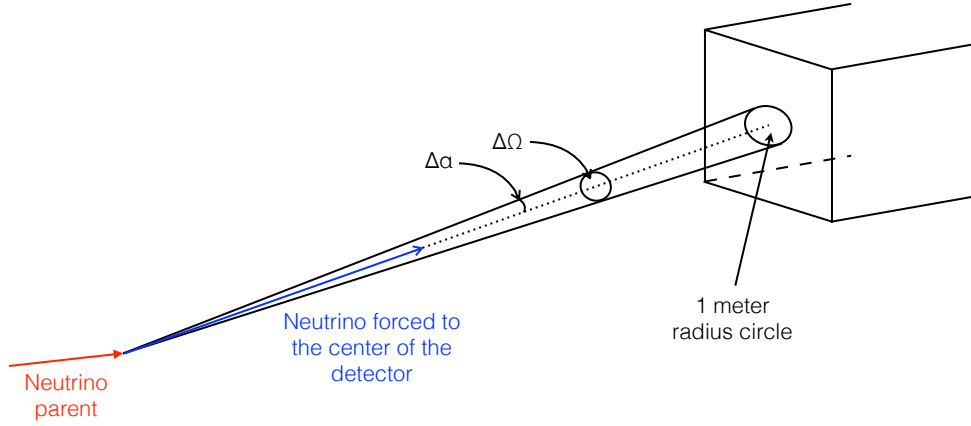


Figure 21: Schematic representation of hadron decaying in a neutrino forced to the center of the detector. See text for details.

4.2.1 The Lorentz Transformation

If $S(x, y, z)$ is the laboratory frame and $S'(x', y', z')$ the hadron rest frame, then the laboratory momentum components of the decay neutrino (E, \mathbf{p}) are related to those in the hadron rest frame by:

$$\begin{aligned} E &= \gamma(E' + \beta p'_z) \\ p_x &= p'_x \\ p_y &= p'_y \\ p_z &= \gamma(p'_z + \beta E') \end{aligned} \tag{37}$$

Without loss of generality one may assume the neutrino momentum has no x component. Further we assume that the neutrino is effectively massless. Let θ and θ' be the polar angles of the momentum vector \mathbf{p} in the laboratory and rest frame respectively, relative to the hadron flight direction. Defining

$$M = \frac{E}{E'} \tag{38}$$

we get from the eqs. in (37):

$$\begin{aligned} M \sin \theta &= \sin \theta' \\ M \cos \theta &= \gamma(\cos \theta' + \beta) \\ M &= \gamma(1 + \beta \cos \theta') \end{aligned} \tag{39}$$

Finally, from the last two eqs. in (39) one may eliminate $\cos \theta'$ to find:

$$M = \frac{1}{\gamma(1 - \beta \cos \theta)}$$

The transformation of solid angles is of particular interest because the neutrino is created isotropically in the hadronic rest frame. What we have is:

$$\frac{\Delta\Omega'}{\Delta\Omega} = \frac{\sin \theta' d\theta' d\phi'}{\sin \theta d\theta d\phi} = M \frac{d\theta'}{d\theta}$$

since the azimuth is unaffected by the Lorentz boost. One may show from eqs. (39) that $d\theta'/d\theta = M$ exactly, so:

$$\frac{\Delta\Omega'}{\Delta\Omega} = M^2. \quad (40)$$

The single boost parameter M then is sufficient to describe both the neutrino energy, eq. (38), and the solid angle transformation, eq. (40). Finally:

$$w = \frac{\Delta\Omega'}{4\pi} = \frac{1}{4\pi} M^2 \Delta\Omega = \frac{1 - \cos \alpha}{2} M^2 \quad (41)$$

where $\Delta\Omega = 2\pi(1 - \cos \alpha)$ and α is the angle shown in Figure 21.

4.2.2 Importance weight

The basic idea behind importance weighting is that we can save disk space and processing time by keeping only a fraction of the many lower energy particles and weighting that fraction up so that the weighted flux is unchanged. The idea is to more evenly distribute the statistics and processing time across energies, even though we produce many fewer high energy particles.

Given a particle with 4-momentum p produced in the simulation, the particle importance weight \tilde{W} is calculated as:

$$\tilde{W} = \frac{30}{|p [\text{GeV}]|}$$

Then, given the weight of the parent particle, W_{parent} , the final weight is

$$W = \tilde{W} \times W_{\text{parent}}.$$

In this way a parent's weight is passed down to its children, whose own additional weighting is applied to get their total weight.

If $W > 100$ the particle is discarded since it will not contribute to the flux in the energy range of interest. Then, a random number R , uniformly distributed between 0 and 1, is generated. If $R > 1/W$, the particle is discarded, otherwise is propagated. At the end of the simulation, every final neutrino will have a specific weight. In order to obtain an energy spectrum, it is necessary to scale each histogram entry with the importance weight W .

4.2.3 Implementation

FLUKA reads user input from an ASCII standard input file. The input consists of a variable number of commands, each consisting of one or more lines (called also cards). Each card has also different options the user can change called `WHAT(i)`. A typical FLUKA input file contains information like titles and comments for documentation purposes, definition of the materials, definition of the particle source and definition of the geometry. In our case the input file does not contain the geometry description, handled instead by Geant4.

The core of FLUKA is pre-compiled and frozen. There are however some user routine called by FLUKA in certain circumstances where the user can add his own code or modify an existing one. These user routines allow to define non-standard input and output, and in some cases even to modify to a limited extent the normal particle transport. Most of them are already present in the FLUKA library as dummy or template routines, and require a special command in the standard input file to be activated. Users can modify anyone of these routines, or insert into them further calls.

STUPRF (SeT User PProperties for FLUKA particles) routine is called before loading into stack hadrons, muons, neutrinos, low-energy neutrons, heavy ions and optical photons. A stack is a set of arrays containing all information about particles to be transported.

Importance weighting is performed by the NUWEIGHT function which is called by STUPRF. The algorithm is as follows. First, the code decides whether or not a particle should be importance weighted. Neutrinos, muons and kaons are not given any additional weight (though they may carry a weight greater than 1 from their parents). Particles with a total momentum above 30 GeV are also not given any additional weight. For the remaining particles, a candidate weight, W , is calculated.

4.3 FLUXREADER

The output of the FLUGG or G4NuMI simulation is called dk2nu (*decay to nu*) [44] flux file. This file contains all the relevant information about neutrino and neutrino parents. If one wants to skip the whole detector simulation, but just see the neutrino flux, or simply the flux with the cross section applied, then can use a recently developed software called *FluxReader* (FR from now onwards), [47].

FR is a framework designed to make distributions from dk2nu flux files. It is written in C++ in conjunction with the ROOT Data Analysis Framework [4].

In a nutshell, FR reads dk2nu flux files and outputs a set of spectra. This set of spectra will output the same variable for each specific neutrino flavor, parent species, applied cross section, and detector location. The user can configure almost everything, e.g.: flavors, parents, cross sections, detectors, binning, labels, variables, and weights to use to create output spectra.

To get the distribution of number of events at the detectors, FR creates a cross section spline by GENIE (a suite of products for the experimental neutrino community, [15]) to determine the appropriate cross section. To generate event rates, the neutrino weight is multiplied by this cross section value, and the results are summed over each neutrino ray for a total rate. Using an estimate that the detector is made of CH_2 , the final spectrum is scaled to have units of events per kton.

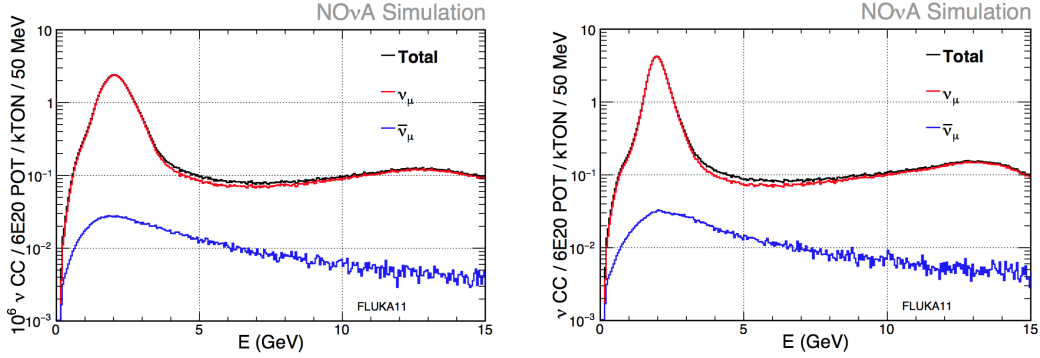
It is a very useful tool to see quickly how the neutrino spectra at the detectors look like, but it should be noted that:

- the flux is simulated at the center of the upstream face of the detectors (in a 1 meter radius circle), see Figure 21;
- it doesn't include the whole detector simulation;
- FR only deals with the true neutrino energy and not the reconstructed energy.

The two plots in Figure 22 show the neutrino energy distributions at the NO ν A ND and FD. At the ND, the 94% of the total spectrum is due to ν_μ events (98% in the [1, 3] GeV energy region). 3.7% is due to $\bar{\nu}_\mu$ and 2.2% due to $\nu_e + \bar{\nu}_e$. In the FD, the 68.7% of the total spectrum is due to $\bar{\nu}_\mu$ events. 10.4% is due to ν_μ and 0.90% due to $\nu_e + \bar{\nu}_e$.

The plot in Figure 23 was obtained using the FR framework. This Figure is part of a blessing package realized ad part of this thesis work, [73]. All

4 PREDICTION OF THE NEUTRINO FLUX



- (a) Neutrino spectra at the NOvA ND. The 94% of the total spectrum is due to ν_μ events (98% in the (1,3) GeV energy region). 3.7% is due to $\bar{\nu}_\mu$ and 2.2% due to $\nu_e + \bar{\nu}_e$.
- (b) Neutrino spectra at the NOvA FD. The 68.7% of the total spectrum is due to $\bar{\nu}_\mu$ events. 10.4% is due to ν_μ and 0.90% due to $\nu_e + \bar{\nu}_e$.

Figure 22: Event rate at the NOvA ND and FD. Also shown the wrong sign neutrino contamination ($\bar{\nu}_\mu$) and beam ν_e , [68].

distributions are plotted as a function of the neutrino true energy E_ν , but the neutral current one. It shows the ν_μ non-oscillated spectrum at the ND (dashed green), as well as the ν_μ spectrum in case of oscillation (solid green). The violet spectrum represents the ν_e events from oscillated ν_μ , while the magenta one represents events due to ν_μ beam contamination. Finally, the blue spectrum shows the neutral current events (due to all neutrino flavors), plotted VS the visible energy $E_\nu y$, where y is the Bjorken variable $y = (E_\nu - E'_\nu)/E_\nu$. To get the visible energy, the true energy has been re-weighted to get the visible one using a detector simulation, [73].

4.3.1 The off-axis angle

Eq. 36 is a good approximation for a perfectly focused pion beam and if pion decays happen all at the same point.

The exact calculation of the off-axis angle at the ND is not trivial. While the FD is so far away that it practically sees a point source of neutrinos, this is not true for the ND that sees a neutrino line source. Figure 24 shows the position along the beam line where the π^+ decay. The Figure shows only pions that are direct NOvA ν_μ parents. Decays occur all along the beam line and not all at the same point. Other factors must be considered when calculating

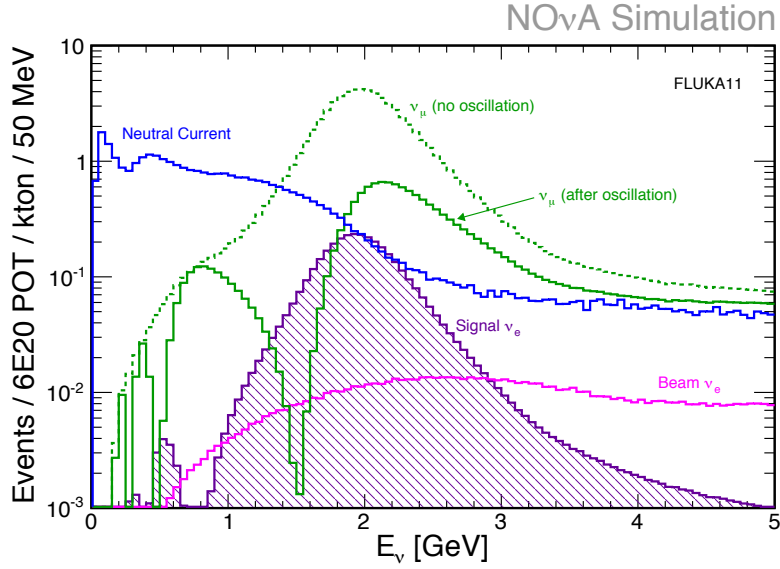


Figure 23: Raw signal and background rates for NOvA as a function of the neutrino true energy. The ν_μ rates are shown with (green dashed) and without (green solid) oscillations applied. In blue is shown the NC rates: they are shown as a function of the visible energy (=neutrino true energy * y). The magenta curve shows the intrinsic beam ν_e component. The violet bump shows the ν_e signal: this are ν_e oscillated form ν_μ , [73].

the off-axis angle, namely a transverse dispersion as well as the beam pipe in non-zero in radius and the detector face as an extension such that the off-axis angle evaluated from the left or right edge will give two different results.

To bypass this problem one can look at each single neutrino ray produced in the simulation as the ray is forced through the detector center point. For all these neutrinos, one can then evaluate the angle between the neutrino ray and the beam line. As explained before, each neutrino will have an importance weight and a location weight: the location weight is the probability that that neutrino will go toward the center of the detector. So at the end one can construct a distribution of neutrino angles w.r.t. the beam line, weighting each entry with the product of the importance and location weights.

The resulting distribution is shown in Figure 25 as the ν ray is forced toward the FD (25a) and the ND (25b). For the FD the mean of this distribution is 14.56 mrad. For the ND one gets 15.9 mrad, but with such a long tail that truncating it could give almost anything down to ~ 12 mrad.

4 PREDICTION OF THE NEUTRINO FLUX

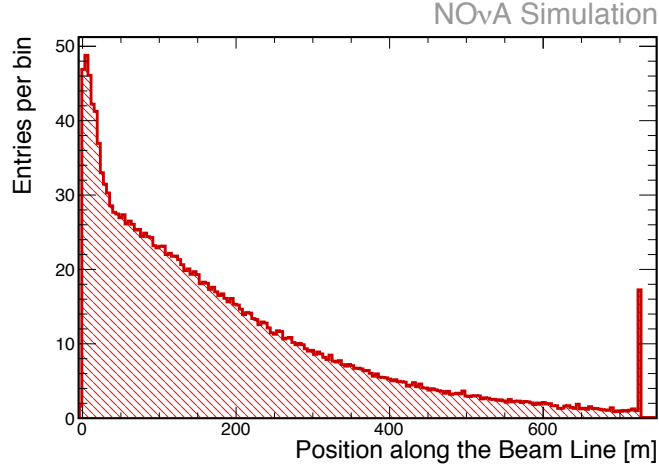


Figure 24: Decay points of π^+ that are direct ν_μ parents along the beamline. Only pions that will decay in NO ν A neutrinos were selected. The end of the focusing system (i.e. the end of Horn 2) is at 22 meters. The spike in the last bin is due to the presence of the hadron absorber.

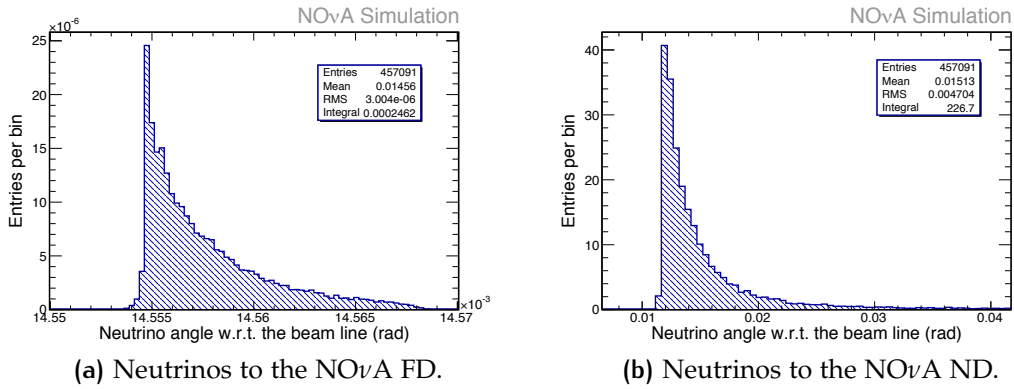


Figure 25: Neutrino off-axis angle for neutrinos directed to the NO ν A ND and FD.

4.4 THE ANCESTOR LIST

As part of this thesis work, an Ancestor List has been developed and implemented in FLUGG, [72]. The Ancestor List allows to keep track of each and every particle contributing to the neutrino flux: from the final neutrino to the initial proton.

During the particle transport, FLUKA keeps track of the interactions that lead to the production of any given particle. For every interaction, the material, vertex,

4 PREDICTION OF THE NEUTRINO FLUX

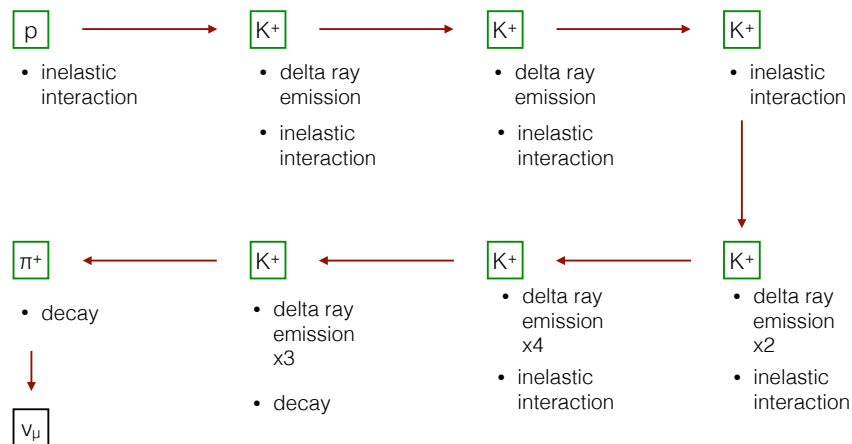


Figure 26: A neutrino history example.

momenta and identities of the outgoing particles are recorded. When a neutrino producing decay occurs, the interaction history that led to the production of the neutrino parents is reconstructed from this record and stored along with the neutrino information. The data of the primary proton that initiated the event are stored at the beginning of the interaction history record.

The information available from the interaction history enables a study of the contributions from various hadronic interactions leading to neutrino production and to tune the MC models based on available hadron production data.

This also allows to optimize the neutrino beam. As an example one can study which pions need just Horn 1, Horn 2, or both of them to be focused, and can find a better value for the magnetic field.

An example of a neutrino history is shown in Figure 26. There are a lot of delta ray interactions that, optionally, the user can exclude from the record. In the example shown, there are a number of inelastic interactions that happen mainly in the target, but that can also happen in some material present along the beam line, like the Horn material or any other beam line sustain.

4.4.1 Implementation

The FLUKA routine MGDRAW (MaGnetic Draw) is called at every step of the simulation. It is usually used to write a *collision tape*, i.e. a file where all or selected transport events are recorded. This routine has various entry points

called in different cases, in particular the subroutine USDRAW (User DRAW) called every time there is an interaction and used to create the Ancestor List, [72].

Every time USDRAW is called, all the relevant information about the particle having the interaction are saved. In particular, the particle unique identifier is saved. When a neutrino producing decay occurs, all the particles that contributed to the neutrino production are latched together using the unique identifier. This history is then saved on a text file. At the end of the simulation, the histories in the text file are written in the root file that will then be converted in dk2nu format.

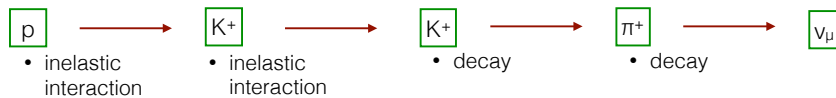
4.5 NUMBER OF INTERACTIONS OF THE NEUTRINO ANCESTORS

The Ancestor List was used for a variety of studies. This section describes some particular applications. One can use the Ancestor List to look at the number of interactions the ancestors had in their path.

Given a ν_μ directed toward the NO ν A ND, one can decompose the neutrino energy spectrum in term of the number of interactions the neutrino ancestors had. For example, a neutrino history with one interaction only is a history of this type:

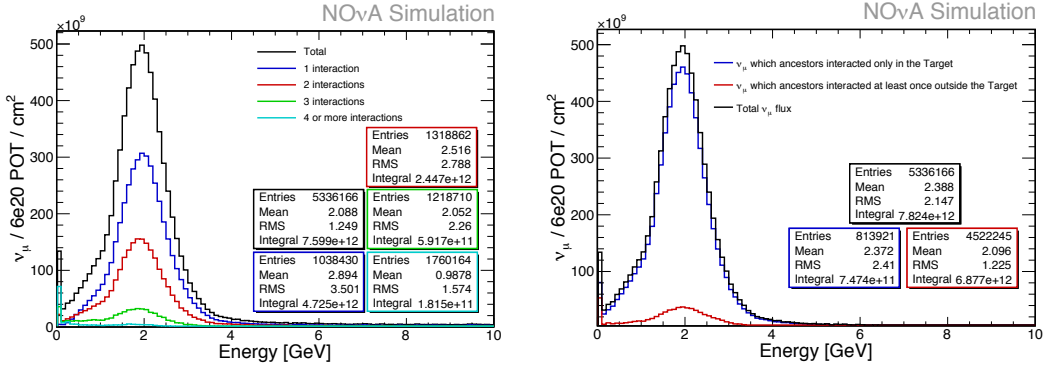


This history counts as one interaction since there is only a proton that interact with the material, while the others are just decays. A two interactions history example is provided by:



that counts as two interactions since there are the proton and the kaon that interact with the material. Also, delta rays and elastic scatterings do not count as interaction in this study.

4 PREDICTION OF THE NEUTRINO FLUX



(a) Decomposition in terms of the number of interactions the neutrino ancestors had in their path. (b) Decomposition in terms of neutrino which ancestors interacted once or at least once outside the target.

Figure 27: Decomposition of the ν_μ energy spectrum seen by the NO ν A ND.

The results of this study are shown in Figure 27a. The black distributions is the total ν_μ energy spectrum at the NO ν A ND. The blue spectrum is due to neutrinos which ancestors had only one interaction with the material. The two, three and more than three interaction cases are shown in red, green and cyan respectively.

A further study shows the distribution of the points, along the beam line, where the ancestors interacted. Considering only one interaction ancestors, the plot in Figure 28 shows in blue the end point of the proton where it interacts. In the same plot are also shown the identities of the particles that come out from that interaction and that belong to the neutrino history.

Figure 29a shows the end points of the ancestors for neutrinos with a two interaction history. The blue distribution shows the point where the proton interacts and the red one shows the point where the second ancestor interacts. Figures 29b and 29c show the identities of the particles that come out of the first and second interaction respectively.

The same study is performed for the three interaction case and is shown in Figure 30.

Since the Ancestor List stores the volume in which each interaction occurs, it is possible to understand the neutrino flux composition in term of how many neutrinos came from ancestors that interacted only in the target or that had some interaction with the material outside the target region. This flux decomposition is shown in Fig. 27b. It shows the total flux (black) at the NO ν A ND, but also the neutrino flux from neutrinos which ancestors interacted only

4 PREDICTION OF THE NEUTRINO FLUX

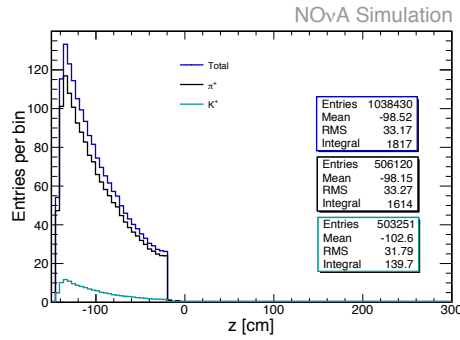
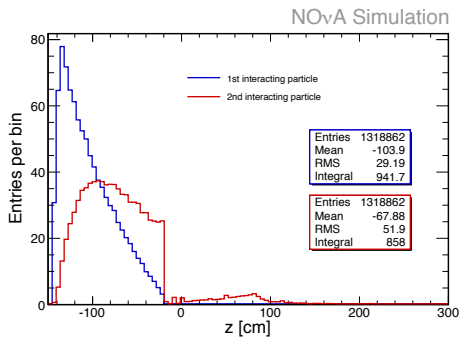
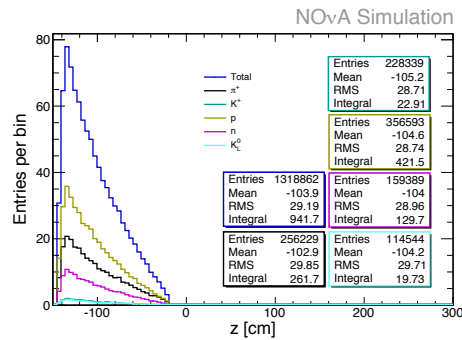


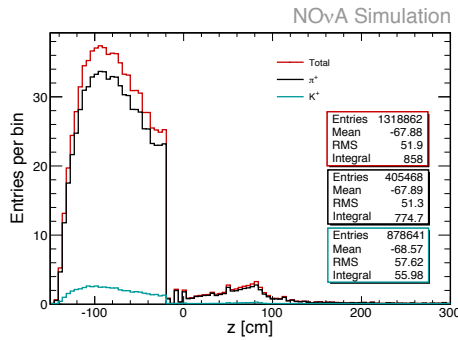
Figure 28: End point of the proton along the beam line (blue). Black and azure distributions show the identity of the particles coming out from the interaction of the proton. Only neutrino ancestors are shown.



(a) Proton end point is shown in blue. The end of the second particle that interacts is shown in red.



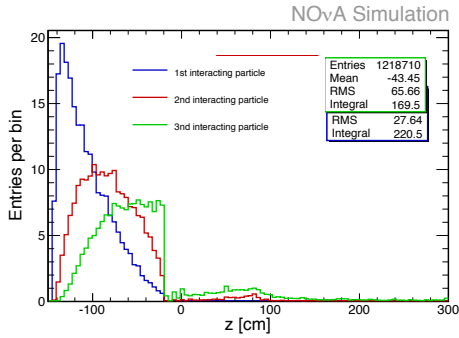
(b) Identities of the particles that come out form the first interaction.



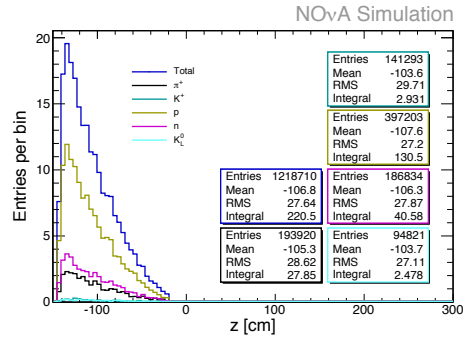
(c) Identities of the particles that come out form the second interaction.

Figure 29: End point of the ancestors that interacted with the material along the beam line for a two interaction case. See text for details.

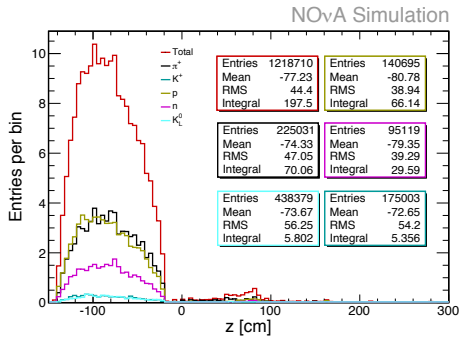
4 PREDICTION OF THE NEUTRINO FLUX



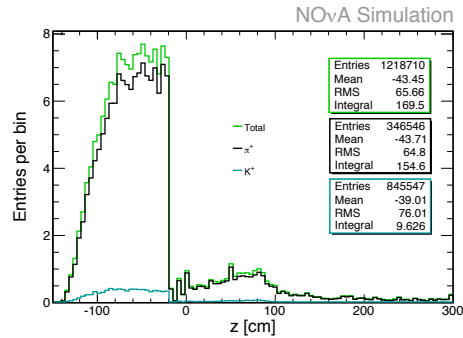
(a) Proton end point is shown in blue. The end of the second and third particle that interact are shown in red and green respectively.



(b) Identities of the particles that come out form the first interaction.



(c) Identities of the particles that come out form the second interaction.



(d) Identities of the particles that come out form the third interaction.

Figure 30: End point of the ancestors that interacted with the material along the beam line for a three interaction case. See text for details.

in the Target (blue). The red distribution is from neutrinos which ancestors interacted at least once outside of the Target.

4.6 PARTICLE TRACKING USING THE ANCESTOR LIST

In this Section a study is reported aiming at a deep understanding of the neutrino flux composition in terms of pion trajectories through the focusing system. Referring to Figure 10 in Section 2.2.1, it is possible to classify the pion trajectories in the following way:

NECK - NECK These are pions that have a low p_T when created, so that they do not go through the magnetic field but instead cross the Horn through the middle aperture (Horn neck) where the field is zero. These pions do not need to be focused.

NECK - HORN 2 These are pions that go through the neck of the first Horn but then are deflected by the second one.

HORN 1 - NECK These are pions that are deflected by Horn 1 and then go through the neck of the second Horn.

UNDER-FOCUSED These are pions that receive insufficient kick from Horn 1, and need Horn 2 to be fully focused.

OVER-FOCUSED These are pions that receive too big a kick from Horn 1 and must be restored by Horn 2.

Since it is not currently possible to access the particle trajectory in the magnetic field, the following method has been developed to understand the pions trajectories. The Ancestor List keep a record of all the particle interactions. Given a pion that will decay in a neutrino, the last interaction before Horn 1 and the first one after Horn 2 are selected. Knowing the momentum at these two points, it is possible to extrapolate the pion position when it enters Horn 1 and exits Horn 2, see Figure 31. Since we are considering the latest interaction before Horn 1, the pion will not undergo other interactions before entering Horn 1. The same applies to Horn 2 so this method gives a very good approximation of the pion positions at the beginning and end of the focusing system.

Two example of pion trajectories retrieved thanks to this method are shown in Figure 32.

4 PREDICTION OF THE NEUTRINO FLUX

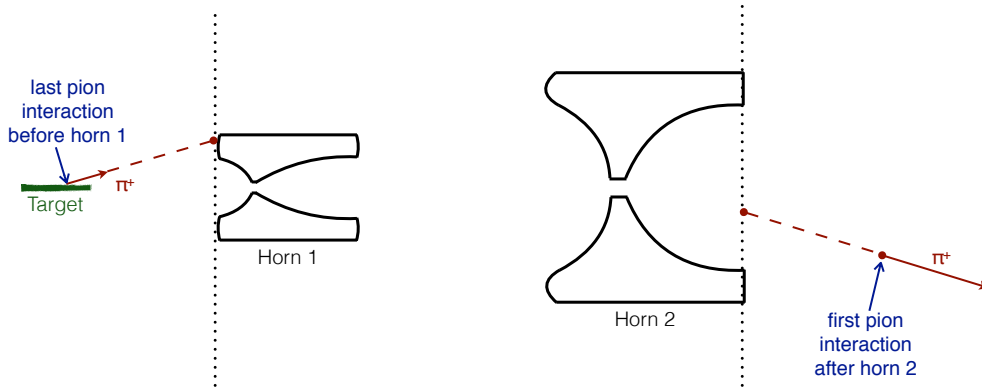


Figure 31: Extrapolation of pion momentum to understand its position at start of Horn 1 and at end of Horn 2.

It should be noted that this is an approximation because, besides energy losses, charged particles undergo scattering by atomic nuclei. In FLUKA, the Molière multiple scattering theory is commonly used to describe the cumulative effect of all scatterings along a charged particle step. This is not recorded in the Ancestor List as an interaction step, because it is an average effect that FLUKA applies to the particle. Figure 33 shows this effect. The estimated position at the Horn 1 (dashed line) could be different from the simulated one (solid arrow). However, the scattering angle average is zero, and the overall effect of the error in the extrapolation is averaged out.

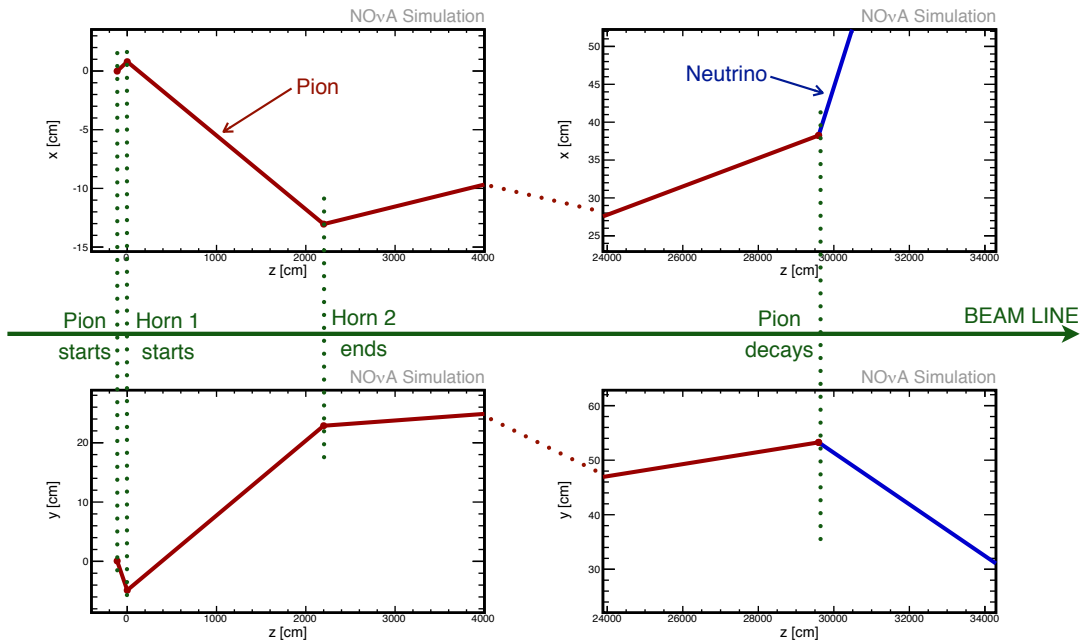
A study on the scattering angle was then performed to check that the angle is indeed small and will only be a negligible perturbation to the estimation of the pion trajectory. The study also provides a simulation cross-check. To give a closer look at this scattering angle, the pions created in the target and re-interacting inside it are selected. This interaction could be an elastic one or a delta-ray source. The Ancestor List allows to easily extract the case and for these two points (production and interaction) to retrieve the particle momenta \mathbf{p}_i and \mathbf{p}_f . Having them, the cosine of the scattering angle θ is simply given by:

$$\cos(\theta) = \frac{\mathbf{p}_i \cdot \mathbf{p}_f}{p_i p_f}$$

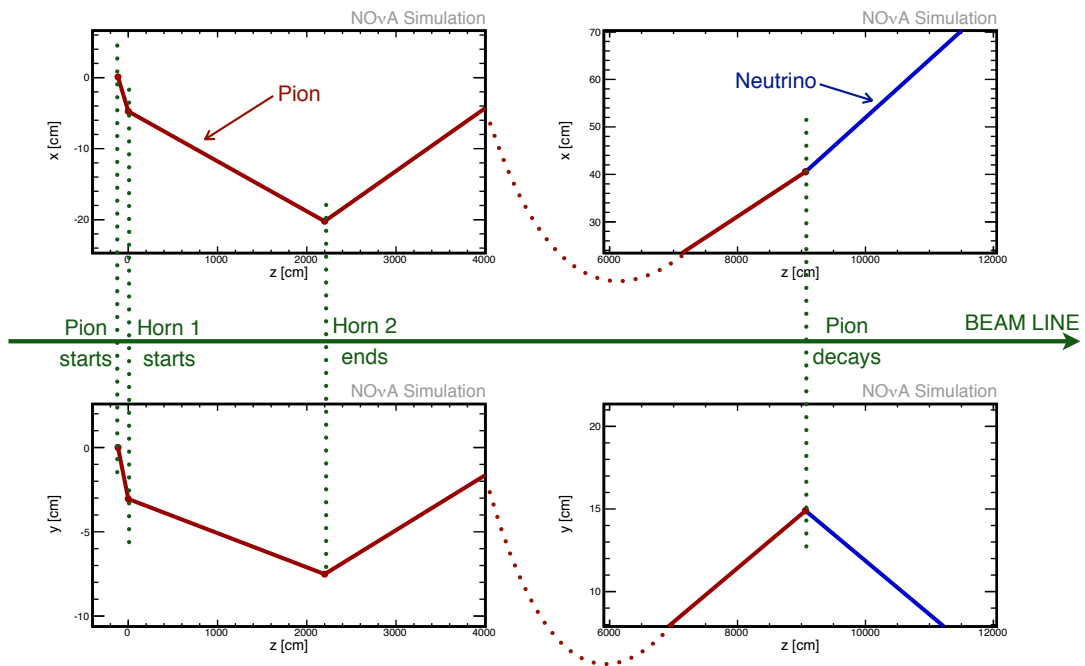
Figure 34a shows the scattering angle simulated by Fluka together with the length of the particle path between these two interactions. The plot in Figure 34b shows the theoretical behavior according to the formula, [12]:

$$\theta = \frac{13.6 \text{ MeV}}{p} \sqrt{\frac{x}{X_0}} \left[1 + 0.038 \ln \left(\frac{x}{X_0} \right) \right]$$

4 PREDICTION OF THE NEUTRINO FLUX



(a) An example of an over-focused pion.



(b) An example of an under-focused pion.

Figure 32: Examples of pion trajectories retrieved from the FLUGG simulation. The red line is the pion trajectory while the blue line is the neutrino one. The neutrino is pointing to the NO ν A ND. The red pion line between the two Horn is not the true trajectory but just connects the points between the start of Horn 1 and the end of Horn 2. See text for details.

4 PREDICTION OF THE NEUTRINO FLUX

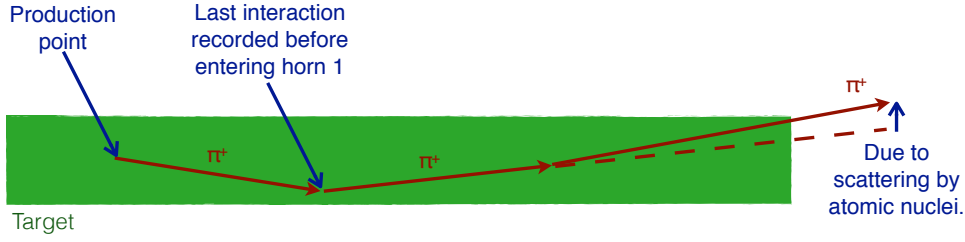


Figure 33: Picture shows the scattering process applied by Fluka to the particle trajectory.

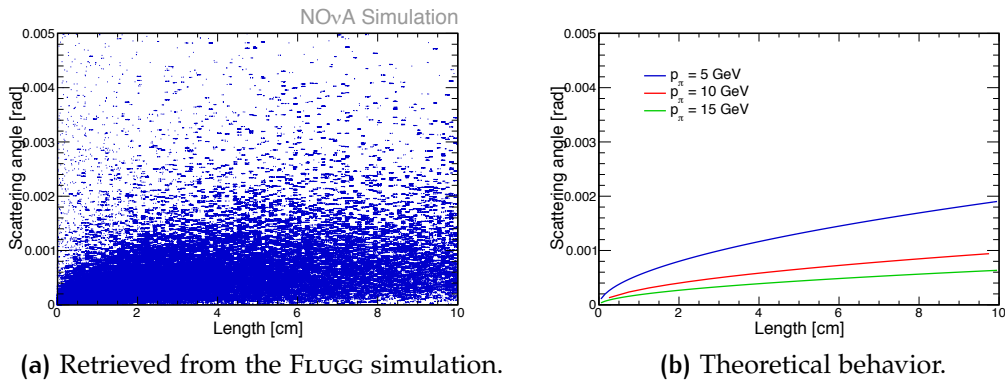


Figure 34: Scattering angle as a function of the distance the pion traveled in the graphite target.

where X_0 is the radiation length that in the graphite is 19.32 cm; x is the particle path and p its momentum. Figure 36a shows the p_T and p_z of π^+ that are direct NOvA ν_μ parents. One can compare this plot with the same that one gets for MINOS neutrino parents in Figure 36b. Selecting 3 typical values of the pion momentum for pion that decays in NOvA neutrinos from Figure 36a, Figure 34b shows the theoretical behavior of the scattering angle as a function of the length the particle travels in the material.

The scattering angle distribution is shown in Figure 35, with a mean value of 0.7 mrad and a rms of 0.6 mrad.

The next two subsections describe the algorithms used to identify all the different pion trajectories.

4 PREDICTION OF THE NEUTRINO FLUX

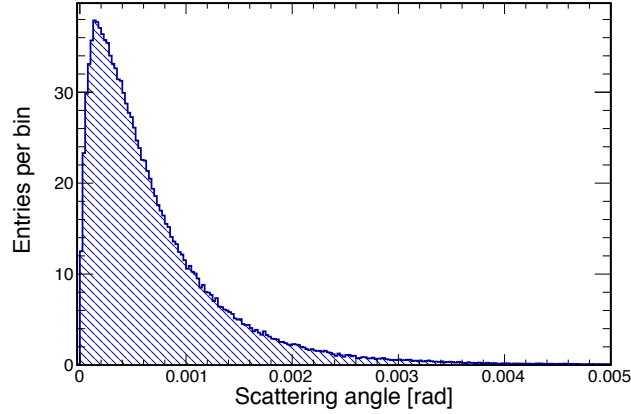
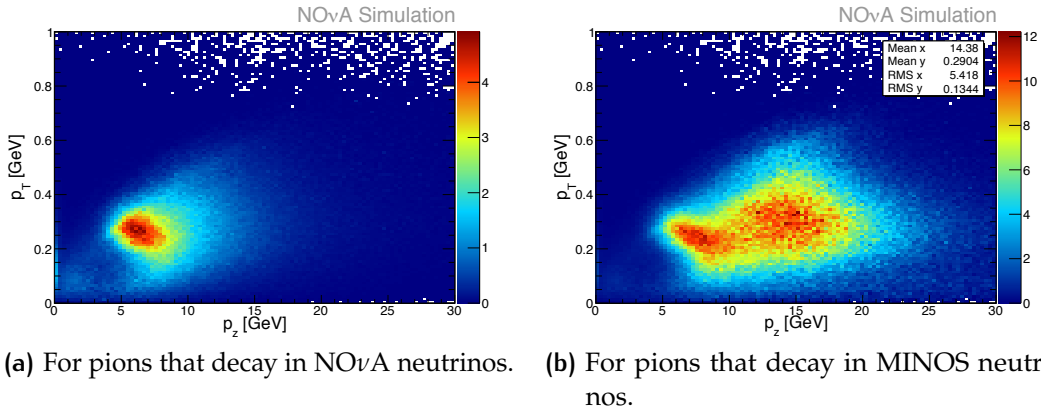


Figure 35: Pion scattering angle in the graphite target.



(a) For pions that decay in NOvA neutrinos. (b) For pions that decay in MINOS neutrinos.

Figure 36: Longitudinal and transverse momentum of π^+ that are direct neutrino parent.

4.6.1 Tagging of particles going through the Horn neck

To select pions passing through the neck of Horn 1, the following strategy has been used. Referring to Figure 37, the pion trajectory is extrapolated to the beginning of Horn 1. At this point, the radial position r_i of the pion is known. The pion trajectory is then extrapolated to the end of the Horn neck to get r_n . Since the Horn dimensions are known (see Table 1 and 2), the pion goes through the Horn neck if $r_i < h_i$ AND $r_n < h_n$, where h_i and h_n are the Horn outer radius and the inner neck radius respectively, see Figure 37.

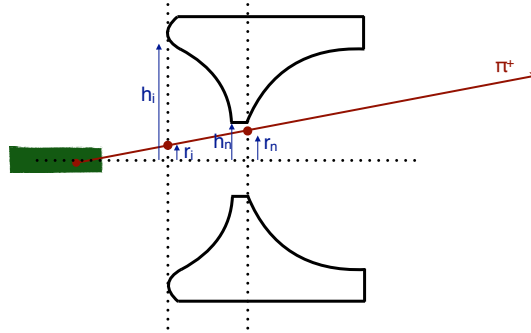


Figure 37: Extrapolation of pion momentum to the neck of Horn1. The goal is to understand if the particle goes through the Horn neck.

The same algorithm (but looking in the opposite direction) also looks at the pions going through the neck of Horn 2.

4.6.2 Tagging of under/over focused pions

In Figure 38 the method applied to identify under/over-focused pions is sketched. Since the pion trajectory was extrapolated to the start of Horn 1 and the end of Horn 2, the position of the red and green points in the Figure is known. In the $x - y$ plane these two points are described by two vectors \mathbf{a} and \mathbf{b} .

The particle is over-focused if it crosses the z axis, while it is under-focused if it does not. So looking at the angle α between \mathbf{a} and \mathbf{b} one can discriminate between these two cases. It's more simple to work with the cosine of this angle:

$$\cos(\alpha) = \frac{\mathbf{a} \cdot \mathbf{b}}{|\mathbf{a}| |\mathbf{b}|}$$

Then:

- $\cos(\alpha) > 0$: the particle is under-focused;
- $\cos(\alpha) < 0$: the particle is over-focused;

Due to the cylindrical symmetry of the focusing system, one would expect α to be either 0 (the pion is under-focused) or π (the pion is over-focused). But scattering effects with the Horn material and the air let α assume values between 0 and π , as it's possible to see in Figure 39, where the α distribution is shown. This distribution has been retrieved from a simulation with 500k POT.

4 PREDICTION OF THE NEUTRINO FLUX

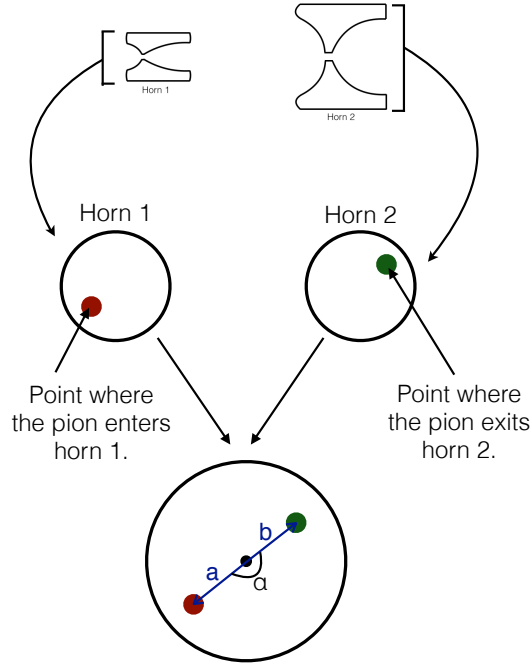


Figure 38: In this Figure is shown the method used to understand if the pion is under or over-focused. Blue vectors \mathbf{a} and \mathbf{b} lie in the $x - y$ plane. If they point in opposite directions the pion is over-focused, otherwise is under-focused.

4.6.3 Decomposition of the neutrino spectrum

Figures 40 and 41 show the predicted neutrino spectrum from the two-Horn system of the NuMI beam line for MINOS and NO ν A respectively. They also show the components of this spectrum corresponding to the different pion trajectories discussed previously. As the angle of the neutrino parent decreases, one expects its momentum $p \sim \langle p_T \rangle / \theta$ to increase. The pions focused by only Horn 1 give softer neutrinos than those focused only by Horn 2. Notably, that the peak of the neutrino energy spectrum comes from particles which pass through the focusing system, while the "high energy tail" comes from particles which pass through the field-free apertures of the Horns.

Figure 42 shows the same spectrum decomposition for NO ν A but with the Horn Currents decreased to 160 kA. Table 3 shows the number of ν_μ events at the NO ν A ND from π^+ having different trajectories through the focusing system. The number of events (i.e the integral of the distributions

4 PREDICTION OF THE NEUTRINO FLUX

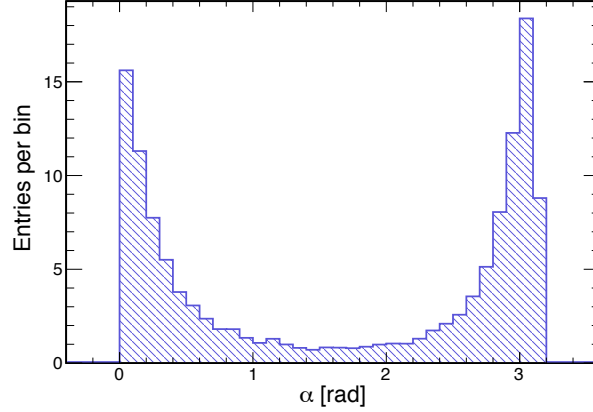


Figure 39: Distribution of the α angle. See text for details. We expect α to be either 0 (the pion is under-focused) or π (the pion is over-focused). Scattering effects with the Horn material and the air let α assume values between 0 and π .

in Figure 41 and 42) is shown for the nominal value of the Horn Current (200 kA) and for the Horn Current reduced to 160 kA.

Comparing the Figures of the $\text{NO}\nu\text{A}$ and the MINOS spectra, it is immediately noticed that while the MINOS spectrum gets a major contribution by under-focused pions, this is not true for the $\text{NO}\nu\text{A}$ spectrum. As shown in Figure 40, the under-focused pions generate higher energy neutrinos compared with the over-focused. These high energy pion are not likely to decay in neutrinos at the $\text{NO}\nu\text{A}$ off-axis angle. This can be shown with an explicit calculation. Going back to eqn. 41, that express the probability that a pion decays in a neutrino directed toward the center of the detector, one can derive the angular distribution of neutrinos in the laboratory frame. For simplicity, let us re-write eqn. 41:

$$w = \frac{1}{4\pi} M^2 \Delta\Omega, \quad M = \frac{1}{\gamma(1 - \beta \cos \theta)}.$$

where θ is the angle between the neutrino and the parent direction. If we assume that the pion is perfectly focused (i.e. as a zero transverse momentum), then θ is the off-axis angle. The angular distribution of neutrinos in the laboratory frame is then

$$\frac{dP}{d\Omega} = \frac{1}{4\pi} M^2 = \frac{1}{4\pi} \left(\frac{1}{\gamma(1 - \beta \cos \theta)} \right)^2$$

4 PREDICTION OF THE NEUTRINO FLUX

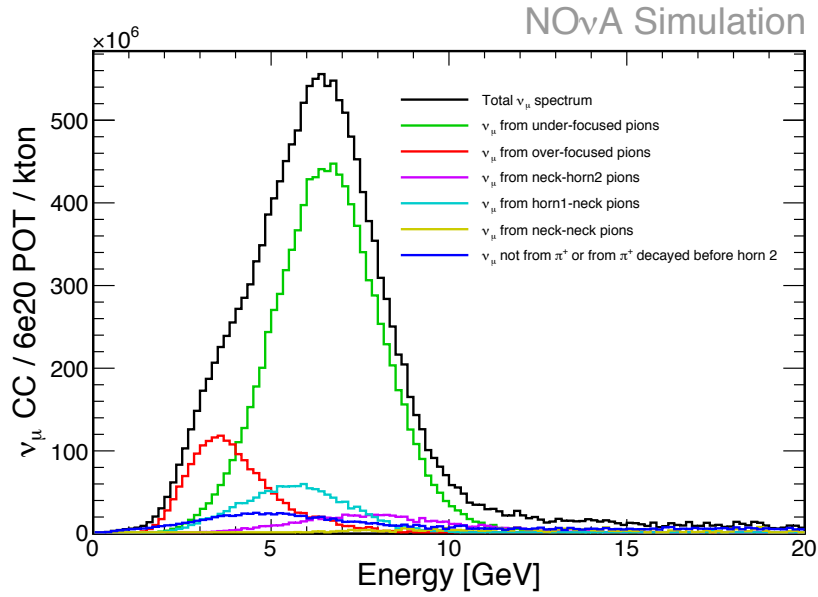


Figure 40: Neutrino spectrum at the MINOS ND (on-axis) from the two-Horn beam at the NuMI facility. The components of the spectrum correspond to the different possible pion trajectories of Figure 10.

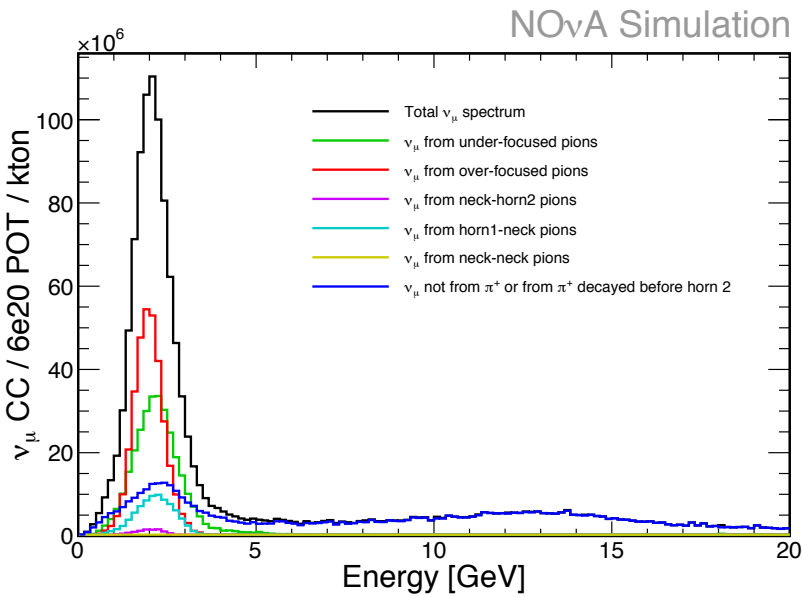


Figure 41: Neutrino spectrum at the NOvA ND (off-axis) from the two-Horn beam at the NuMI facility. The components of the spectrum correspond to the different possible pion trajectories of Figure 10.

4 PREDICTION OF THE NEUTRINO FLUX

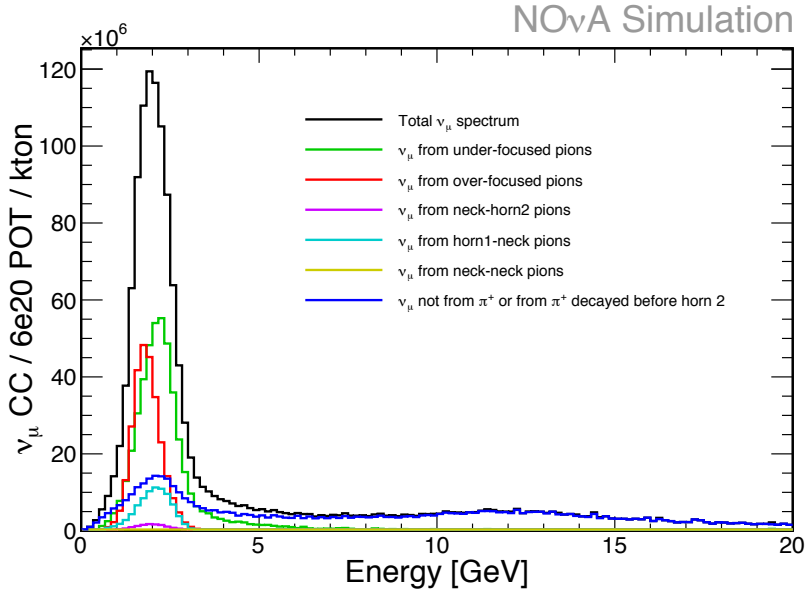


Figure 42: Neutrino spectrum at the NOvA ND (off-axis) with the Horn Current set to 160 kA. The components of the spectrum correspond to the different possible pion trajectories of Figure 10. The over-focused and under-focused components are swept w.r.t. the nominal value of the Horn Current, 200 kA, see Figure 41.

Table 3: Number of events at the NOvA ND from ν_μ that come from π^+ having different trajectories through the focusing system. See text for details. *Total ν_μ* means the number of ν_μ events independently of the pion trajectory. *Others* means ν_μ events from other parents rather than π^+ , or from π^+ that decayed before the end of Horn 2. The events are shown for two values of the Horn Current: 200 and 160 kA.

	200 kA		160 kA	
	Events [$\times 10^6$]	Ratio w.r.t. total ν_μ (%)	Events [$\times 10^6$]	Ratio w.r.t. total ν_μ (%)
Total ν_μ	60.9	100	59.8	100
Under-focused	21.0	34.5	26.4	44.1
Over-focused	24.4	40.1	17.7	29.6
Neck-neck	0.06	0.1	0.1	0.2
Horn1-neck	5.7	9.4	5.2	8.7
Neck-Horn2	0.9	1.4	0.8	1.3
Others	9.8	16.0	9.5	15.9

This expression can be simplified if one considers small off-axis angles: $\theta \ll 1$, so that $(1 - \beta \cos \theta) = (1 - \beta) + \beta(1 - \cos \theta) = 1/2(1 - \beta^2) + \theta^2/2$. From this:

$$M = \frac{2\gamma}{1 + \gamma^2\theta^2}$$

and the neutrino angular distribution is

$$\frac{dP}{d\Omega} = \frac{1}{4\pi} \left(\frac{2\gamma}{1 + \gamma^2\theta^2} \right)^2$$

Finally, the flux of neutrinos at a given decay angle θ with respect to the pion direction is

$$\phi_\nu(\theta) = \frac{A}{4\pi z^2} \left(\frac{2\gamma}{1 + \gamma^2\theta^2} \right)^2$$

where A is the size of the detector, z is its distance from the pion decay point, and γ is the pion boost factor. Figure 43 shows the suppression $\phi_\nu(\theta)/\phi_\nu(0)$ of the off-axis flux with respect to the on-axis flux for $\theta = 14.6$ and 130 mrad. As the pion energy increases, the suppression is bigger such that the large majority of the high energy pions do not decay in NO ν A neutrinos.

Looking back at Figure 36b, that shows the transverse and longitudinal momentum of π^+ that will decay in MINOS ν_μ , two clusters are visible. They correspond to the over-focused (the left one) and under-focused (the right one) pions. The energy of these pions is shown in Figure 44 separately for under and over-focused. These two distributions correspond to the two clusters in Figure 36b. Just looking at the mean of these distributions one can see from Figure 43 that under-focused pions are more suppressed than over-focused.

4.7 CROSSING POINT ALONG THE BEAM LINE FOR OVER-FOCUSED PIONS

Let us refer only to over-focused pions since they contribute to a great part of the NO ν A neutrino spectrum (see Fig. 41). These pions are too much focused by Horn 1 as they cross the z axis in some point and then are restored by Horn 2, that completes the focusing.

One could think to put a second target between Horn 1 and Horn 2 to make use of the protons that have not interacted in the NuMI target ($\sim 1/3$ of the proton beam) to increase the neutrino yield. It is then interesting to understand

4 PREDICTION OF THE NEUTRINO FLUX

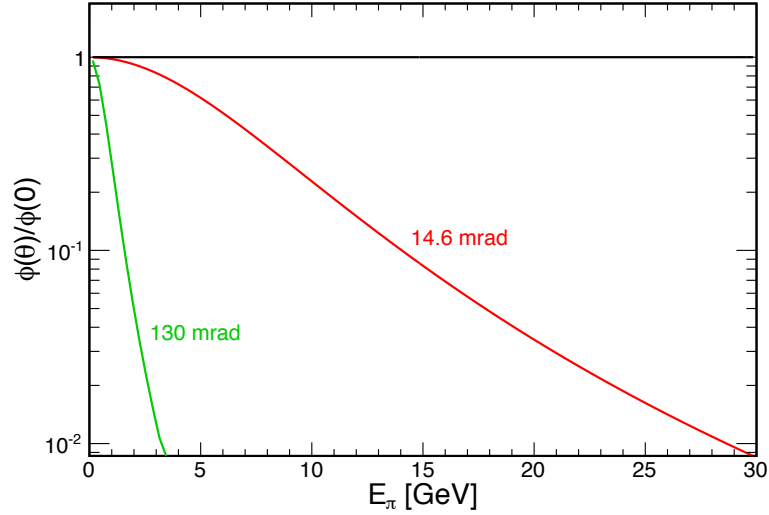


Figure 43: Suppression of the off-axis neutrino flux with respect to the on-axis flux for two off-axis angles: 14.6 and 130 mrad.

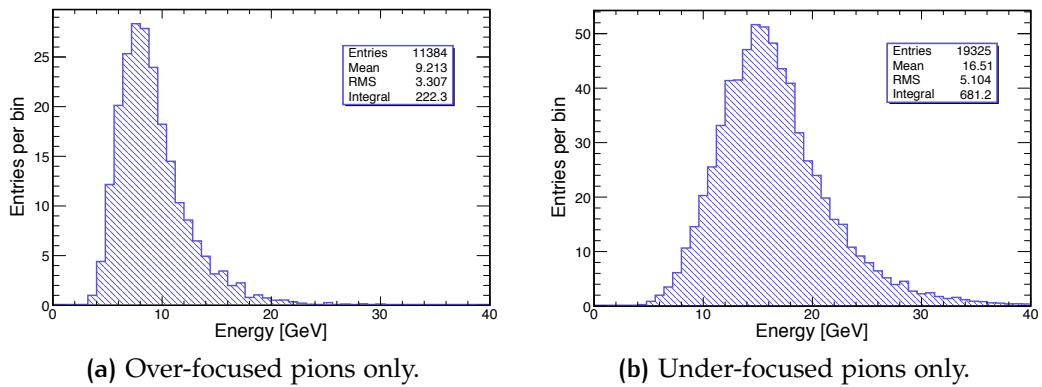


Figure 44: Energy of the π^+ that will decay in ν_μ directed to the MINOS ND. Under-focused pions are more energetic than over-focused.

where the over-focused pions cross the z axis to find a good spot to place this second target in such a way that it will not absorb many of the pions that were created by the first target.

Figure 32a shows the trajectory of a pion retrieved from one simulation. The red line that connects the points where the pion enters Horn 1 and exits Horn 2 is not the real trajectory of the pion, but it just connects the pion position at the start of Horn 1 and at the end of Horn 2. It can not be used to extract the position where the pion crosses the beam line, but this can be overcome using again the Ancestor List. Selecting only the pions that have an interaction in the region between the two Horns (usually a delta ray interaction with the air) and knowing the pion momentum at that point thanks to the Ancestor List, one can extrapolate the pion trajectory between the Horns as a straight line, described in the x and y views by:

$$x(z) = m_x z + q_x \quad y(z) = m_y z + q_y$$

If there was only the effect of the magnetic field, one expects to find a value of z where both x and y are zero, but scattering processes are present that will make the particle deviate from the expected trajectory in the absence of materials. For this reason, one should look at the z position where the distance (or the square one) from the z axis $r^2(z) = x^2(z) + y^2(z)$ is minimum:

$$\frac{dr^2}{dz} = 0 \quad \implies \quad z = -\frac{m_x q_x + m_y q_y}{m_x^2 + m_y^2}$$

Using this strategy, one can retrieve the closest approach positions of the pion to the z axis. The distribution of such points is shown in Figure 45.

4.8 PION ANGLE W.R.T. THE BEAM LINE AFTER THE FOCUSING

Once we know the π^+ trajectory along the beam line it is straightforward to look at the pion angle w.r.t. to the beam line after the focusing. The magnetic Horns are not 100% efficient and that angle is not exactly zero as it would be for a perfectly focused pion. It is also useful to select only those pions that will decay in neutrinos directed toward the NO ν A ND and FD. The distributions of this angle is shown in Figure 46. Plots on the left part show the angle for π^+ that will decay in neutrinos forced to the center of the ND. Right plots is the

4 PREDICTION OF THE NEUTRINO FLUX

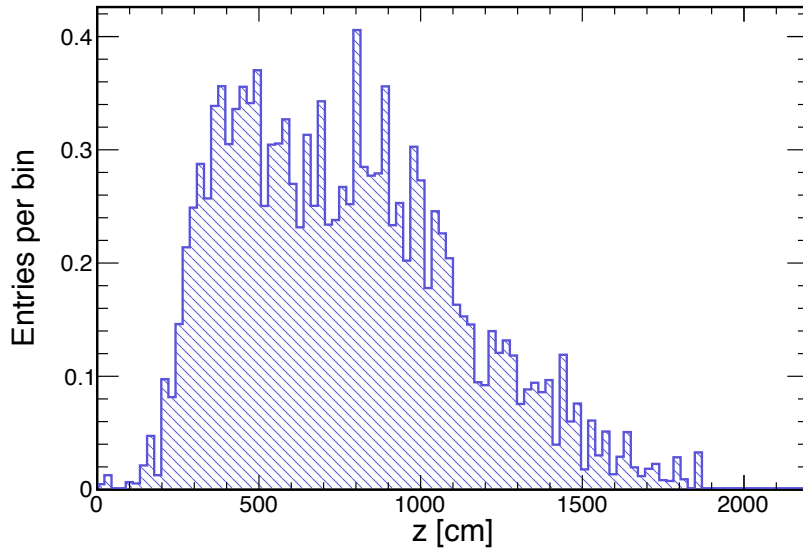


Figure 45: Position along the z axis where the over-focused pions travel more closed to the z axis. Horn 1 extends from 0 to 300 cm and Horn 2 from 1900 to 2200 cm.

same but for the FD. The angle is shown in the $x - z$ plane (θ_x), in the $y - z$ plane (θ_y) and in space (θ_{space}).

Common to both the ND and FD is that the distribution spread is bigger for over-focused pions than for under-focused. The ND distributions also have a bigger width w.r.t. the FD. In fact, since the ND is closer to the beam production target:

- it sees a neutrino line source since decays do not all happen in the same point;
- it is more sensible to neutrino (and then pion) angular spread.

But since we are only considering a 1 meter radius circle at the center of the detector, the second effect is not visible in the distributions in Figure 46.

4 PREDICTION OF THE NEUTRINO FLUX

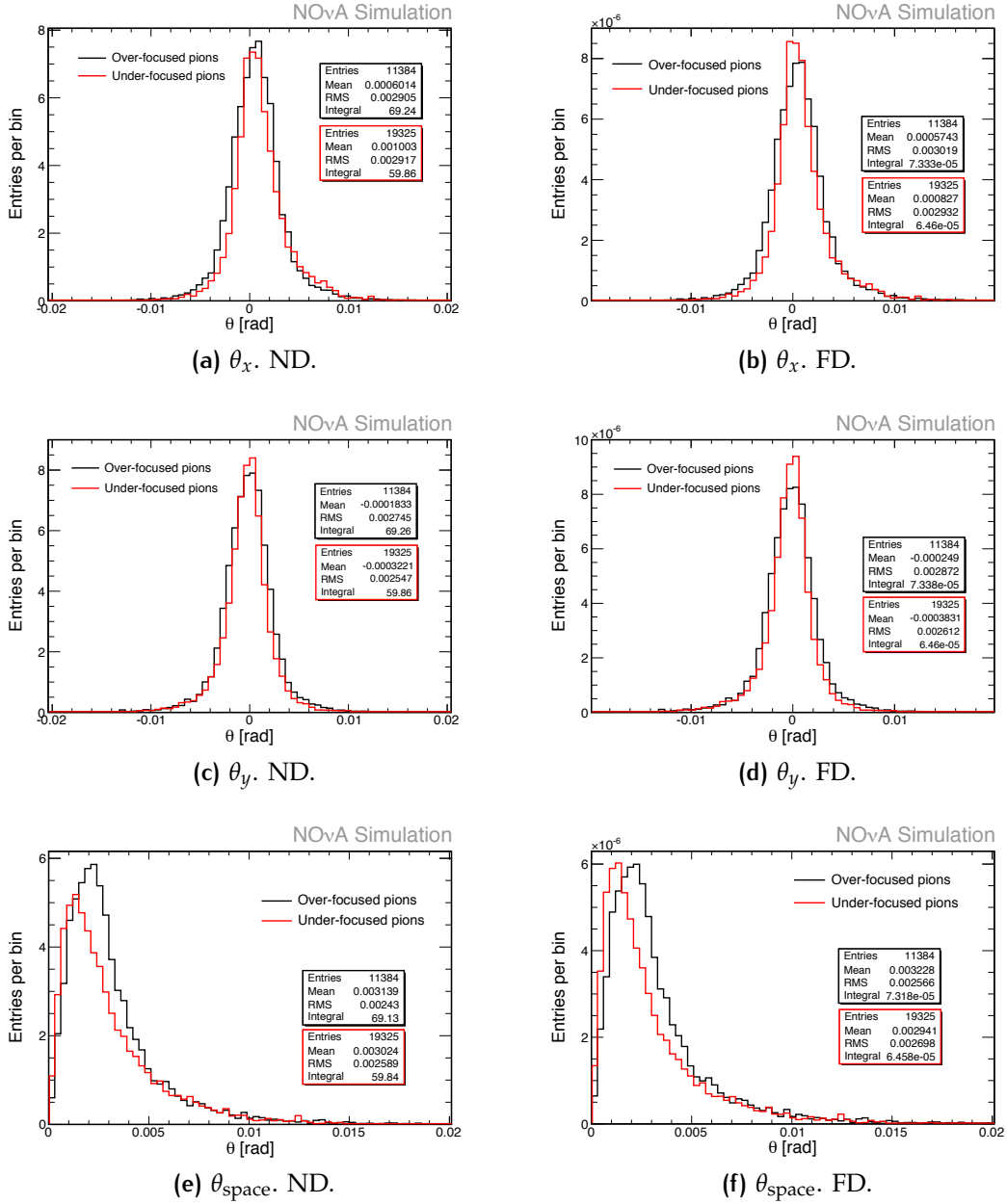


Figure 46: π^+ angle with respect to the beam line as the pion exits Horn 2, i.e. after the focusing. Plots on the left show such angle for π^+ that will decay in neutrinos forced to the center of the ND. Right plots is the same but for the FD. The angle is shown in the $x - z$ plane (θ_x), in the $y - z$ plane (θ_y) and in space (θ_{space}).

5 | HORN CURRENT STUDIES

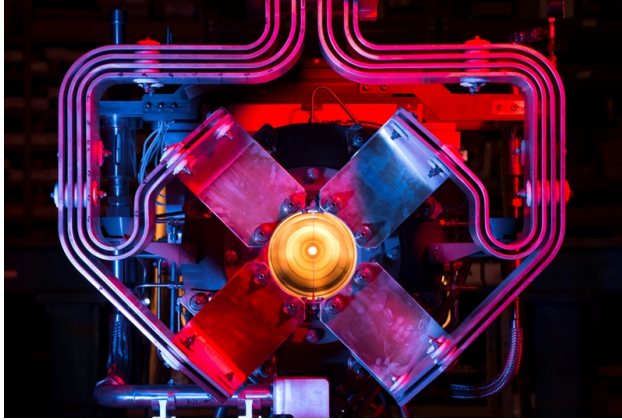


Figure 47: The NuMI magnetic Horn and the striplines.

A study on the Horn Current (HC) was performed as part of this thesis work. As described in Section 2.2, the magnetic Horns are devices that allow to focus one sign charged particles and de-focus particle with the opposite sign.

Using both the FLUGG and G4NuMI simulations, the HC was decreased from the nominal value to understand how the neutrino spectrum changes with this variation. This study is shown in the following Sections. To check

the Monte Carlo (MC) prediction, data were taken during June 2015, changing the HC. The data analysis is presented in this Chapter, together with a comparison between data and MC.

5.1 MOTIVATIONS

The NO ν A Beam Group has been looking at the NuMI beam using both G4NuMI and FLUGG simulations. The goal is to vary all the beam parameters systematically to make sure NO ν A is getting the optimum neutrino yield per POT. These beam simulations yield similar but not identical results and further studies are required to understand the underline difference between these two.

One very important feature is that sometimes they show a very different behavior for the NO ν A off-axis beam than seen for the on-axis beam. The behavior at different HC is such an example. A possible comparison between data and MC is to look at the variation of the number of events as a function of the HC, [75]. Although there are other variable beam parameters suitable to

check the accuracy of the simulation and the on/off-axis behavior, the HC is really the only parameter one can change while taking data. Five shifts of beam (8 hour each) were then proposed to check the MC expectations shown in Figure 48a, [74]. This Figure shows the simulated neutrino energy spectrum for several values of the HC at the NO ν A ND. The HC have been turned down from 200 kA (nominal value) to 0 kA (no magnetic field at all). First, it is possible to notice the impressive effect of the magnetic focusing: considering the flux at 200 kA as the "standard flux", if one goes to 0 kA loses 91.94% of neutrino events off-axis.

Figure 48b shows the simulated neutrino energy spectrum seen by the MINOS ND. Clearly, an on-axis detector immediately loses events when the current is lower. Conversely, an off-axis detector actually gains some events at slightly lower current, and keeps the original yield if the currents are decreased to 160 kA, see Figure 48a. According to the simulation, an off-axis experiment is characterized by the stability in number of events as the HC is turned down.

All the simulations have been run with an exposure of 5×10^6 POT.

Figure 49a shows the number of events as a function of the HC predicted by FLUGG for both the NO ν A and the MINOS ND. Figure 49b shows the same number of events at the NO ν A ND predicted by both FLUGG and G4NuMI. Both programs show that an off-axis detector will get the same neutrino yield if the HC are decreased to 160 kA.

The data taken with the NO ν A ND during the actual runs with different current values were expected to:

- verify the approximately flat behavior in the range 160 – 200 kA;
- verify the yield drop at 140.

If data confirm the behavior predicted by MC, the HC could be decreased in future running and this will be helpful because the Horn heats up due to the pulsed current and radiation. Although during running the inner conductor is being cooled with nozzles that spray water on it, Horn 1 will be near the edge of its design for heating of the inner conductor at 700 kW. The NuMI Horns are now working with a current of 200 kA, that is the maximum current they were designed to sustain.

If the HC can be decreased in future running, this will improve the Horn lifetime and would allow putting more target material closer to Horn 1. Having more fins closer to Horn 1 will increase the NO ν A neutrino yield, as was shown in previous studies, [5]. At the moment this is not possible because it will increase the Horn heating from secondary particles. However, if the HCs are

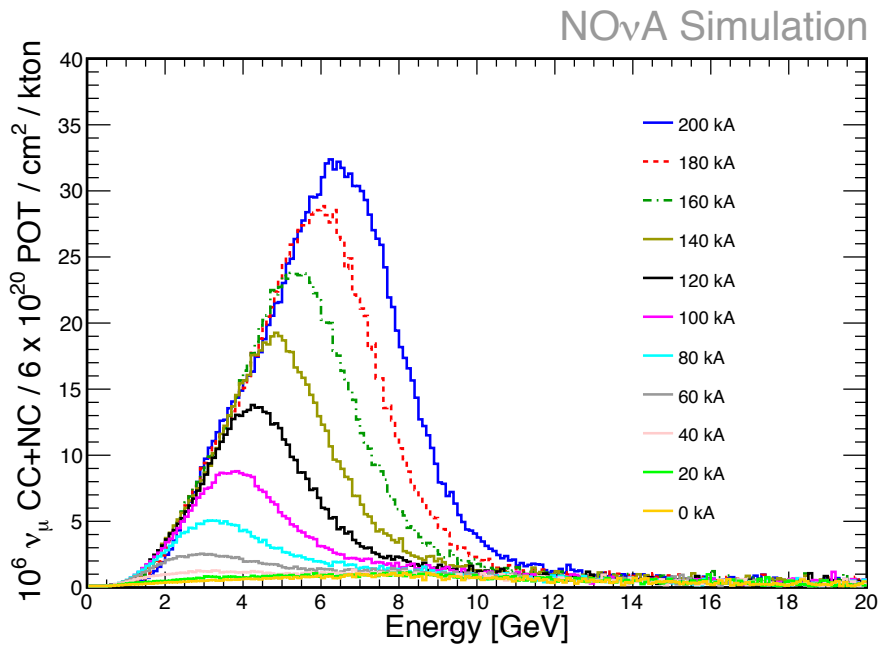
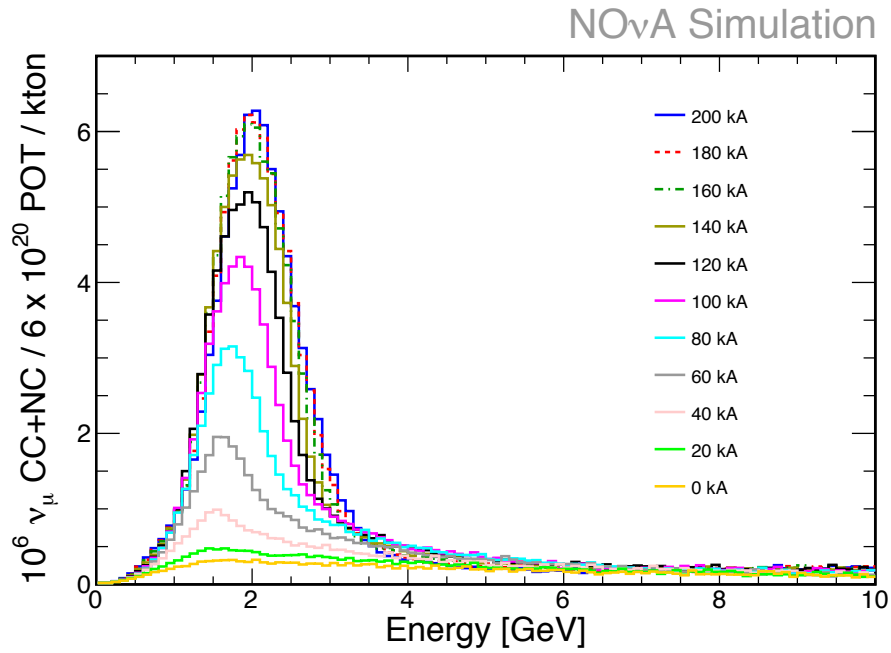


Figure 48: Neutrino energy spectrum for the different values of the HC. From the FLUGG simulator.

5 HORN CURRENT STUDIES

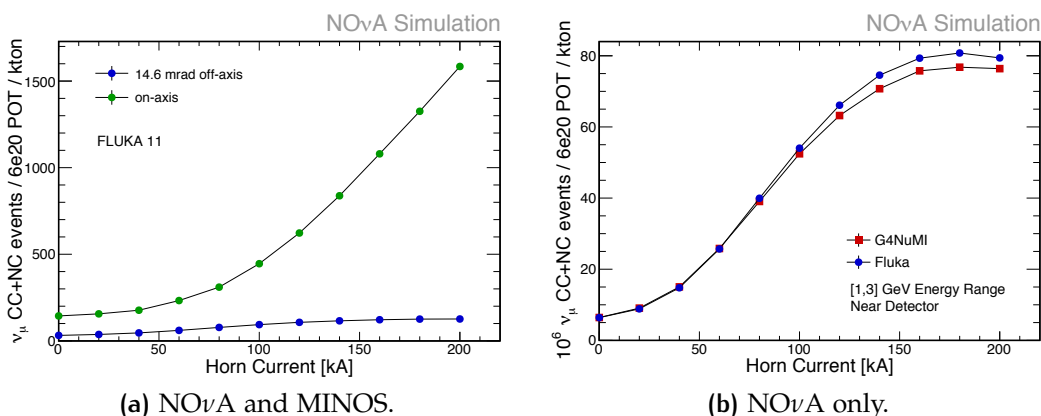


Figure 49: Simulated number of events as a function of the HC. Left plot show how the neutrino yield changes for both NO ν A (blue) and MINOS (green) retrieved from the FLUGG simulator (G4NuMI gives similar results). MINOS immediately loses events as the HC are turned down. Right plot shows the neutrino yield for NO ν A only simulated by FLUGG and G4NuMI. Both simulators show that NO ν A will approximately see the same number of events if the current is pulled down to 160 kA. Otherwise the neutrino yield will decrease if the current is less than 160 kA.

turned down, the Joule heating will go down and allow more fins to be put closer to Horn 1.

Lower HC will also put much less stress on the stripline. Striplines are the conductors that bring electric current to the Horn surface. A picture of the striplines is shown in Figure 47.

The previous Chapter showed a study on the pion trajectory along the beam line. Figures 41 and 40 show the neutrino spectrum decomposition in terms of over and under-focused neutrinos at the NO ν A ND for 200 and 160 kA respectively. As it is possible to see, the over/under-focused ratio changes when the HC is lowered. In particular, there are less over-focused pions at 160 than at 200 kA. Since over-focused pions cross the beam line axis, running at 160 kA will reduce the number of pions that cross the beam axis and so it would allow to place a second target between the horns. The idea of putting a second target is to capture the 1/3 of the protons that do not interact with the first target. If a second target is placed with the HC at 200 kA, however it will reduce the neutrino flux since it will kill great part of the over-focused pions, see [5].

5.2 DATA TAKING

Data have been taken in one week starting from June the 8th to June the 12th. I was assigned to take responsibility of the beam line tuning during the period. Table 4 shows the date and time when data were taken.

The HC values are retrieved from the Intensity Frontier database (IFDB) and are show in blue in Figure 50a as a function of time for the run at 160 kA. Four calibrated devices (NSLINA, NSLINB, NSLINC, and NSLIND) are used to calculate the total HC. Taking into account their calibration ([42], [46]), the HC is calculated as:

$$I_{\text{horn}} = (\text{NSLINA} - 0.01)/0.9951 + (\text{NSLINB} + 0.14)/0.9957 \\ (\text{NSLINC} + 0.05)/0.9965 + (\text{NSLIND} + 0.07)/0.9945$$

Accounting for these calibrations, the final values of the HC as a function of time are shown in red in the same Figure. Figure 50b shows the HC distribution for the run at 160 kA.

Table 4: Days and time when the Special Runs were performed.

HC [kA]	Day	Start Time	End Time	Notes
160	06/08/2015	9:41	17:51	
140	06/09/2015	14:10	22:00	From 17:16 to 18:32 beam power was 260 kW (instead of 240) and intensity was $24e12$ (instead of $32e12$).
190	06/10/2015	14:36	22:00	No beam from 17:56 to 19:10.
180	06/11/2015	15:07	18:28	From 14:00 to 15:00 ND didn't work.
180	06/11/2015	18:39	18:54	A small run again at 180 kA.
170	06/11/2015	18:56	22:03	
180	06/12/2015	13:59	17:55	
170	06/12/2015	17:57	22:02	

5 HORN CURRENT STUDIES

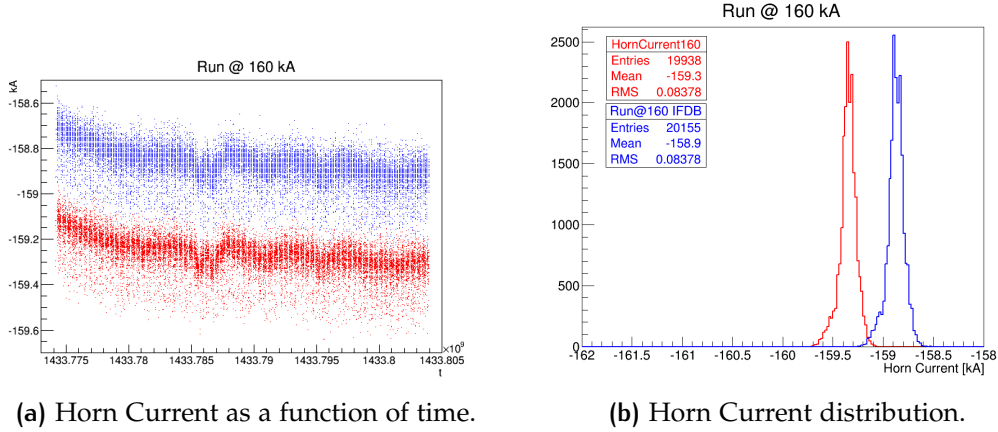


Figure 50: Horn Current as a function of time and Horn Current distribution for the Special Run at 160 kA. Blue plots are retrieved from the Intensity Frontier database (IFDB). Red plots are the final distributions where the calibration correction was applied (see text for details).

5.3 EVENT RECONSTRUCTION

As written in Section 3.4, the NO ν A ND is made of cells of extruded, highly reflective plastic PVC filled with liquid scintillator. When a neutrino strikes an atom in the liquid scintillator, it releases a burst of charged particles (see the event display in Figure 51). As these particles come to rest in the detector, their energy is collected using wavelength-shifting fibers connected to photo-detectors. Using the pattern of light seen by the photo-detectors, one can determine what kind of neutrino caused the interaction and what its energy was. There are three ways a neutrino can interact with a nucleon N in the NO ν A Detector via a CC interaction:

QUASI-ELASTIC INTERACTION (QE) The neutrino interacts with a neutron n or a proton p in the nucleon:

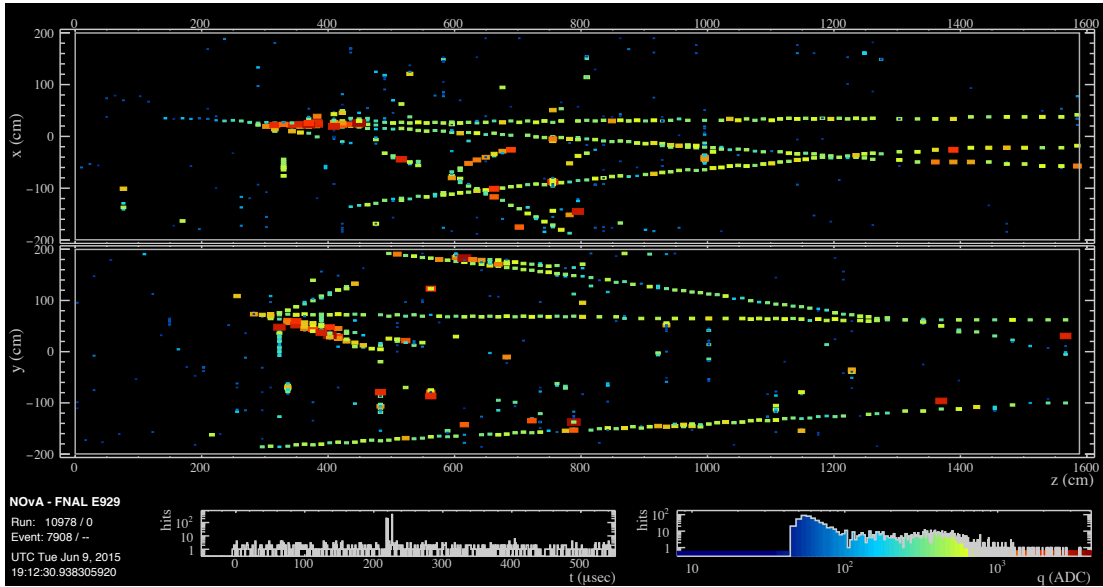
$$\nu_{\mu} + n \rightarrow \mu^{-} + p \quad \text{or} \quad \nu_{\mu} + p \rightarrow \mu^{+} + n$$

RESONANCE EXCITATION (RES) The neutrino interacts with the nucleon via:

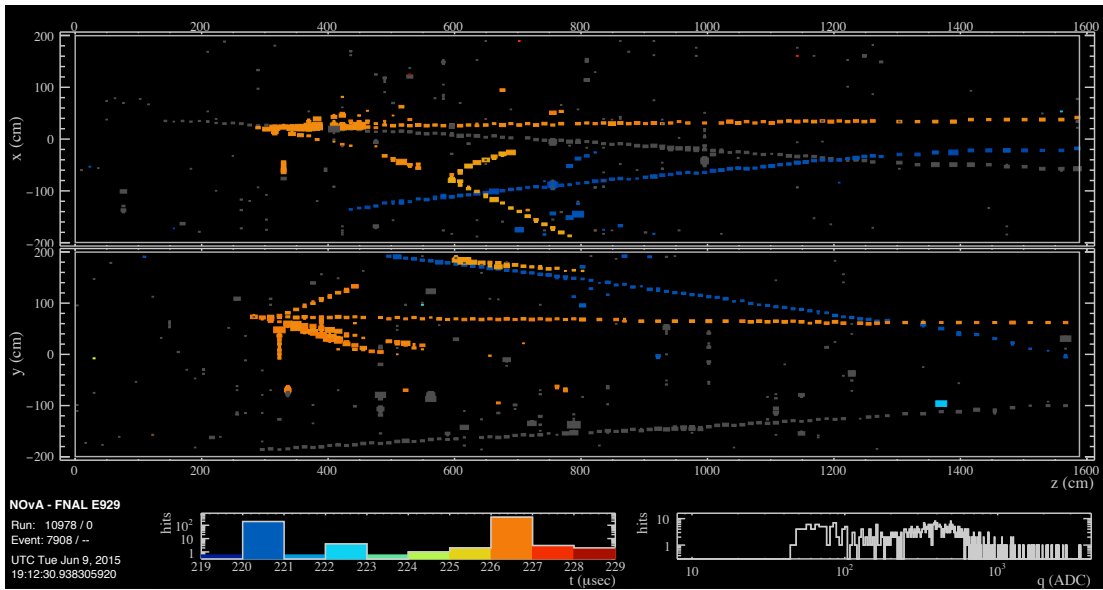
$$\nu_{\mu} + N \rightarrow \mu + \Delta N^{*} \rightarrow \mu + \pi N'$$

where Δ and N^{*} correspond to excited states, decaying with π production.

5 HORN CURRENT STUDIES



(a) Usually, in the NOvA ND there are more than one interaction per spill.



(b) A 10 μs time window allow to select the tracks in time.

Figure 51: The NOvA event display. Beam comes from left to right.

(DEEP) INELASTIC INTERACTION (DIP) The neutrino interacts with the nucleon destroying it:

$$\nu_\mu + N \rightarrow \mu + X$$

where X are the debris from the destroyed nucleon.

A spill of approximately 32×10^{12} protons is delivered every 1.3 seconds on the NuMI target. At each spill, a trigger window of $10 \mu\text{s}$ is opened and during that time the two NO ν A Detectors record data. This "NuMI trigger" is very useful for the FD. Since the FD is on surface, cosmic events are a large background and the NuMI trigger allows to discard all the cosmic events outside the NuMI trigger window.

Event reconstruction [57] begins with grouping hits correlated in time and space into *slices*. A slice is a cluster of hits associated/correlated between themselves. The intention is that each slice corresponds to one neutrino interaction. The next steps are to reconstruct 3D tracks and select the most muon-like track.

Track reconstruction is performed using a track finding algorithm based on a Kalman filter. The main goal is to reconstruct the true muon trajectory in a ν_μ CC event.

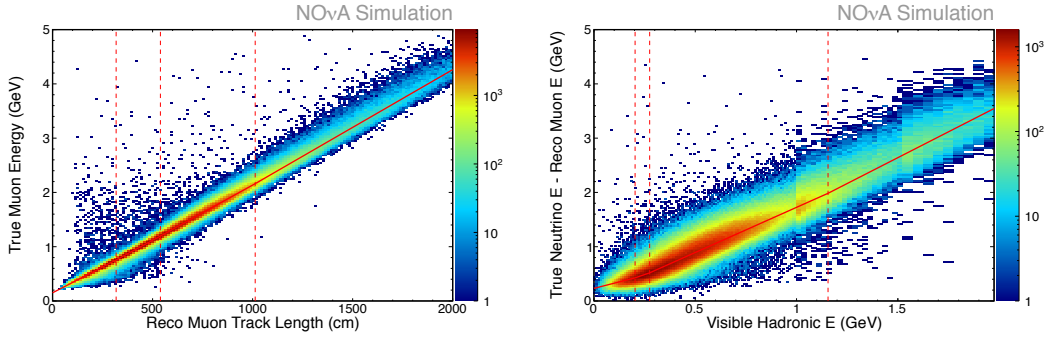
5.3.1 Energy Estimation

The reconstructed energy of ν_μ CC events is based on the reconstructed muon track length and the sum of all energy deposits in cell hits not associated with the muon track. Specifically,

$$E_{\nu_\mu} = E_\mu^{\text{range}} + E_{\text{calo}}$$

where E_μ^{range} is the energy of the muon based on its reconstructed pathlength through the detector, and E_{calo} is defined as the summed energy (in GeV) of all hits in the slice which are not on the track tagged as a muon (the track with the highest ReMId value, see Section 5.4) as well as the summed energy of the hadronic contamination on the muon track in the vertex region. Both E_μ^{range} and E_{calo} are calibrated in this analysis from MC as described in [49].

E_μ^{range} is reconstructed using a linear four-spline fit from FD simulation that relates reconstructed track length (in cm) to true muon energy (in GeV), see Figure 52a. For the ND, if the muon enters the muon catcher, a linear fit is used to relate reconstructed track length in the muon catcher (in cm) to true muon energy when it enters the muon catcher (in GeV). This is then used to create an effective track length in active detector and is added to the reconstructed track



- (a) This plot shows the fit of reconstructed muon track length (cm) to true muon energy (GeV) for the Numu analysis.
- (b) This plot shows the fit of visible energy excluding the muon track (GeV) to true neutrino energy minus reconstructed muon energy (GeV). Note the x-axis has variable binning.

Figure 52: Energy fits. See single Figure captions for details. The fit used is a four-spline fit, with 3 junction locations, 4 slopes, and one offset value as free parameters. Note the z-axis is on a logarithmic scale. The fit is displayed as a red line. Dotted lines indicate spline junctions. [49].

length in the active part of the detector. Finally, the FD fit is used to return the total reconstructed muon energy (in GeV).

The visible hadronic energy (GeV) is the calorimetric energy E_{calo} that is not associated with the muon energy, see Figure 52b.

As described in [57], the hadronic sector needs a correction to correctly estimate the hadronic energy. Since the calibration of the hadronic energy is done using the MC, a correction applied to the MC hadron interaction modeling will result in a correction to the calibration procedure. For this reason, an empirical correction is applied to the data, shifting the reconstructed hadronic energy such that the data matches the MC.

At the end, the hadronic energy has been scaled up by 21%. To be conservative, this 21% has been considered has the systematic uncertainty on such energy (it results in a 6% uncertainty on the neutrino energy). NO ν A is continuing to look for an underlying reason for this energy shift.

5.4 EVENT SELECTION

The signal for the ν_μ analysis consists of muon neutrinos that interact through a CC process.

The Event Selection needed to select ν_μ CC events only is done following the official NO ν A procedure [57]. Observation of the muon in these events provides a handle for detecting ν_μ CC events. The majority of the background comes from neutral current (NC) interactions where one of the particles produced is a penetrating π^\pm . In these events, the π^\pm has features similar to muons in ν_μ CC events. The easiest background neutrino event to reject comes from ν_e CC interactions. These result in a final state electron which typically leaves a electromagnetic shower.

The ν_μ CC selection is done by the *ReMId* (Reconstructed Muon Identification, [65]) algorithm. ReMId assumes that each track is a muon track and then builds up a PID (particle identification) discriminating variable.

ReMId uses four observables to classify the ν_μ CC muon likeness of the a reconstructed track:

- *dE/dx log-likelihood (LL)*. Muons in the detectors lose a regular dE/dx as a function of energy following the Bethe-Bloch equation. Charged pions, on the other hand, lose energy not only through Bethe-Bloch processes, but also through hadronic scattering. In the NO ν A detectors, the interaction length for a charged pion is ~ 80 cm. Using the dE/dx shape information makes it possible to distinguish particles from each other.
- *Scattering LL*. The scattering LL variable looks at the scatter of the reconstructed track as a function of the distance from the end of the track. The NO ν A detectors are not magnetized so any curvature in reconstructed tracks is due to scattering. Muons passing through the detector get most of their curvature from small angle multiple scattering with occasional hard scatters due to Coulomb scattering. Charged pions undergo the same Coulomb scattering, but have additional scattering from hadronic interactions.
- *Track length*. The track length of the reconstructed track is an input into ReMId. Hadronic showers produce many short reconstructed tracks. The total track length provides a powerful discrimination between tracks originating from hadronic showers and muons.
- *Fraction of planes used in the dE/dx LL*.: the dE/dx LL variable is calculated on a limited number of planes in the track due to energy contamination

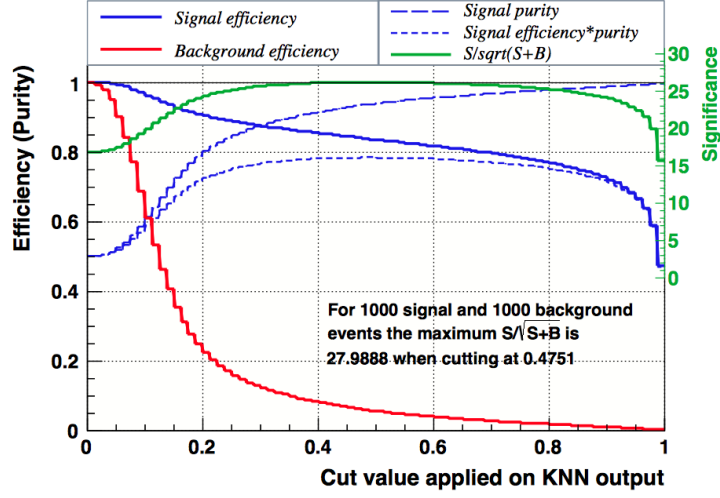


Figure 53: Sample efficiencies, purities, and FOM in a testing sample as a function of PID cut value, [65].

of the track. By excluding the planes with contamination, the dE/dx LL variable more accurately identifies the individual particle; however, information about the hadronic energy deposition of the track is lost. Muons have very little hadronic contamination as the muon produced in a CC interaction is back-to-back in center-of-mass frame with the hadronic shower.

At the end, a Multivariate Analysis is performed. ReMId uses a k-Nearest Neighbour (kNN) classifier to determine an overall PID value to characterize a track's likeness to a muon coming from a ν_μ CC event, see Figure 53.

Beside muon identification, containment cuts are needed to select well contained track inside the NO ν A Detector. The overall ND Selection is divided into two parts [70]: a pre-selection and the actual selection cut. These are described in the next two sub-sections.

5.4.1 Near Detector pre-selection

VALID NUMU CC ENERGY ESTIMATION It ensures that the ν_μ CC energy algorithm has returned a valid value for the energy. As the ν_μ CC energy estimation algorithm also requires that there is a 3D muon track in an

event, this ensures all slices selected have at least one 3D track that has been reconstructed as a muon.

NUMBER OF HITS IN SLICES As a slice is a cluster of hits associated/correlated between themselves, this cut requires that in each slice there must be at least 20 hits. Events with less than 20 hits are more likely to be due to NC interactions and are often not well reconstructed and are removed.

NUMBER OF CONTINUOUS PLANES Events crossing too few planes are very likely to be due to cosmic muons. Though their expected rate is very small at the ND, requiring that the number of continuous planes be greater than four will help remove any that would have otherwise been selected.

AT LEAST ONE TRACK IDENTIFIED BY THE COSMIC TRACKER The cosmic tracker looks for long straight tracks in the detector and will identify ND muon tracks from the beam. This selection is necessary for the FD cosmic muon rejection and is included here for consistency between the two detectors.

5.4.2 Near Detector Selection

NUMBER OF TRACKS Each reconstructed track has a number assigned. This cut ensures that the total number of reconstructed tracks is greater than zero, and that is greater than the track number assigned to the best track which the ReMID algorithm has classified as the best track.

SLICE CONTAINMENT CUTS Require that the slice does not extend to the edge of the detector. This ensures that minimal hadronic energy is lost outside of the detector and reduces the background from neutrino interactions outside the detector entering the detector: (i) the slice must be two cells from the edge of the detector; (ii) no activity in the first two planes of the detector; (iii) no activity in the last two planes of the detector.

VERTEX CONTAMINATION CUT Require that all vertices start inside the fully active region, and in particular 1.25 meters before the muon catcher such that a reasonable portion of the track energy is deposited outside the muon catcher.

TRACK CONTAINMENT CUTS (i) Require that the forwards projection of the track is greater than 4 cells from the edge of the detector, removes the contamination from neutrino interactions outside the detector. A cell is a $\sim 6 \times 4$ cm unit of the detector read out by a single APD pixel. (ii) Require that the

backwards projection of the track is greater than 8 cells from the edge of the detector. Removes events where the muon track is not fully contained in the detector.

AIR PASSING EVENTS Remove all events that could have exited the active region of the detector before reentering into the muon catcher. Require that the track stop before the muon catcher or that the position of the track at the transition plane between the fully active region and the muon catcher is less than 55 cm in y .

ENERGY DEPOSITS IN THE MUON CATCHER Removal of all events that deposit a significant amount of energy in the Muon Catcher. The Muon Catcher suffers from poorly calibrated channels and the NuMu CC energy estimation algorithm does not take this energy into account in its estimation. Require that the sum of the hadronic calorimetric energy in the muon catcher and in the transition plane between the detector and the Muon Catcher is less than 30 MeV.

REMIID SELECTION It requires that the response of the ReMIid selection algorithm is: $kNN > 0.75$.

5.5 DATA QUALITY

Since during these scans the HC was out of the nominal range, if the standard NO ν A Data Quality Cuts were applied here all the runs would have been considered as "bad". To escape the Data Quality Cuts, all the spills were considered as "good". This is justified from the fact that the ND was stable during the special runs week. A study on the data quality was then performed to ensure the quality of the data. The quality cuts that are usually applied to the data are [63]:

- a cut on the **number of protons on target (POT) per spill**: $\#POT > 2 \times 10^{12}$.

The POT number for each spill is determined by measurements taken with toroids along the proton beam line. The total POT is the sum of the POT for all spills. POT for a spill is considered "good" if the beam parameters for that spill are all within their acceptable ranges.

- a cut on the **Horn Current** value: $i - 2 < HC < i + 2$ where i is the HC for that run.

The HC is the sum of the normalized and shifted values for the HC from the four strip-lines; NSLINA, NSLINB, NSLINC and NSLIND, as described in Section 5.2.

- a cut to ensure **the beam is hitting the target in the right spot**: the beam position at the target should be more than 0.02 mm and less than 2.00 mm (both horizontal and vertical).
The horizontal and vertical beam positions on the target are calculated using measurements from the beam position monitors and the beam position intensity monitors.
- a cut on the **beam width** to ensure the beam is not too much spread: the width should be more than 0.57 mm and less than 1.58 mm.
The beam width is a measure of the horizontal and vertical extent of the beam. The spread of the beam at the target location in the beam line is calculated using voltage values on the wires of the beam profile monitor at that location.
- a cut on the **time difference** (Δt) between the spill time as recorded in the NOvA event files and the time recorded by the IFDB, specifically, DAQ event time - nearest IFDB time: $\Delta t < 5$ sec.

Table 5: Table shows the total number of spills and the spills considered good by the Data Quality Cuts, for each value of the Horn Current.

HC [kA]	# of spills	# of POT	# of good spills	# of good POT	(Good/Total) POT %
190	15858	$4.08214E + 17$	12804	$4.08228E + 17$	100
180	18130	$5.45108E + 17$	17256	$5.45074E + 17$	99
170	17636	$5.40012E + 17$	16942	$5.39980E + 17$	99
160	19938	$6.28462E + 17$	19279	$6.28429E + 17$	99
140	18379	$5.52355E + 17$	17824	$5.52297E + 17$	99

Table 5 shows, for each current, the total number of spills (all good for this analysis) and the spills considered good by the Data Quality Cuts. It is possible to see that quite 100% of all the spills passed the Data Quality Cuts. The POT have been summed up for each spill, to get the POT for each HC.

The previous cuts were applied at spill level. To make sure the detector was responding correctly during the special runs, a further study was done looking at the data after the following cuts (at event level) were applied:

- one cut that allow to detect when the electronics is not reporting data;
- one cut that allow to detect when the detector is out of time syntonization.

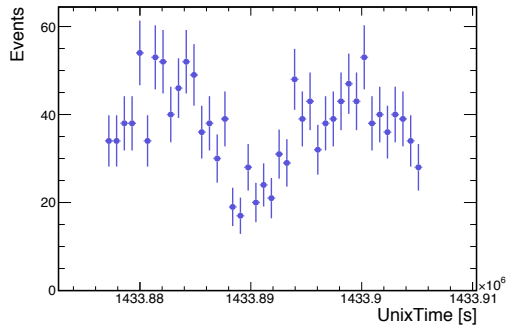
The results are shown in Table 6.

Table 6: Table shows the number of POT accumulated for each spill, the number of events selected without Data Quality Cuts and with Data Quality Cuts applied.

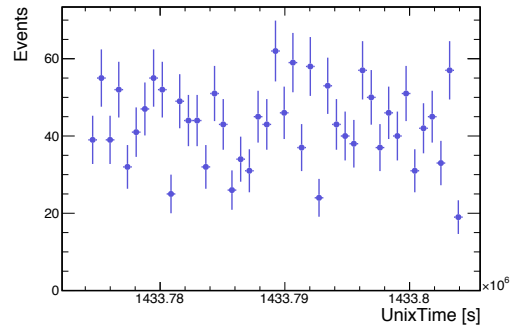
HC [kA]	Accumulated POT	Selected Events w/o data quality cuts	Selected Events w/ data quality cuts	Ratio %
200	$1.66E + 20$	509358	502179	98.6
190	$4.08E + 17$	1250	1239	99.1
180	$5.45E + 17$	1622	1607	99.1
170	$5.40E + 17$	1572	1557	99.0
160	$6.29E + 17$	1847	1831	99.1
140	$5.52E + 17$	1536	1514	98.7

To ensure the detector was always up and running during the Special Runs the number of events recorded every ~ 10 minutes were plotted. Plots are shown in Figure 54. The Unix time represented in these plots is the time when the event was recorded. It is expressed in *Unix time*. The number of event recorded in time is almost constant as expected.

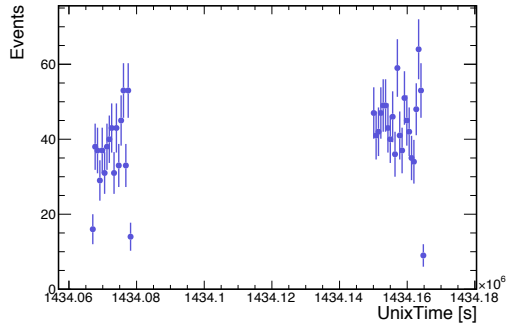
5 HORN CURRENT STUDIES



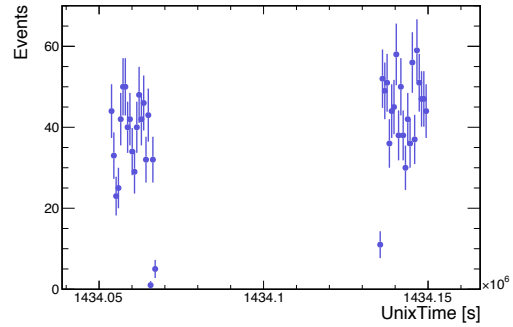
(a) *Special Run at 140 kA.* The number events goes down in the middle because the beam intensity was less than nominal during that time.



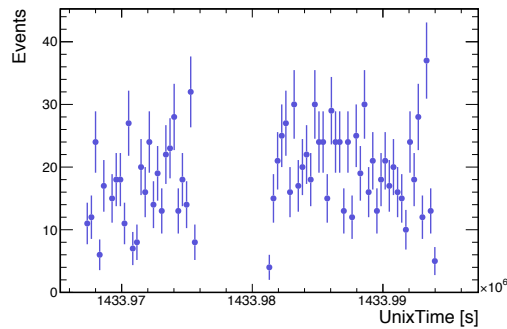
(b) *Special Run at 160 kA.*



(c) *Special Run at 170 kA.* There is a gap because data was taken in two consecutive days.



(d) *Special Run at 180 kA.* There is a gap because data was taken in two consecutive days.



(e) *Special Run at 190 kA.* There is a gap because the beam was down for approximately one hour.

Figure 54: Events revealed at the Near Detector as a function of time. Each point is number of events every ~ 10 minutes.

5.6 DATA ANALYSIS

Since events relative to different special runs correspond to a different exposure of POT, it is needed to scale the events to the same number of POT to allow a yield comparison between different runs.

For each HC value, data were taken for approximately 8 hours (1 shift). Since one shift corresponds on the average to 5.98×10^{17} POT, all the events in the following will be presented scaled to 5.98×10^{17} POT, i.e.

$$(final\ evts\ @\ i) = (evts\ @\ i) \frac{5.98 \times 10^{17}}{POT\ @\ i}$$

where i is the value of the HC.

The number of events at 200 kA allows a comparison with the other HC runs and was also used to normalize the FR output.

At the time of this analysis, the total number of accumulated POT running with nominal conditions (HC = 200 kA) was 1.66×10^{20} . The total number of events that passed the previous cuts are 509358 ± 714 (stat). Normalizing at 5.98×10^{17} POT the number of events is 1838.6 ± 2.6 . If then one applies a cut on the reconstructed energy to select the oscillation region (1 to 3 GeV), 1634.8 ± 2.4 are left. It is important to look at the number of events in that energy region because neutrino around 2 GeV of energy are most likely to oscillate (see Chapter 3).

In Figure 55 is shown the neutrino reconstructed energy distribution for the candidate events obtained after the selection. Figure 56 shows the number of neutrino events detected as a function of the HC. Table 7 summarizes these values and also shows the fraction of neutrino data lost when the HC is lowered. Table 9 shows the number of events in the oscillation region only.

To allow a comparison between the reconstructed energy distribution at 200 kA with the ones obtained from the different special runs, they are plotted together in Figure 57.

5.6.1 Peak Position

It is interesting to look at the shape of the neutrino energy distribution. As described in Chapter 3, the ν_μ energy should be peaked at 2 GeV since at that energy the oscillation probability is maximal.

To look at how the peak position changes with the HC, the reconstructed energy distributions were fitted with a truncated gaussian in the proximity of

5 HORN CURRENT STUDIES

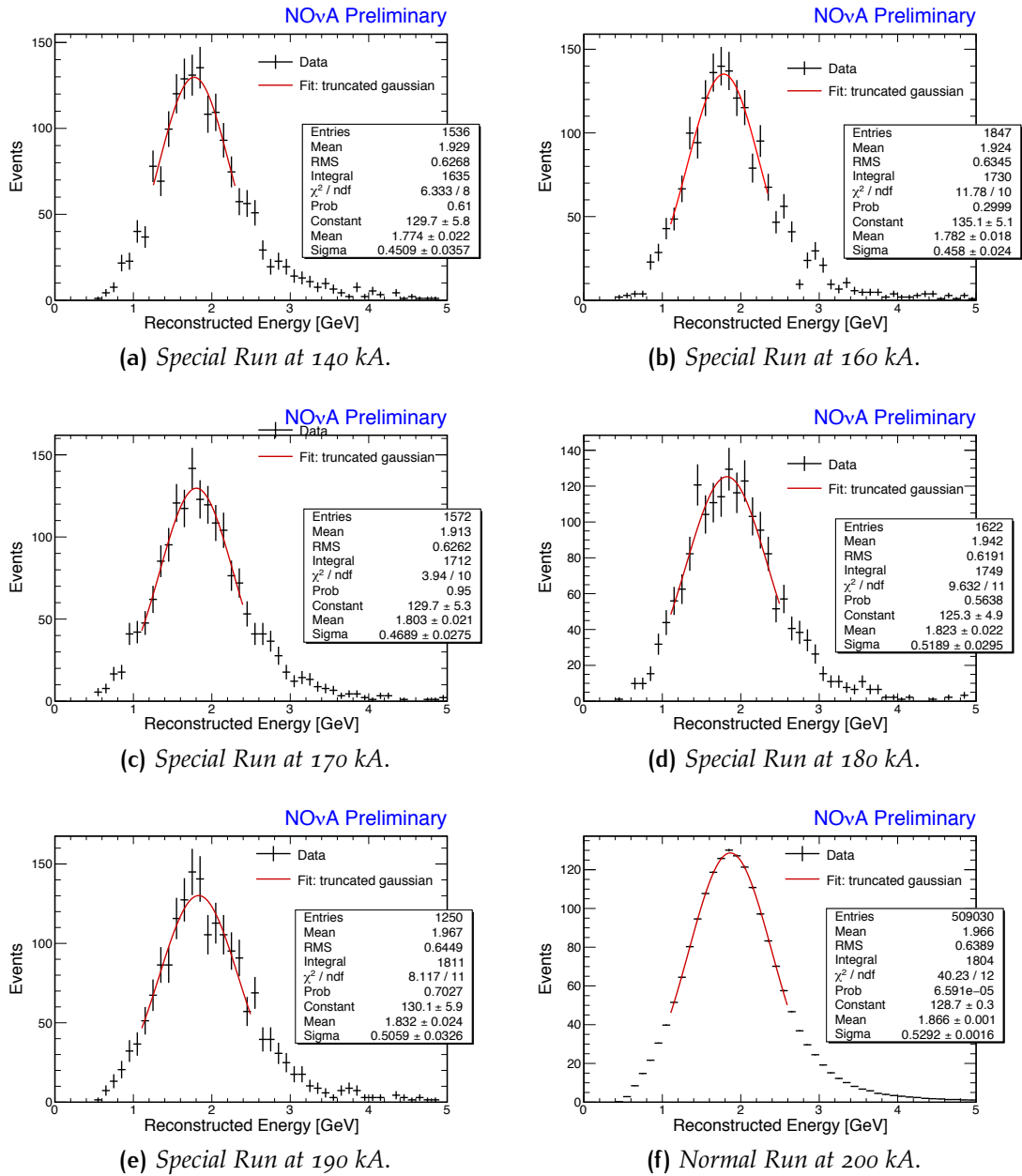


Figure 55: Neutrino reconstructed energy distributions. Data are shown with black points. The red fit is a truncated gaussian, the goal is to find the peak position of the distribution as the HC changes, see also Figure 58.

Table 7: Number of selected ν_μ CC events at the NO ν A Near Detector for different values of the Horn Current. Errors are statistical only.

HC [kA]	Selected Events	Accumulated POT	Selected Events / 5.98e17 POT	(evts @ i)-(evts @ 200) percent
200	509030 \pm 713	1.66E20	1837.6 \pm 2.6	0
190	1250 \pm 35	4.08E17	1831 \pm 52	-0.4 \pm 2.8
180	1622 \pm 40	5.45E17	1779 \pm 44	-3.2 \pm 2.4
170	1572 \pm 40	5.4E17	1741 \pm 44	-5.3 \pm 2.4
160	1847 \pm 43	6.29E17	1757 \pm 41	-4.4 \pm 2.2
140	1536 \pm 39	5.52E17	1663 \pm 42	-9.5 \pm 2.3

Table 8: Number of selected ν_μ CC events at the NO ν A Near Detector for different values of the Horn Current. An energy cut as been applied on the reconstructed energy to show events in the [1,3] GeV energy region. Errors are statistical only.

HC [kA]	Selected Events	Accumulated POT	Selected Events / 5.98e17 POT	(evts @ i)-(evts @ 200) percent
200	448253 \pm 670	1.66E20	1618.0 \pm 2.4	0
190	1111 \pm 33	4.08E17	1627 \pm 49	0.6 \pm 3.0
180	1451 \pm 38	5.45E17	1592 \pm 42	-1.6 \pm 2.6
170	1384 \pm 37	5.4E17	1532 \pm 41	-5.3 \pm 2.5
160	1650 \pm 41	6.29E17	1570 \pm 38	-2.8 \pm 2.4
140	1367 \pm 37	5.52E17	1480 \pm 40	-8.5 \pm 2.5

the peak. The fits are shown in Figure 55. The plot if Figure 58 shows the mean of the fitted gaussian VS the HC.

The variation of the peak position with the HC is shown in Table 9.

5 HORN CURRENT STUDIES

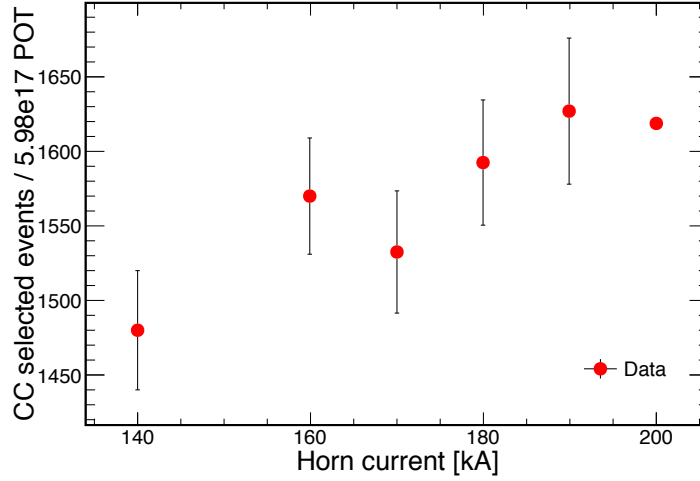
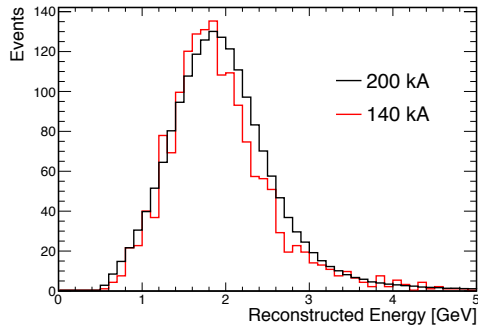


Figure 56: Number of selected ν_μ CC events at the NO ν A Near Detector as a function of the Horn Current. An energy cut was applied on the reconstructed energy to show events in the [1,3] GeV energy region. Errors are statistical only.

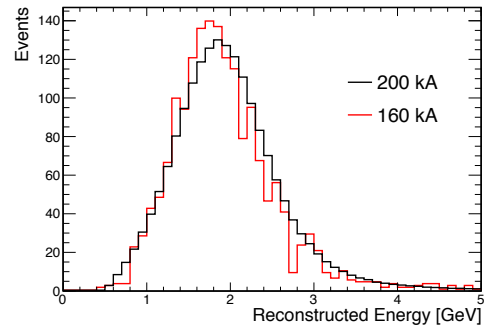
Table 9: This table shows how the peak position of the reconstructed energy distribution changes with the Horn Current, see also Fig. 58.

HC [kA]	(peak pos. @ i)-(peak pos. @ 200) percent
200	0
190	-1.8 ± 1.3
180	-2.3 ± 1.2
170	-3.4 ± 1.1
160	-4.5 ± 0.9
140	-4.9 ± 1.2

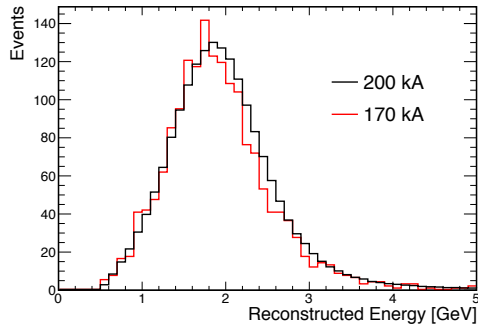
5 HORN CURRENT STUDIES



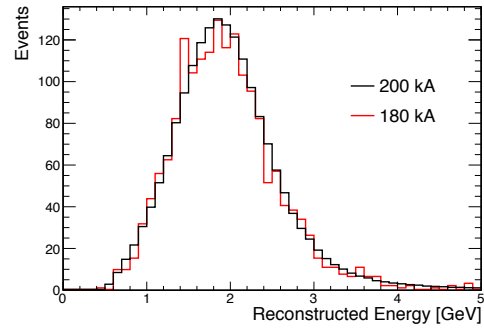
(a) *Special Run at 140 kA.*



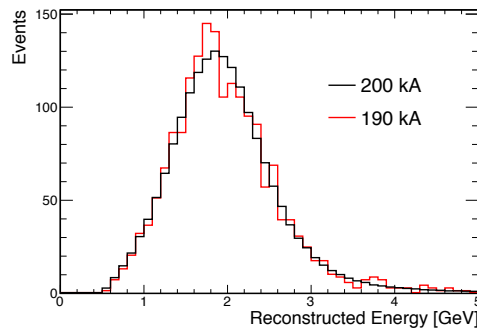
(b) *Special Run at 160 kA.*



(c) *Special Run at 170 kA.*



(d) *Special Run at 180 kA.*



(e) *Special Run at 190 kA.*

Figure 57: Neutrino reconstructed energy distributions from data taken during the Special Runs. The black distribution shows the neutrino reconstructed energy when running with nominal conditions (200 kA). The red distribution shows the same but for the different special runs: 140, 160, 170, 180 and 190 kA.

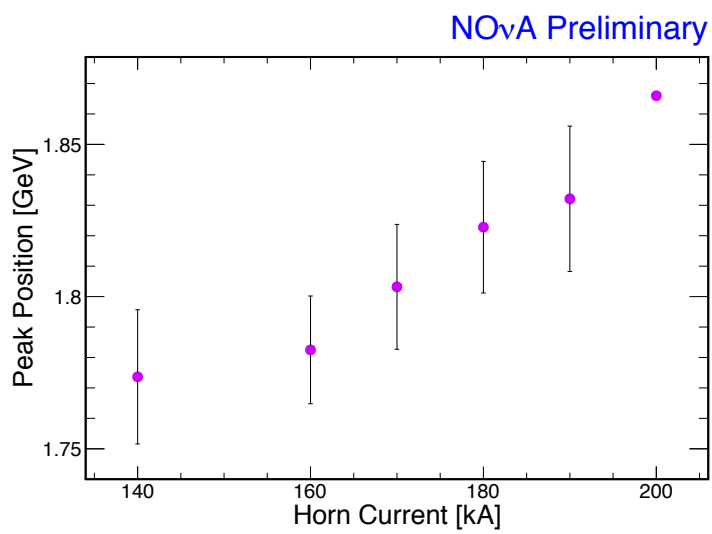
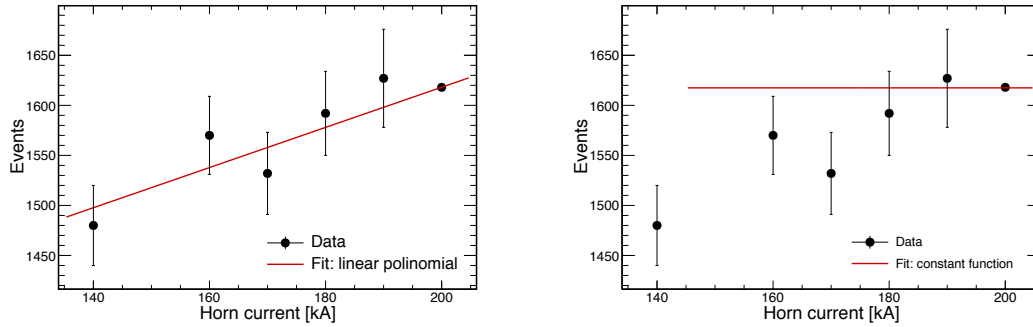


Figure 58: Peak position of the reconstructed energy distribution as a function of the Horn Current. The peak position was evaluated fitting the reconstructed energy spectrum with a truncated gaussian in the proximity of the peak.

5.7 DATA FITS

Two different types of fit have been applied to the data points shown in Figure 56: a linear and a constant fit. The last one was performed without the point at 140 kA and it is meant to determine the likelihood that the neutrino yield is constant between 160 and 200 kA. The fits are shown in Figs. 59.



(a) Linear fit. $\chi^2 = 1.7$, $N_{df} = 4$, $p0 = 1218 \pm 99$, $p1 = 2.0 \pm 0.5$. P-value= 79%. (b) Constant fit. Point at 140 kA excluded from the fit. $\chi^2 = 8.7$, $N_{df} = 4$, $p0 = 1634 \pm 2$. P-value= 7%.

Figure 59: These figures show the number of ν_μ CC selected events as a function of the Horn Current, together with a linear and a constant fit.

5.8 THE NOVA SIMULATION CHAIN

In the next Sections Data are compared with the MC simulation adopted by NOVA . The whole Simulation Chain includes also the Detector Simulation [2] allowing to compare the neutrino reconstructed energy distributions obtained from the Data and the Simulations.

The steps to simulate neutrino interactions and backgrounds are illustrated in Figure 60. The neutrino beam simulation was described in details in Chapter 4. It starts with modeling hadron production within the Target, focusing in the Horns, and downstream tertiary production to determine the production rate and energy spectrum of each neutrino flavor from the decay of pions, kaons, and muons in the decay pipe using the FLUGG simulation package. The resulting simulated neutrinos are stored in flux files along with information about their parentage, and they are used as inputs to the neutrino event generation stage

performed with GENIE. Factorizing out the simulation of the neutrino flux from the rest of the simulation minimizes the number of times this computationally intensive step needs to be run as well as allowing for after the fact tunings of hadron production or focusing parameters. Cosmic ray events are generated with CRY [6]. The particle lists generated by either GENIE or CRY are then passed to Geant4, which propagates particles through the detector and produces energy deposits in active material. Finally, the list of energy deposits in active material are passed to a parametrized front-end simulation which converts energy deposits into scintillation light, transports scintillation light to the APD, and simulates the readout electronics response. The final output is formatted like raw data.

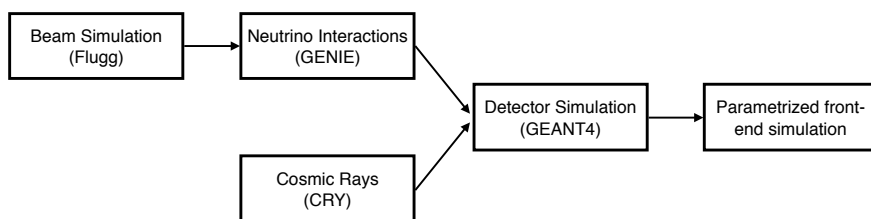


Figure 60: Steps in simulation chain for the NO ν A experiment, [2].

5.9 SYSTEMATICS

In this analysis, the following systematic uncertainties have been accounted for, [57]: cosmic ray backgrounds, detector alignment, neutral currents (NC) backgrounds, ν_τ backgrounds, POT accounting and detector mass (combined into an overall relative normalization uncertainty), GENIE modeling of final state particles of neutrino-nucleus scattering, modeling of the detector response, relative and absolute energy scales, and the hadronic energy correction. The following subsections describe each item in some detail.

5.9.1 NuMI Flux Uncertainties

Detailed studies of uncertainties in the neutrino flux are shown in [14]. Flux uncertainties are dominated by hadron production uncertainties, estimated by comparing NuMI target MC predictions to thin-target data published by the NA49 collaboration.

Also hadron transport uncertainties have been studied. Transport uncertainties arise from uncertainties in the NuMI target and horn positions, HC and magnetic field uncertainties, and beam spot size and position. The study includes variations in parameters associated with the beam transport, simulating neutrino flux at the NOvA detectors:

- Horn Current shifted by ± 1 kA w.r.t nominal;
- Horn1 position shifted by ± 2 mm both in x and y w.r.t nominal;
- Horn2 position shifted by ± 2 mm both in x and y w.r.t nominal;
- Magnetic field distribution changed to an exponential magnetic field distribution (0.77 cm skin depth) in the horn skin;
- Beam position on the target shifted by ± 0.5 mm in x and y separately;
- Beam spot size shifted by ± 0.2 mm both in x and y w.r.t nominal;
- Target position shifted by ± 2 mm shift w.r.t nominal.

All these uncertainties are estimated to be small compared to the hadron production uncertainties.

5.9.2 Detector related Uncertainties

The systematic uncertainties accounted for in this analysis are summarized in the following and determined as in [57].

COSMIC RAY BACKGROUNDS Cosmic ray backgrounds are measured directly from data collected outside of the NuMI spill, and therefore the only systematic uncertainty related to this background is the statistical uncertainty in the measured background rate. The out-of-time data are recorded in a $\sim 500 \mu\text{s}$ wide window in which the $12 \mu\text{s}$ -wide NuMI beam spill occurs. Data recorded between $25 - 475 \mu\text{s}$ within the NuMI spill trigger, with the exception of a $30 \mu\text{s}$ window around the NuMI beam spill that is blinded to the analysis, are used to measure the cosmic ray backgrounds. The resulting $420 \mu\text{s}$ of cosmic ray data, or a factor of about 35 more of cosmic ray data than NuMI spill data result in negligible systematic uncertainty in the background rate.

DETECTOR ALIGNMENT The effect of mis-modeling the detector alignment is determined by studying how the selected energy spectrum changes between simulation samples with nominal and staggered geometries. It was shown that the expected amount of mis-modeling has negligible effect and is ignored in this analysis.

NC BACKGROUNDS The NC backgrounds are estimated using the MC prediction. The uncertainty on this background is taken as 100% of the predicted rate.

ν_τ **BACKGROUNDS** The ν_τ backgrounds from beam contamination are studied by using the tau-swapped flux MC in order to enhance the number of ν_τ interactions in the detector. The study found approximately 0.04 tau events per 10^{20} POT. As this number is already very small, a 100% uncertainty on this predicted background is assumed.

NORMALIZATION The mass uncertainty of the fiducial volume of the detector can lead to a systematic error on the total exposure. In order to constraint this normalization uncertainty a survey of the detector mass was performed. Measurements of specific basic components of the detector were used in the present analysis: extrusions, scintillator, glue, and fiber to determine the average unit of mass and its associated uncertainty in the fiducial volume of the detector. The measurements of the detector components come from the as built detector when available and specified part tolerances when no measurements data was available. From this mass accounting a 0.7% relative uncertainty on the mass of both the ND and FD was found. Systematic uncertainties related to POT arise from periods when NuMI spills were recorded in only one detector. The stability of the POT measurement over time is better than 0.5%, which is the conservative estimate used for the POT normalization systematic. The combined conservative normalization systematic uncertainty is therefore 0.9%.

ν_μ - **NUCLEUS SCATTERING AND HADRONIZATION** The GENIE MC provides a mechanism for re-weighting events by altering parameters used to calculate cross sections and final state particles exiting the nucleus. There are 67 such "knobs", and they have been changed by $\pm 1, 2\sigma$ to see the impact on the ν_μ CC energy spectrum

DETECTOR RESPONSE MODELING Detector modeling systematics come from uncertainties in the GEANT simulation of the response of the detector, the time-dependent masking of detector channels, and the tuning of the simulated light levels, photon transport and electronics response in the

detectors. Uncertainties in the GEANT simulation of the response of the detector are estimated by comparing MC with alternative GEANT4 physics lists that use different models to simulate hadronic interactions and nuclear de-excitation.

CALIBRATION ENERGY SCALE Energy scale shifts have been propagated all the way through the full reconstruction and analysis chain to estimate the uncertainties due to calibration systematics. A conservative 5% uncertainty in both the absolute and relative energy scale is assumed.

HADRON ENERGY CORRECTION The systematic uncertainty on the E_{had} correction has two parts - an absolute error (the same in the ND and FD), and a relative error (potentially different between the ND and FD). The absolute hadronic energy scale error is taken to simply be 100% of the size of the shift, as described in Section 5.3.1. The relative energy scale is assessed by assuming that the E_{had} correction is driven by uncertainties in modeling the production of final-state particles in neutrino interactions and/or modeling how these final state particles interact with the detectors.

5.10 DATA – MONTE CARLO COMPARISON

FR doesn't include the whole detector simulation. The flux is considered only in 1 m radius circle placed at the center of the upstream face of the detector. It also returns a number of events per kton.

Moreover, FR outputs the true neutrino energy, while the data are presented in terms of reconstructed energy. To compare data and MC prediction, the detector simulation at 200 kA was then used.

A 2-dimensional histogram was created to store true neutrino energy and reconstructed neutrino energy. The true energy axis of this histogram has then been re-weighted using the FR true energy distribution. This allows to use the detector simulation at 200 kA as reference and scale it with the new flux, provided by FR. At the end one remains with the whole simulation chain for all the different values of the HC.

Figure 61 shows the neutrino energy distribution for the data (black points) and the predicted one from the MC simulations (solid red line). The light red bands show the MC systematic errors as described in Section 5.9. The ratio between data and MC is shown in figure 62.

5 HORN CURRENT STUDIES

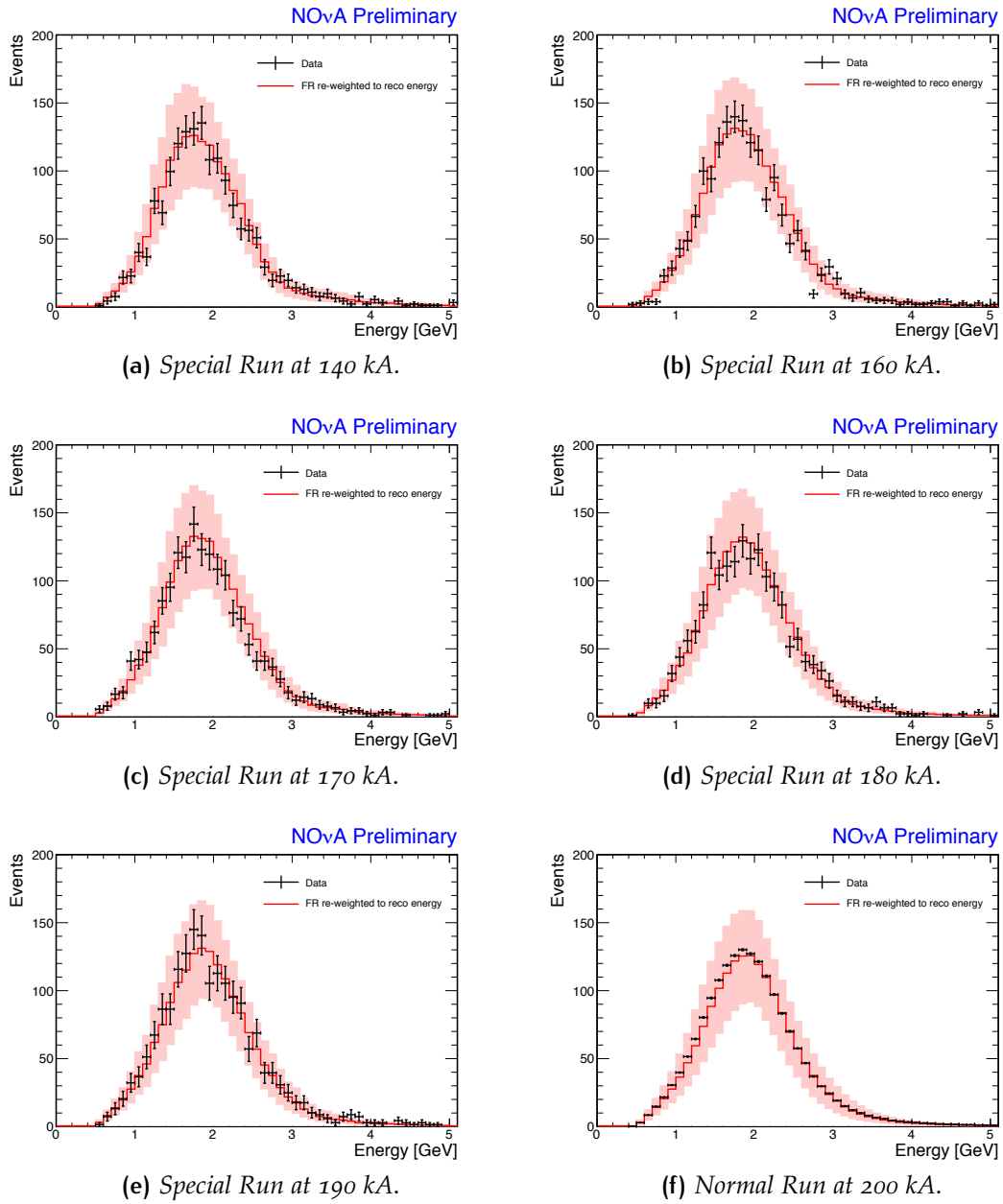
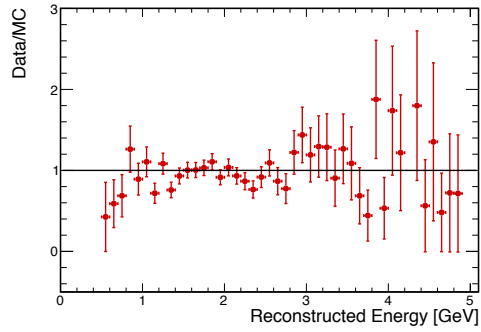
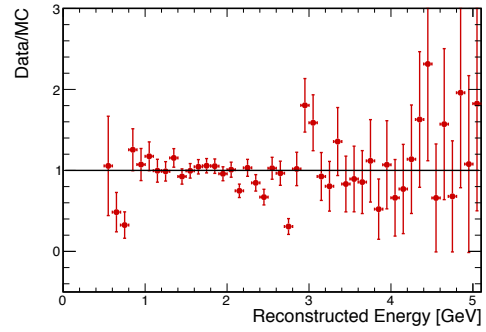


Figure 61: Neutrino reconstructed energy distributions. Data points are shown in black. The red distribution is the MC predicted reconstructed energy. The light red band is the systematic error on the MC.

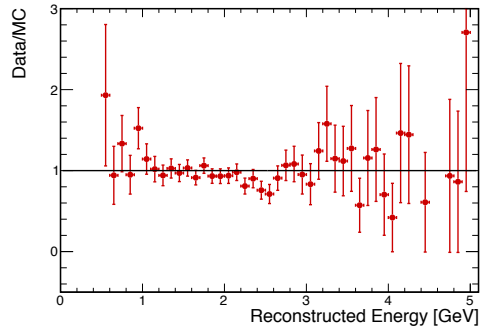
5 HORN CURRENT STUDIES



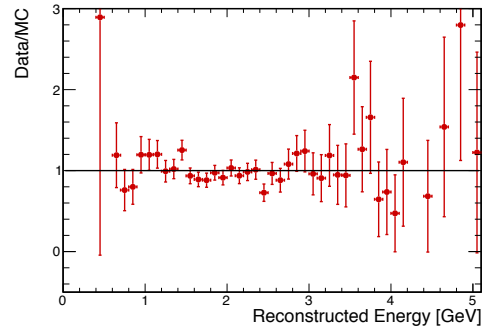
(a) *Special Run at 140 kA.*



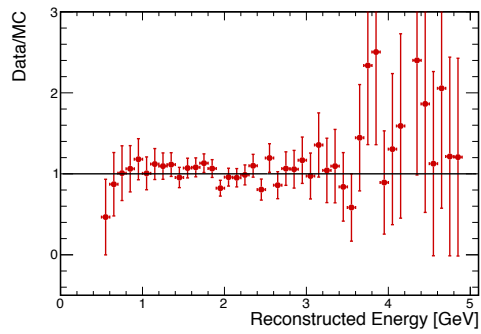
(b) *Special Run at 160 kA.*



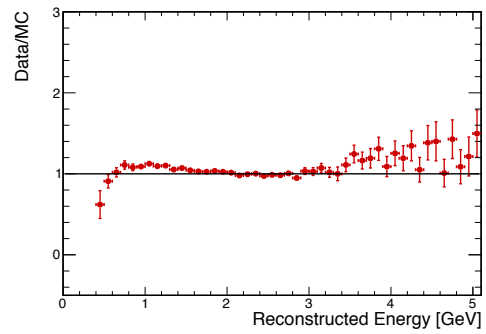
(c) *Special Run at 170 kA.*



(d) *Special Run at 180 kA.*



(e) *Special Run at 190 kA.*



(f) *Normal Run at 200 kA.*

Figure 62: Ratio between data and MC of the distributions in Figure 61.

Since huge statistics is available at 200 kA (circa 500,000 events), a scale factor has been retrieved to convert the FR output to number of events expected at the ND.

The point at 200 kA was then considered fixed by the data and this allows FR to predict the number of events at $i = 190, 180, 170, 160$ and 140 kA in this way:

$$\text{Events at } i \text{ kA} = \frac{(\text{FR evts at } i \text{ kA})}{(\text{FR evts at } 200 \text{ kA})} \cdot (\text{ND selected evts at } 200 \text{ kA}) \quad (42)$$

Figure 63 shows the number of events as a function of the HC in black and the predicted points from FLUGG and G4NuMI in red and blue respectively. The two bands represented in the plots are not the MC statistical or systematic errors, but are 1σ and 2σ deviations from the FR simulated point n , i.e. $\pm\sqrt{n}$ and $\pm 2\sqrt{n}$. If the prediction is correct, we expect the data point to be constraint in these two bands at 1 and 2 σ level. Figure 64 show data, FLUGG and G4NuMI all in the same plot.

The ratio between data and MC is shown in Fig. 65 for both FLUGG and G4NuMI.

If one uses the FR predicted number of events at the MINOS ND, pinning at 200 kA and then using the points in Figure 49a to predict the events at lower HC, then gets the plot in Figure 66. In this Figure data points are shown in black and the FR predicted points in red for FLUGG and blue for G4NuMI. As it's possible to see, data points are certainly not compatible with the big event reduction predicted for an on-axis detector.

Table 10 shows the total number of selected events and the relative POT exposure for each special run, the number of events scaled to the same number of POT (5.98×10^{17}) and the expected events from FLUGG and from G4NuMI.

5 HORN CURRENT STUDIES

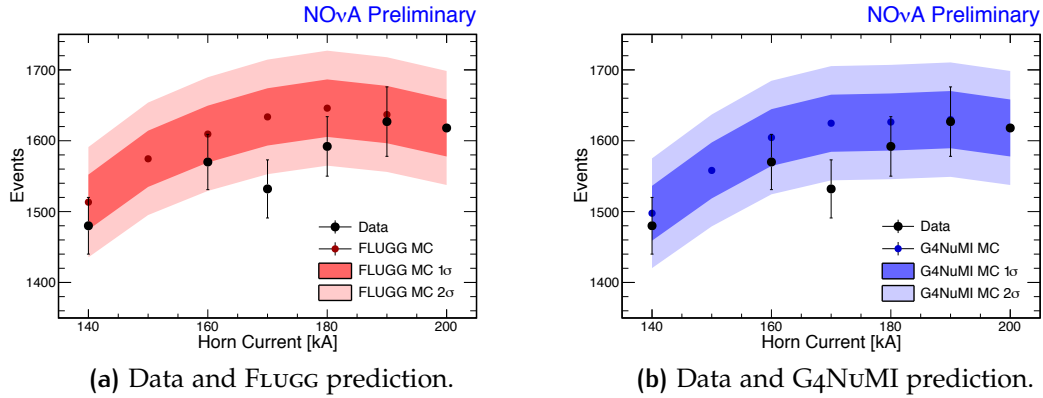


Figure 63: Number of selected ν_μ CC events at the NO ν A Near Detector for different values of the HC. Data events are shown in black while simulated events are shown in red (FLUGG) and blue (G4NuMI). The two bands represented are not the MC statistical or systematic errors, but are 1σ and 2σ deviations from the FR simulated point, i.e. $\pm\sqrt{n}$ and $\pm 2\sqrt{n}$ where n is the FR simulated point.

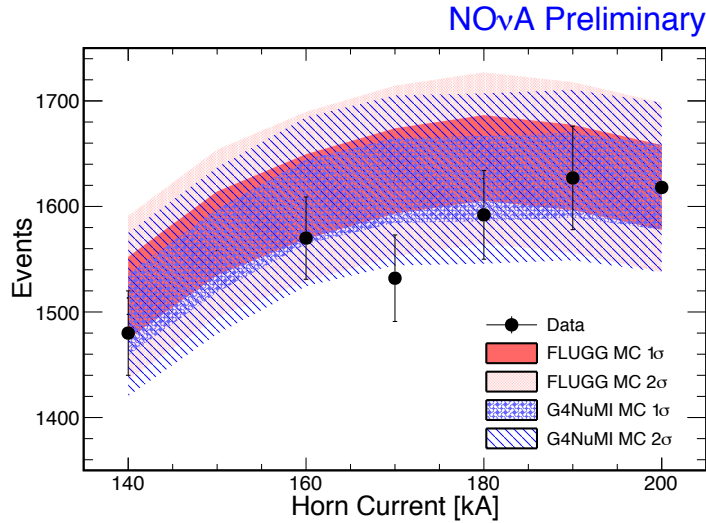


Figure 64: Number of selected ν_μ CC events at the NO ν A Near Detector for different values of the Horn Current. Data events are shown in black while simulated events are shown in red (FLUGG) and blue (G4NuMI). The two bands represented are not the MC statistical or systematic errors, but are 1σ and 2σ deviations from the FR simulated point, i.e. $\pm\sqrt{n}$ and $\pm 2\sqrt{n}$ where n is the FR simulated point.

5 HORN CURRENT STUDIES

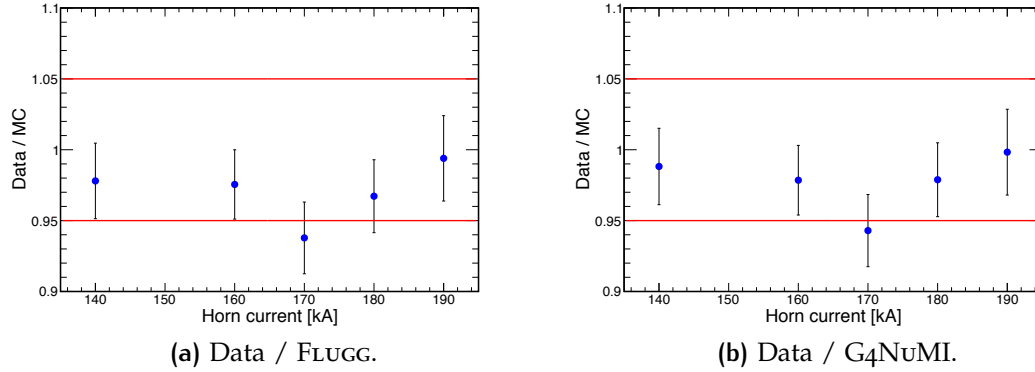


Figure 65: Ratio Data / MC of plots in Figure 63. The 2 red lines show $\pm 5\%$ band on the ratio.

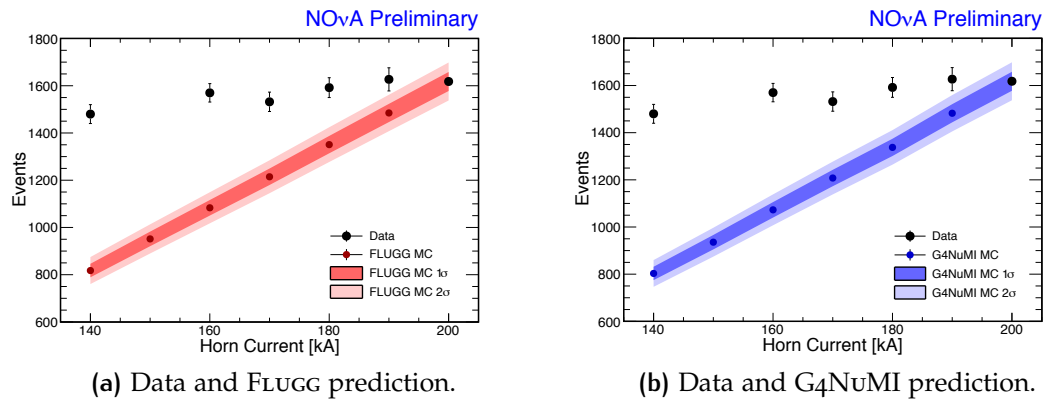


Figure 66: Black points show the number of selected ν_μ CC events at the NOvA ND for different values of the HC. Red (FLUGG) and blue (G₄NuMI) points show the simulated events at the MINOS ND. The two bands represented are not the MC statistical or systematic errors, but are 1σ and 2σ deviations from the FR simulated point, i.e. $\pm\sqrt{n}$ and $\pm 2\sqrt{n}$ where n is the FR simulated point.

Table 10: Number of selected ν_μ CC events at the NO ν A Near Detector for different values of the Horn Current. An energy cut was applied on the reconstructed energy to shown events in the [1,3] GeV energy region. Errors are statistical only.

HC [kA]	Selected Events	Accumulated POT	Selected Events / 5.98e17 POT	FLUGG Expected / 5.98e17 POT	G4NuMI Expected / 5.98e17 POT
200	448253 \pm 670	1.66E20	1618.0 \pm 2.4	-	-
190	1111 \pm 33	4.08E17	1627 \pm 49	1623 \pm 5	1647 \pm 6
180	1451 \pm 38	5.45E17	1592 \pm 42	1638 \pm 5	1643 \pm 6
170	1384 \pm 37	5.4E17	1532 \pm 41	1627 \pm 5	1642 \pm 6
160	1650 \pm 41	6.29E17	1570 \pm 38	1608 \pm 5	1621 \pm 6
140	1367 \pm 37	5.52E17	1480 \pm 40	1511 \pm 5	1513 \pm 6

5 HORN CURRENT STUDIES

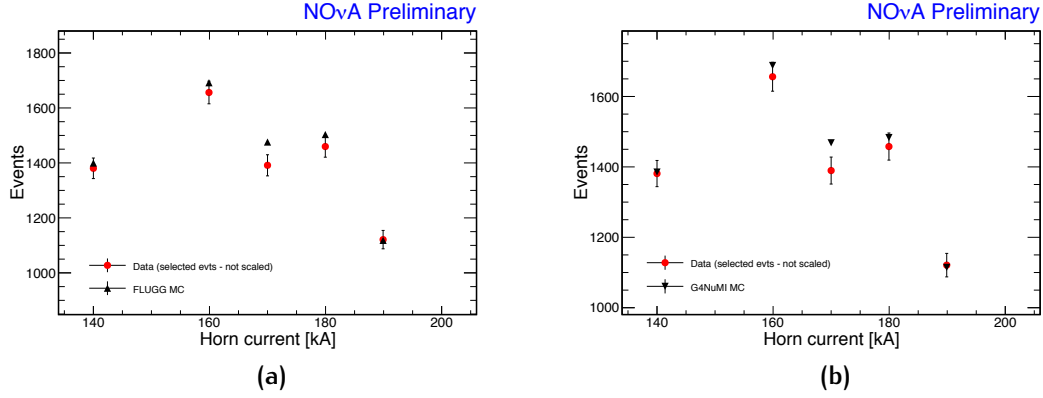


Figure 67: Red points are data points. Black triangles show the predicted number of events by FLUGG (left) and G4NuMI (right). Different runs are not scaled by the same number of POT.

5.11 DATA – MC FITS

Two different fits have been performed in order to study the data/MC agreement. First, a likelihood test was performed. The plots in Figure 67 show the number of events counted for each value of the HC in red. These values are not scaled by any POT number, so they correspond to different accumulated POT. The black points are the FR expected events scaled by the POT value of the data. Given that, a likelihood function can be constructed as a product of probabilities to get the number of events obtained, given the FR expected values:

$$L(n|y) = \prod_{i=1}^M \frac{e^{-y_i} y_i^{n_i}}{n_i!}$$

where n_i is the number of events from the data, y_i is the number of predicted events by the simulation and M is the number of special runs. Then a chi-squared test can be performed in the following way [9]:

$$\chi^2 = -2 \ln \frac{L(n|y)}{L(n|\nu)}$$

And, for the poissonian case:

$$\chi^2 = -2 \sum_{i=1}^M \left(n_i \ln \frac{y_i}{n_i} \right) + 2(N_0 - N)$$

5 HORN CURRENT STUDIES

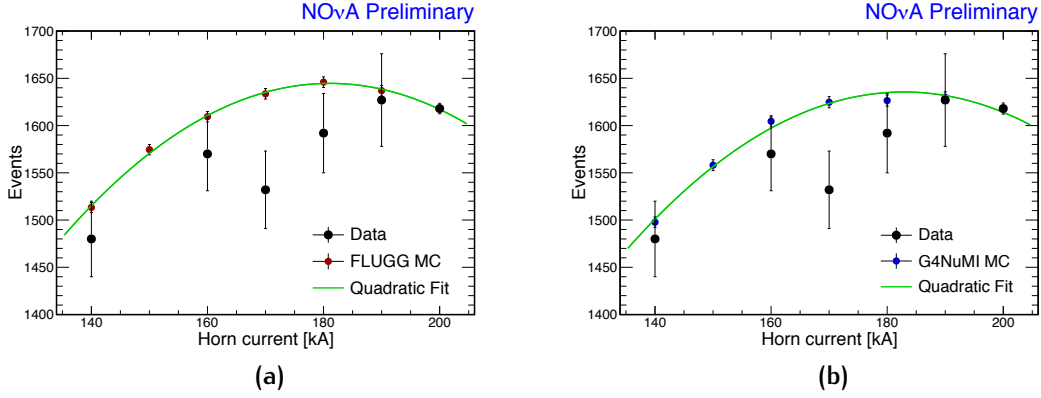


Figure 68: Black points are data points. Red and blue points show the predicted number of events by FLUGG (left) and G4NuMI (right). The quadratic fit on the simulated points is shown in green.

where N is the total number of events from the data, summing up events for all the special runs and N_0 is the expected number from the simulation. The results are (degree of freedom = 5):

$$\begin{array}{llll}
 \text{FLUGG} & \chi_F^2 = 7.5 & \Rightarrow & \text{P-value} = 18.6\% \\
 \text{G4NuMI} & \chi_G^2 = 5.4 & \Rightarrow & \text{P-value} = 39.6\%
 \end{array} \quad (43)$$

The second fit is described in the following. The FR predicted points have been fitted using a parabolic function $y = a + bc + cx^2$, as shown in Fig. 68, where the FR points are shown with red and blue dots. The data points are shown in black. Then a χ^2 test was performed to see how much the data follow the parabolic behavior. Extracting a , b and c from the FR fit, the χ^2 on the data points was evaluated as:

$$\chi^2 = \sum_{i=1}^M \left(\frac{z_i - y_i(x_i, a, b, c)}{\sigma_i} \right)^2$$

where M is the number of points, z_i are the data points, y_i are the fitted functions evaluated at x_i , x_i are the HC values and σ_i are the uncertainties on the data points. The results are (degree of freedom = 5):

$$\begin{array}{llll}
 \text{FLUGG} & \chi_F^2 = 9.8 & \Rightarrow & \text{P-value} = 8.1\% \\
 \text{G4NuMI} & \chi_G^2 = 6.9 & \Rightarrow & \text{P-value} = 23.6\%
 \end{array} \quad (44)$$

The comparison between data and the two MC packages thus shows fair agreement at this first stage of analysis.

CONCLUSIONS

The NO ν A off-axis long-baseline neutrino oscillation experiment uses an almost pure ν_μ beam produced in the Fermilab NuMI beam line. The NO ν A detectors are now fully operational and the First Oscillation Results were presented on August 6, 2015 [60].

The NuMI neutrino beam regularly operated with a beam power of 400 kW and reached a record beam power of 521 kW. Future upgrades are on track to increase the power to the final specification of 700 kW. The NuMI beam had 85% uptime for the period of data-taking described in this thesis and exceeded design goals for POT delivered.

This thesis presents a study of the NuMI beam line intended to clarify how the particle trajectories through the focusing system and consequently the neutrino event yield are affected by the variation of the Horn Currents.

In order to understand the pion trajectories for pions that produce neutrinos, the Ancestor List was developed and implemented in the FLUGG code. The Ancestor List allows to keep track of every particle produced that contribute to the neutrino flux: from the final neutrino to the initial proton. For every particle and every time such particle undergoes an interaction, the material, vertex, momenta and identities of the particle are recorded in the Ancestor List. These information enable a study of the contributions from a variety of hadronic interactions that leads to neutrino production. MC models based on available hadron production data can be tuned accordingly. This also allows to optimize the neutrino beam. In this thesis the Ancestor List was indeed used to reconstruct the pion trajectories along the beam line.

As a result of this study, almost all the pions providing on-axis neutrinos are found to be under-focused, while the off-axis spectrum is slightly more due to over-focused pions. As shown by simulations, as the Horn Currents are turned down from the nominal value of 200 kA, the over-focused and under-focused components of the off-axis spectrum swap, keeping the number of events almost constant down to 160 kA. The neutrino yield goes significantly down if the currents are further reduced to 140 kA or lower values.

These simulations have been compared to the data. The predicted number of ν_μ CC events at the NO ν A ND has been compared with the data taken in one week starting from June the 8th to June the 12th 2015. The Horn Currents

have been decreased to 190, 180, 170, 160 and 140 kA. The data taking period for each Horn Current is about 8 hours each, that correspond to an exposure of approximately 5×10^{17} POT. Selecting only events in the oscillation region (i.e. with energy between 1 and 3 GeV), the variation between the number of events at 160 and at 200 kA is:

$$\frac{(\text{Evs. @ 160}) - (\text{Evs. @ 200})}{(\text{Evs. @ 200})} = (-2.8 \pm 2.4) \%$$

Although the simulations showed a flat behavior down to 160 kA, data show a small reduction in the number of events at the NO ν A ND. This event drop is quite small compared to the predicted event drop on-axis.

A further study was done to understand how the peak position of the ν_μ energy distribution changes with the horn current. The ν_μ energy should be peaked at 2 GeV since at that energy the oscillation probability is maximal. The percent variation between the peak position at 160 and at 200 kA is:

$$\frac{(\text{Peak pos. @ 160}) - (\text{Peak pos. @ 200})}{(\text{Peak pos. @ 200})} = (-4.5 \pm 0.9) \%$$

The NuMI Horns are now working with a current of 200 kA, that is the maximum current they were designed to sustain. Lower Horn Current will put much less stress on the stripline, it can then be a solution to avoid Horns malfunctions. The Horns heat up due to the pulsed current and radiation and Horn 1 will be near the edge of its design for heating of the inner conductor at 700 kW. If the Horn Current is decreased in future running, this will improve the Horn lifetime. Running at lower Horn Current will be considered by the NO ν A experiment and the Fermilab Accelerator Division as a potential solution to avoid future malfunctioning of the NuMI Horns.

BIBLIOGRAPHY

- [1] Mar. 2015. URL: <http://science.energy.gov/hep/facilities/user-facilities/fermilab-accelerator-complex/>.
- [2] A. Aurisano. “The NOvA Detector Simulation”. In: *NOvA doc-db 13577* (2015).
- [3] M. Beuthe. “Oscillations of neutrinos and mesons in quantum field theory”. In: *Phys. Rept.* 375 (2003), pp. 105–218. URL: <http://arxiv.org/abs/hep-ph/0109119>.
- [4] Rene Brun and Fons Rademakers. “ROOT - An Object Oriented Data Analysis Framework”. In: *Nucl. Inst. and Meth. in Phys. Res.* Vol. A. 389. 1996, pp. 81–86. URL: <http://root.cern.ch/>.
- [5] G. Brunetti. “Target Studies with FLUGG”. In: *NOvA doc-db 12556* (2014).
- [6] D. Lange C. Hagmann and D. Wright. “Cosmic-ray shower generator (CRY) for Monte Carlo transport codes”. In: *Nuclear Science Symp. Conf. Rec.* 2 (2007), pp. 1143–1146.
- [7] NOvA Collaboration. “NOvA Technical Design Report”. In: (2007). URL: http://www-nova.fnal.gov/nova_cd2_review/tdr_oct_23/tdr.htm.
- [8] Daya Bay Collaboration. “Independent measurement of the neutrino mixing angle θ_{13} via neutron capture on hydrogen at Daya Bay”. In: *Phys. Rev. D*. 90 (2014), p. 071101. URL: <http://journals.aps.org/prd/abstract/10.1103/PhysRevD.90.071101>.
- [9] G. Cowan. *Statistical Data Analysis*. Oxford Science Publications, 1998.
- [10] S. Dodelson and J. Lykken. “Complementarity of Neutrinoless Double Beta Decay and Cosmology Complementarity of Neutrinoless Double Beta Decay and Cosmology”. In: *FERMILAB-PUB-14-065-A-T* (2014). URL: <http://arxiv.org/abs/1403.5173>.
- [11] The DUNE and LBNF collaboration. “Long-Baseline Neutrino Facility (LBNF) and Deep Underground Neutrino Experiment (DUNE) - Conceptual Design Report”. In: *LBNE doc-db 10690* (2015). URL: <https://lbne.bnl.gov/tmp/volume-project.pdf>.

Bibliography

- [12] K.A. Olive et al. (Particle Data Group). “Review of particle physics”. In: *Chin. Phys. C*, 38, 090001 (2014). URL: <http://pdg.lbl.gov/2011/reviews/rpp2011-rev-passage-particles-matter.pdf>.
- [13] A. Ferrari et al. “FLUKA: a multi-particle transport code”. In: *CERN-2005-10, INFN/TC_05/11, SLAC-R-773* (2005).
- [14] A. Radovic et al. “A Technote Describing the Derivation and Size of NuMI Flux Uncertainties Used in the First NOvA Analyses”. In: *NOvA doc-db 13584* (2015).
- [15] C. Andreopoulos et al. “The GENIE Neutrino Monte Carlo Generator”. In: *Nucl. Instrum. Meth. A*.614 (2010), pp. 87–104. URL: <http://arxiv.org/abs/0905.2517>.
- [16] C. Angelini et al. “New experimental limits on $\nu_\mu \rightarrow \nu_e$ oscillations”. In: *Phys. Lett. B*.179 (1986), p. 307.
- [17] E. Eskut et al. “New results from a search for $\nu_\mu \rightarrow \nu_\tau$ and $\nu_e \rightarrow \nu_\tau$ oscillation”. In: *Phys. Lett. B*.497 (2001), pp. 8–22.
- [18] E. K. Akhmedov et al. “Series expansion for three-flavour neutrino oscillation probabilities in matter”. In: *JHEP* (2004). URL: <http://arxiv.org/abs/hep-ph/0402175>.
- [19] F. Bergsma et al. “A search for neutrino oscillations”. In: *Z. Phys. C*.40 (1988), p. 171.
- [20] F. Dydak et al. “A search for ν_μ oscillations in the Δm^2 range 0.3 – 90 eV²”. In: *Phys. Lett. B*.134 (1984), p. 281.
- [21] K. Abe et al. “Indication of Electron Neutrino Appearance from an Accelerator-produced Off-axis Muon Neutrino Beam”. In: *Phys. Rev. Lett.* 101 041801 (2011). URL: <http://arxiv.org/abs/1106.2822>.
- [22] K.Abe et al. “Measurements of neutrino oscillation in appearance and disappearance channels by the T2K experiment with 6.6×10^{20} protons on target”. In: *Phys. Rev. D*.91 072010 (2015).
- [23] L. Aliaga et al. “Design, Calibration, and Performance of the MINERvA Detector”. In: *Nucl. Inst. and Meth. A*.743 (2014), p. 130. URL: <http://arxiv.org/abs/1305.5199>.
- [24] M. Ambrosio et al. “Atmospheric neutrino oscillations from upward throughgoing muon multiple scattering in MACRO”. In: *Phys. Lett. B*.566 (2003), p. 35. URL: <http://arxiv.org/abs/hep-ex/0304037>.

Bibliography

- [25] M. Apollonio et al. "Search for neutrino oscillations on a long base-line at the CHOOZ nuclear power station". In: *Eur. Phys. J.C27* (2003), pp. 331–374. URL: <http://arxiv.org/abs/hep-ex/0301017>.
- [26] M. Guler et al. "An appearance experiment to search for ν_μ ν_τ oscillations in the CNGS beam: experimental proposal". In: *CERN-SPSC-2000-028* (2000).
- [27] N. Agafonova et al. "Discovery of tau neutrino appearance in the CNGS neutrino beam with the OPERA experiment". In: *Phys. Rev. Lett.* 115, 121802 (2015). URL: <http://arxiv.org/abs/1507.01417>.
- [28] P. Adamson et al. "First Direct Observation of Muon Antineutrino Disappearance". In: *Phys. Rev. Lett.* 107 021801 (2011). URL: <http://arxiv.org/abs/1104.0344>.
- [29] P. Adamson et al. "The NuMI Neutrino Beam". In: (2015). URL: <http://arxiv.org/abs/1507.06690>.
- [30] P. Aprili et al. "ICARUS : a second generation proton decay experiment and neutrino observatory at the Gran Sasso Laboratory". In: *CERN-SPSC-2002-027* (2002).
- [31] P. Astier et al. "Search for $\nu_\mu \rightarrow \nu_e$ Oscillations in the NOMAD Experiment". In: *Phys. Lett. B.150* (2003), pp. 19–31.
- [32] R. L. Talaga et al. "PVC Extrusion Development and Production for the NOvA Neutrino Experiment". In: *FNAL-Pub-15-049-ND-PPD* (2015).
- [33] R. N. Cahn et al. "White Paper: Measuring the Neutrino Mass Hierarchy". In: *arXive* (2013). URL: <http://arxiv.org/abs/1307.5487>.
- [34] S. Agostinelli et al. "Geant4-a simulation toolkit". In: *Nuclear Instruments and Methods in Physics Research* 506.3 (2003), pp. 250–303.
- [35] S. Ahmed et al. "Measurement of the Total Active 8B Solar Neutrino Flux at the Sudbury Neutrino Observatory with Enhanced Neutral Current Sensitivity". In: *Phys. Rev. Lett.* 92 181301 (2004).
- [36] S. Mufson et al. "Liquid Scintillator production for the NOvA experiment". In: *Nuclear Instruments and Methods in Physics Research A.799* (2015), pp. 1–9. URL: <http://arxiv.org/abs/1504.04035>.
- [37] T.T. Bohlen et al. "The FLUKA Code: Developments and Challenges for High Energy and Medical Applications". In: *Nuclear Data Sheets* 120 (2014), pp. 211–214.

Bibliography

- [38] Y. Ashie et al. "Evidence for an oscillatory signature in atmospheric neutrino oscillation". In: *Phys. Rev. Lett.* 93 101801 (2004). URL: <http://arxiv.org/abs/hep-ex/0404034>.
- [39] Y. Fukuda et al. "Atmospheric ν_ν/ν_e ratio in the multi-GeV energy range". In: *Phys. Lett. B*.335 (1994), pp. 237–245.
- [40] Y. Fukuda et al. "Solar Neutrino Data Covering Solar Cycle 22". In: *Phys. Rev. Lett.* 77 (1996), pp. 1683–1686.
- [41] C. Giunti and C. W. Kim. *Fundamentals of Neutrino Physics and Astrophysics*. Oxford University Press, 2007.
- [42] Lisa Goodenough. "Horn Current Cuts for Determining "good beam"". In: *NOvA doc-db 10646* (2014).
- [43] F. Halzen. "Ice Fishing For Neutrinos". In: Fermilab Lecture Series. 2015. URL: <http://vms.fnal.gov/asset/detail?recid=1935689#>.
- [44] R. Hatcher. "Proposal for a Unified "Flux" N-tuple Format". In: *MINOS doc-db 9070* (2012). URL: <http://minos-docdb.fnal.gov/cgi-bin/ShowDocument?docid=9070>.
- [45] A. Himmel. "The NuMI Beam Simulation with Flugg". In: *NuMI/MINOS DocDB MINOS Document.6316-v10* (2010). URL: <http://minos-docdb.fnal.gov/cgi-bin/ShowDocument?docid=6316>.
- [46] Jim Hylen. "NuMI Operating Conditions". In: *NuMIX doc-db 68* (2014).
- [47] G. Kafka. "The FluxReader Framework". In: (Aug. 2014). URL: <https://cdcvms.fnal.gov/redmine/projects/fluxreader/wiki/>.
- [48] S. E. Kopp. "Accelerator Neutrino Beams". In: *Phys. Rept.* 439 (2007), pp. 101–159. URL: <http://arxiv.org/abs/physics/0609129v1>.
- [49] S. Lein and K. R. Bays. "Numu Charged Current Energy Estimators". In: *NOvA doc-db 11208* (2015).
- [50] H. J. Lipkin. "Quantum theory of neutrino oscillations for pedestrians: simple answers to confusing questions". In: *Physics Letters B* (2006). URL: <http://arxiv.org/abs/hep-ph/0505141>.
- [51] A. Marchionni. "Neutrino Beams". In: *Fermilab Summer Lecture Series*. 2015. URL: http://neutrino.fnal.gov/events/summer_lecture_series/index.html.
- [52] M. Martens, J. Hylen, and K. Anderson. "Target and Horn Configuration for the NOvA Experiment". In: *NOVA-doc.3453* (2009).

Bibliography

- [53] M. Messier. “Neutrino Detectors”. In: *NOvA doc-db 9452* (2013).
- [54] R. H. Milburn. “Neutrino Beam Simulation using PAW with Weighted Monte Carlo”. In: *NuMI/MINOS DocDB MINOS Document.109-v1* (2008). URL: <http://minos-docdb.fnal.gov/cgi-bin/ShowDocument?docid=109>.
- [55] E. Niner. “Observation of Electron Neutrino Appearance in the NuMI Beam with the NOvA Experiment”. PhD thesis. Indiana University, 2015. URL: <http://inspirehep.net/record/1389804>.
- [56] A. J. Norman. “The NOvA experiment”. In: *Neutrino 2014 (Boston)*. 2014. URL: <https://indico.fnal.gov/conferenceOtherViews.py?view=standard&confId=8022>.
- [57] J. M. Paley et al. “Executive Summary of the 2015 (First Analysis) numu Disappearance Analysis”. In: *NOvA doc-db 13641* (2015).
- [58] R. B. Palmer. “Magnetic Fingers”. In: *CERN Informal Workshop on Neutrino Physics, CERN-65-32* (1965), pp. 141–146. URL: <http://cds.cern.ch/record/862814/files/p141.pdf>.
- [59] S. Parke. “Neutrinos: Theory and Phenomenology”. In: *Nobel Symposium on LHC Results* (2013). URL: <http://arxiv.org/abs/1310.5992>.
- [60] R. B. Patterson. “First Oscillation Results from NOvA”. In: *Fermilab Joint Experimental-Theoretical Seminar*. August 6, 2015. URL: <http://nova-docdb.fnal.gov/cgi-bin/ShowDocument?docid=13883>.
- [61] R. B. Patterson. “The NOvA experiment: status and outlook”. In: *Nuclear Physics B* (2012). URL: <http://arxiv.org/abs/1209.0716v1>.
- [62] Z. Pavlovic. “Observation of Disappearance of Muon Neutrinos in the NuMI Beam”. PhD thesis. The University of Texas at Austin, 2008. URL: <http://www.lib.utexas.edu/etd/d/2008/pavlovicz79754/pavlovicz79754.pdf>.
- [63] S. R. Phan-Budd and L. Goodenough. “Technical Note on the NOvA Beam Monitoring for 2015 Summer Analysis”. In: *NOvA doc-db 13572* (2015).
- [64] B. Pontecorvo. In: *Sov. Phys. JETP* 6.429 (1957).
- [65] N. J. Raddatz. “Reconstructed Muon Identification”. In: *NOvA doc-db 11206* (2014).
- [66] B. Richter. “Conventional Beams or Neutrino Factories: The Next Generation of Accelerator-Based Neutrino Experiments”. In: *SLAC-PUV-8587* (2000). URL: <http://arxiv.org/abs/hep-ph/0008222v1>.

Bibliography

- [67] P. R. Sala and S. Vanini. *FLUGG: FLUKA + Geant4 Geometry for Simulation in HEP*. Tech. rep. 2003. URL: <http://www.fluka.org/content/tools/flugg/>.
- [68] R. Schroeter. "Wrong sign neutrino contamination and beam nue content for FHC/RHC beam configurations - Fluka 2011". In: *NOvA doc-db 13097* (2015).
- [69] P. Shanahan. "Current and Future Long Baseline Neutrino Experiments". In: *Neutrino Summer Student Lecture Series* (2015). URL: http://neutrino.fnal.gov/events/summer_lecture_series/LongBaselineShanahan.pdf.
- [70] L. Suter. "ND Selection for the Muon Neutrino Disappearance Analysis". In: *NOvA doc-db 13212* (2015).
- [71] J. A. Thomas and P. L. Vahle. *Neutrino Oscillations (Present Status and Future Plans)*. World Scientific, 2008.
- [72] M. Del Tutto. "Ancestor History in FLUGG - Technical Note". In: *NOvA doc-db 14035* (2015).
- [73] M. Del Tutto. "Blessing Package - Beam Simulation Plots". In: *NOvA doc-db 13524* (2015).
- [74] M. Del Tutto. "Horn Current Study". In: *NOvA doc-db 13360* (2015).
- [75] M. Del Tutto et al. "Special Run proposal". In: *NOvA doc-db 13451* (2015). URL: <http://nova-docdb.fnal.gov/cgi-bin/ShowDocument?docid=13451>.
- [76] S. van der Meer. "A directive device for charged particles and its use in an enhanced neutrino beam". In: *CERN-61-07* (1961).
- [77] K. Winter. *Neutrino Physics*. Cambridge University Press, 2000.
- [78] L. Wolfenstein. "Neutrino Oscillations in Matter". In: *Phys.Rev. D.17* (1978), pp. 2369–2374.
- [79] R. Zwaska. "Accelerator systems and instrumentation for the NuMI neutrino beam". PhD thesis. University of Texas at Austin, 2005. URL: <http://inspirehep.net/record/704397/>.